Quantitative Description of the Morphology and Microdamages of Composite Materials

Axelsen, M. S.

Publication date:
1995

Document Version
Publisher's PDF, also known as Version of record

Institute of Mechanical Engineering
Aalborg University
Special Report No. 26

Quantitative Description of the Morphology and Microdamages of Composite Materials

Ph.D. Dissertation

by

Mikael Staal Axelsen

Printed at Aalborg University, January 1995.

ISBN 87-89206-03-7

Preface

This dissertation has been submitted to the Faculty of Science and Technology of Aalborg University, Aalborg, Denmark, in partial fulfilment of the requirements for the technical Ph.D. degree.

The project underlying this thesis has been carried out from July 1992 to December 1994 at the Institute of Mechanical Engineering at Aalborg University. The project has been supervised by Professor, lic.techn. Ryszard Pyrz, to whom I am deeply grateful for his inspiring ideas, his encouraging spirit and his guidance through the project.

I would like to thank my colleagues, M.Sc. Eric Knudsen and M.Sc. Peter From for many exhausting and inspiring discussions and also the other colleagues at the Institute of Mechanical Engineering. I am greatly indebted to Susanne Nielsen for her professional editorial assistance.

The present work has been supported partly by the Centre for Polymer Based Composite Materials under the Material Technological Research Programme (MUP I) and partly by the Danish Technical Research Council. The support is gratefully acknowledged.

Mikael Staal Axelsen

Aalborg, January 1995

Abstract

The purpose of the present Ph.D. project is to investigate correlation between the microstructure variability and transverse mechanical properties. The material considered here is a polymer based unidirectional composite with long cylindrical fibers, and the transverse properties can be analysed by considering a plane cross section. Then the microstructure appears as circular inclusions embedded in a matrix.

In order to perform this correlation a stress analysis method is established and it is possible to determine the stress field in a composite containing multiple randomly dispersed fibers. The method takes into account the stress interaction between fibers using a superposition scheme.

To determine the stress intensity factors for cracks situated among the fibers an interaction procedure is proposed. The procedure takes all interaction effects into account, and transmission factors, which relate the pressure distribution on the crack face with the interacting stresses, are derived.

A crack growth procedure, which includes both matrix and interface cracking, is established. For matrix cracking a well known fracture criterion is applied and for interface cracking a criterion based on the strain–energy density is proposed. Critical values must be given for the strength of both the matrix and the interface.

The microstructure variability is described by applying different statistical parameters. The degree of clustering is indicated by the nearest neighbour distance and the distinction between various distributions is performed by introducing functions belonging to the spatial statistics. Four distinct types of fiber distributions are generated within a unit cell, which is exposed to various boundary conditions.

Stress field calculations for the four distinct types of distributions can be correlated with the dispersion of fibers. The stress field inside the fibers is dependent on the ratio between the mean nearest neighbour distance and the mean nearest neighbour orientation. Peaks of the local stress components around the fibers, which are partly responsible for the nucleation of cracks, are also affected by the distribution of fibers.

Variation of the fracture toughness of the material is estimated by applying a correlation function, which relates the stress intensity factor of a macrocrack with the exact position of the neighbouring fibers. Different distributions can be discriminated both with respect to the type of distribution and within the distribution type itself by applying the function.

By applying a crack nucleation procedure the stress intensity factor of a macrocrack located in the vicinity of the fiber distribution is estimated as microcracks initiate at the interface between the matrix and the fibers. In this procedure the load is gradually increased until microcracks appear at all interfaces, and during this load increase the stress intensity factor is calculated. Particular configurations of fiber may change the fracture toughness, but the nucleation of cracks reverses the effect.

The strength of interfaces is estimated by analysing the crack paths in real microstructures and comparing the roughness of the fracture profile with the corresponding numerical models, for which the strength of the interface is changed.

Abstrakt

Formlet med dette Ph.D. projekt er at undersge korrelationen mellem mikrostrukturers forskelligartighed og de transverse mekaniske egenskaber. Det undersgte materiale er en polymerbaseret ensrettet komposit med lange cylindriske fibre. De transverse egenskaber analyseres ved at betragte et plant tvrsnit, og mikrostrukturen fremstr derved som cirkulre inklusioner omgivet af matrixmateriale.

For at undersge denne korrelation er en metode for spndingsanalyse etableret. Det muliggr bestemmelse af spndingsfeltet i en komposit, som indeholder multiple tilfldigt fordelte fibre. Metoden medtager spndingsinteraktionen mellem fibre ved anvendelse af superposition.

For at bestemme spndingsintensitetfaktorer for revner placeret mellem fibrene er en interaktionsprocedure foreslet. Proceduren medtager alle interaktionseffekter, og der er udledt en transmissionsfaktor, der relaterer spndingsfordelingen p revnefladerne med interaktionsspndingerne.

Der er etableret en revnevkstprocedure, der inkluderer bde matrix- og interfacerevner. For matrixrevner er et kendt brudkriterie anvendt. For interfacerevner er der foreslet et kriterie, som er baseret p tjningsenergidensitet. Kritiske vrdier skal angives for styrken af bde matrix og interface.

Mikrostrukturens forskelligartighed beskrives ved at anvende forskellige statistiske parametre. Graden "clustering" er angivet ved *nearest neighbouring distance*, og adskillelsen mellem forskellige fordelinger er udfrt ved introduktion af funktioner tilhrende rumlig statistik. Fire forskellige typer af fiberfordelinger er genereret i en enhedscelle, der er udsat for forskellige randbetingelser.

Spndingsfeltberegninger for de fire forskellige typer af fordelinger kan korreleres med fordelingen af fibre. Spndingsfeltet i fibrene afhnger af forholdet mellem *mean nearest neighbour distance* og *mean nearest neighbour orientation*. Maxima af lokale spndingskomponenter omkring fibrene, som er delvist skyld i dannelsen af revner, er ogs pvirket af fordelingen af fibre.

Variationen af brudsejheden af et materiale er estimeret ved at anvende en korrelationsfunktion, der relaterer spndingsintensitetfaktorene af en makrorevne med den eksakte position af nrliggende fibre. Ved at anvende funktionen kan forskellige fordelinger adskilles bde med hensyn til typen af fordeling og indefor fordelingstypen selv.

Ved at anvende en revnedannelseprocedure er spndingsintensitetfaktoren af en makrorevne, placeret i nrheden af en fiberfordeling, estimeret, mens mikrorevner initieres ved interfacet mellem matrix og fibrene. I denne procedure er belastningen gradvist get, indtil mikrorevner forekommer i alle interfaces, og undervejs er spndingsintensitetfaktoren beregnet. Specielle konfigurationer af fibre kan ndre brudsejheden, men dannelsen af mikrorevner reverserer effekten.

Styrken af interfaces er estimeret ved at analysere revnestien i virkelige mikrostrukturer og sammenligne ruheden af brudprofilet med tilsvarende numeriske modeller, hvor styrken af interfacet er ndret.

Contents

Introduction

In the recent years the investigation of composite materials has received more attention in the field of micromechanics because it is recognized that the microstructure influences the properties of the material. Furthermore, understanding the mechanism on a microstructural level leads inevitably to an understanding of the mechanism on a macrostructural level. The interest for micromechanics is also enhanced by the development of experimental equipment as well as possibility for fast numerical analysis.

For unidirectional composites with long fibers, which are the subject for the present work, the transverse properties are very much affected by constitution of the microstructure. In this case the constituents of the microstructure are fibers dispersed in the matrix material but also the existence of cracks influences the response of the material. In order to perform quantitative analysis, it is necessary to establish methods, which can provide information about characteristic parameters of the materials, and the methods must take into account the constitution of the microstructure.

The microstructural influence on the mechanical properties arises due to the interaction between the constituents in the composite material, and the amount of interaction is determined by their relative position. In order to simplify the analysis it is usually assumed that the microstructure has some form of regularity (fig. 0.1) or that fibers and cracks are sparsely distributed.

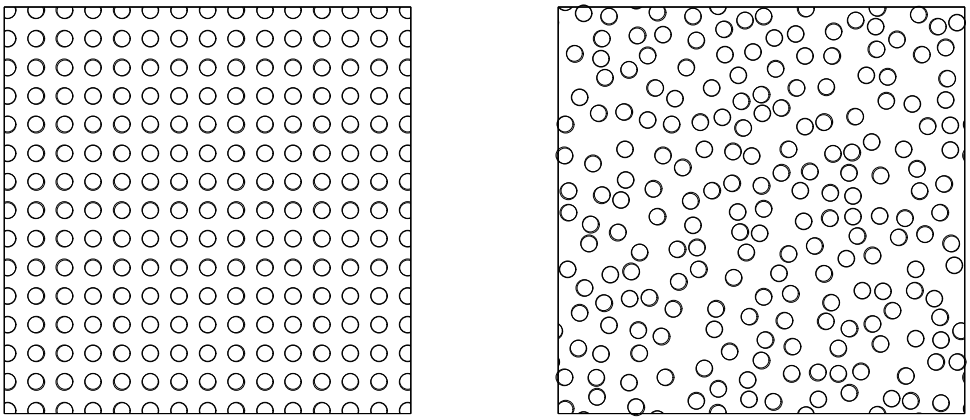

(a) (b)

Figure 0.1: Regular and non–regular distribution of fibers.

This makes it reasonable to create a repetitious *unit cell* containing a part of a fiber, one fiber, or a few fibers, which is made representative for the whole microstructure.

An elaborated analysis may then be performed on the material using simplified models. The simplified models are sufficient as long as the interaction effects do not vary in the microstructure for the regular distributions or as long as the interaction effects between inclusions and cracks are insignificant for the dilute distributions.

In general the microstructure is not regular but more random. The random dispersion of inclusions and cracks leads to a strong local interaction in areas of the microstructure where the distances between the inclusions are small. As for the regular distributions it is not reasonable to include only a few fibers in the analysis and the unit cell concept must be re–defined in order to include enough fibers so that the whole microstructure may be represented. The number of fibers needed in the unit cell depends on microstructure and the desired information.

The relatively limited knowledge of how the distribution of fibers and cracks influences the transverse properties of the materials makes it interesting to investigate the correlation between the microstructure variability and the response of the materials. In order to perform this type of investigation it is imperative to apply a method, which is able to determine the stress field in a material with randomly dispersed fibers as well as determining the stress intensity factors for cracks situated among these fibers. As a first attempt it is reasonable to model the material with finite elements, as commercial finite element programs facilitate both the possibility for geometric modelling and numerical calculation. But as a large number of fibers in the re–defined unit cell may become necessary it renders the finite element modelling very difficult and leads to an increase of the computational time as the number of fibers is increased. Therefore, is it necessary to develop another approximate, numerical method, which takes into account the interaction effects.

As it is an enormous task to analyse all random constitutions of composite materials it is reasonable to classify their morphology and only consider a few representative microstructures. The randomness can be nearly complete random and also to some extent orderly, and the classification can be performed by applying various statistical descriptors, which take into account the exact position of constituents. Materials with a very high concentration of inhomogenities are less affected by the distribution than materials with low concentration. Therefore, the correlation between the mechanical properties and the geometrical arrangement of the microstructure is only performed on a few typical dilute configurations of fibers and cracks.

Related Work

Spatial distribution of point patterns is described by Rieply [24] by applying a *second order intensity function*. The function is clearly able to differentiate between various dispersions of points. In Pyrz [18], [19] and [20] the function is used in the description of fiber distributions in unidirectional composites. Points are represented by fiber centres and the function is able to distinguish between various fiber arrangements. Furthermore, the *nearest neighbour distances* and *Dirichlet cell tesselation* are used in the description of fiber distributions, and separation between distributions is performed by calulating the cumulative distribution of distances and cell areas, respectively. These latter descriptors have also been presented by Everett and Chu [5] in order to characterize composite microstructures. Applying spatial descriptors to the distribution of fibers is very useful and provides quantitative information about microstructure.

The interaction problem between a macrocrack and neighbouring microcracks is solved in Meguid *et al.* [14] using finite elements. Various configurations are considered and regions of the material are seen to amplify the stress intensity factors, and in other regions it is reduced. Also in Lam and Phua [11] and Lam and Wen [12] various configurations are analysed, but the problems are now reduced to a system of singular integral equations. Hori and Nemat-Nasser [6] solved different problems using *the method of pseudotractions*. Kachanov [9] introduced a superpostion technique where cracks are analysed in an arbitrary arrangement. Applying this technique the interaction problem between a macrocrack and an array of microcracks is solved in Kachanov *et al.* [10]. The methods, which take into account the interaction between cracks, make it possible to analyse a large variety of crack arrangements and thus estimate the fracture toughness of materials.

The interaction problem between an inclusion and a crack is presented in Erdogan *et al.* [4]. The solution is obtained through a system of singular integral equations. Using the similar method Lam and Wen [13] considered the interaction problem of an inclusion and arbitrarily located cracks. Interaction between randomly dispersed fibers and a crack is analysed in Pijaudier-Cabot and Bažant [17]. A procedure is developed and applied for various configurations of a crack situated among the fibers. The method of pseudotractions is applied for randomly dispersed fibers and cracks by Horii and Nemat-Nasser [7]. These methods allow to include the interaction between fibers and cracks and contributes also to the fracture toughness estimation.

Brockenbrugh *et al.* [2] found that the fiber distributions affect the plastic response of a metal–matrix composite. The analysis is performed using finite elements where the unit cell for random microstructures is assumed to contain a large number of fibers. Pyrz [21] showed that a correlation exists between the dispersion of fibers and the fractal properties of fracture profiles of composite materials. Axelsen og Pyrz [1] applied a method based on Pijaudier-Cabot and Bažant's fiber–crack interaction procedure and Kachanov's crack–crack superpostion technique. An estimate of the fracture toughness for various dispersion of fibers is given for a composite material where interface cracks nucleate. The load carrying capacity is correlated with the disorder of a two–phase material in Pyrz and Bochenek [22] and [23]. A discrete model based on Dirichlet cell tesselation is developed and it allows for crack nucleation. The correlation between the microstructure variability and the mechanical properties is useful as it contributes to the quantification of composite materials on a microstructural level.

Outline

In chapter 1 the fundamental ideas of the stress analysis method are presented. The method is able to determine the stress field in an infinitely extented solid exposed to uniform tractions at the remote boundaries and with randomly dispersed inclusions. It is based on a superpostion scheme where the interaction effect between the inclusions is taken into account and an iterative procedure is established in order to solve the problem.

Chapter 2 contains the derivation of the interaction scheme for multiple inclusions and cracks. Stress intensity factors of cracks situated among randomly dispersed inclusions can be determined with the method. The interaction effect enters the solution through transmission factors, which account for the interacting stress field from a crack to an inclusion or another crack. The solution can be found directly, although the iterative

procedure stated in chapter 1 also enters the method.

Chapter 3 presents a procedure for crack growth in a composite material containing multiple inclusions and cracks. Both crack growth in the pure matrix and at the interface between the fibers and the matrix are considered. An iterative procedure is established to account for the combined crack evolution.

Chapter 4 presents various methods to quantify the morphology of a microstructure. The re–defined unit cell is established on basis of *zone of influence* calculations. Statistical descriptors are applied to typical classes of fiber distributions and their ability to describe the constitution of a microstructure is investigated.

Chapter 5 correlates the distribution of fibers with the local stress field. Typical classes of fibers distributions are presented and they serve as representative configurations. The stress field inside the fibers is correlated with the microstructure variability. The local stress field around the fibers is determined in order to analyse sensitivity of various configurations of fibers towards crack initiation at the interphase. Microstructures from real materials, which are manufactured under various conditions, are also investigated.

Chapter 6 provides information as to how the distribution of fibers affects the crack parameters. The problem considered consists of a crack situated in the vicinity of dispersed fibers, and an estimate of short–range and long–range interaction is given. On basis of the stress field for the single inclusion problem a *direct correlation function* is established. The function relates the stress intensity factor of a crack with the neighbouring dispersion of fibers.

Chapter 7 deals with the problem of how the fracture toughness of material is affected if interface cracks nucleate. As in chapter 6 the configuration consists of a crack, located in the vicinity of dispersed fibers. A procedure for crack initiation, which allows to analyse the deterioration of the material, is developed. The fracture toughness is determined for various configurations and is seen to change depending on the nucleation of cracks.

Chapter 8 is devoted to the description of crack trajectories of percolating cracks. Typical fiber distributions are considered, and cracks are initiated at the edge of the observation window. The cracks are then allowed to extend through the microstructure and depending on the distribution of fibers the crack path changes. By investigating the crack path in real microstructures the strength of the interface is estimated.

Chapter

1

Stress Analysis Method

The determination of the local stress field in a composite material is of interest when considering the microstructure's influence on the transverse mechanical properties. Stress analysis methods, which can be applied, are limited by the composition and complexity of the composite, e.g. spatial distribution and shape of the inclusions. For composites with long cylindrical fibers embedded in a matrix material and aligned unidirectionally the analysis may be performed on a plane section perpendicular to the fiber direction. Thus the analysis may be reduced to a two–dimensional problem consisting of a matrix with circular inclusions.

The spatial distribution of inclusions is normally assumed to have some form of regularity or the inclusions are assumed to be sparsely distributed. Due to the regularity of the distribution the inclusions will be exposed to the same amount of interaction, and a unit cell only needs to contain a small part of the distribution. The simplified unit cell is then assumed to be representative throughout the microstructure. For the sparse distribution it is assumed that the inclusions are not exposed to any interaction and also in this case a simple unit cell may be created. These types of unit cells make it possible to apply both analytical and numerical stress analysis methods as the problem is relatively simple. When the distribution of inclusions is assumed to be random, the inclusions are not exposed to the same amount of interaction, and creating a unit cell with only a small part of the distribution is not adequate. Therefore, the unit cell must be re–defined so that it contains enough fibers to be representative for the microstructure and it must account for the varying interaction between the inclusions.

Due to the complexity of the problem it cannot be solved analytically. Only numerical methods are applicable. The methods must be able to determine the stress field in a plane solid containing multiple inclusions, which are randomly dispersed. As a first attempt the problem can be solved using finite element modelling but as it is necessary to include a large number of inclusions the finite element method is inexpedient to apply and the computational time increases immensely when the number of inclusions is increased. Therefore, another numerical method is applied. This method is based on determining the eigenstresses within the inclusions based on a superposition scheme using an iterative procedure.

The main problem of determining the stress field in an elastic solid containing randomly dispersed inclusions is to include the interaction effects between inclusions. The

problem with one inclusion in an infinite solid may be solved analytically using the complex potential theory by Muskhelishvili [16] or the Eshelby solution (Mura [15]). Yu and Sendeckyj [27] applied the complex potential theory and calculated numerically the stress field in an infinite plane elastic solid containing multiple circular inclusions. The distribution of inclusions may be random although overlap of inclusions is not permitted. Horii and Nemat-Nasser [7] presented an approximate method to calculate the stress and strain field in a linearly elastic, homogeneous solid, which contains multiple randomly distributed defects of arbitrary shape. The technique is called *the method of pseudotractions* and takes the interaction effects between the defects into account. The method rests upon superposition of subproblems. Pijaudier-Cabot and Bažant [17] also considered the interaction between multiple, randomly distributed inclusions and solved the problem by extending the solution for a single inclusion into multiple inclusions. The latter method is applied in the following.

In section 1.1 of this chapter an iterative procedure for calculating the stress field in a solid with only one inclusion is presented as this constitutes the basic idea for the stress analysis method. Results from the procedure are compared with the analytical solution. In section 1.2 the method is extended to include multiple inclusions using superposition of subproblems. Stress field calculations are compared with corresponding finite element results.

1.1 Stress Field for One Inclusion

In order to establish a stress analysis method for multiple inclusions the solution for a single inclusion is needed and consists in the following of a calculation of the stress field in a solid containing a circular inclusion. As mentioned both analytical and numerical solutions may be applied to this problem and the methods are not easily transformed into a method for multiple, randomly distributed inclusions. For this purpose a numerical method has been presented by Pijaudier-Cabot and Bažant [17]. As for the Eshelby solution the eigenstrain analogy is also applied but contrary to this solution where the Eshelby tensor is solved, an iterative procedure derived. In this procedure the first step is to find the stress field inside the inclusion. Then this information is used to find the stress field at any point outside the inclusion. In the following the method is derived in details and compared with analytical results.

The problem consists of determining the stress field in an infinitely extented plane solid containing a circular inclusion and subjected to unidirectional uniform tractions $\boldsymbol{\sigma}_\infty$[1] at the remote boundaries (fig. 1.1).

The matrix and inclusion materials are perfectly linear elastic with stiffness $\mathbf{D}_m$ and $\mathbf{D}_a$ respectively. The interface between the inclusion and the matrix is assumed perfect and no other defects are assumed to exist. The boundary curve of the inclusion is denoted by Γ_a and radius of the inclusion is R.

When applying tractions to the solid with elastic stiffness differing from the inclusion it will lead to a disturbance of the applied stress field $\boldsymbol{\sigma}_\infty$ due to the presence of the

[1] The following notation is used. $\boldsymbol{\sigma}$ and $\boldsymbol{\varepsilon}$ in boldface denote a vector containing the non–bold components σ and ε respectively. For convenience the notation $\bar{\boldsymbol{\sigma}}$ is also used where the overbar denotes a matrix. Upper case roman letters in boldface denote a matrix and lower case letters in boldface denote a vector. Non–bold letters are just scalars.

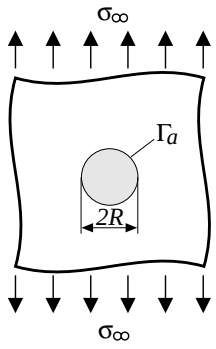

Figure 1.1: Infinitely extented plane solid containing a circular inclusion and exposed to uniform tractions at the remote boundaries.

inclusion. The disturbed stress field is denoted $\boldsymbol{\sigma}_a$ and the corresponding strains from the applied and disturbed stress are denoted by $\boldsymbol{\varepsilon}_\infty$ and $\boldsymbol{\varepsilon}_a$, respectively. Hooke's law for the inclusion and matrix may be written as:

$$\boldsymbol{\sigma}_\infty + \boldsymbol{\sigma}_a = \mathbf{D}_a(\boldsymbol{\varepsilon}_\infty + \boldsymbol{\varepsilon}_a) \quad \text{inside } \Gamma_a \tag{1.1}$$

$$\boldsymbol{\sigma}_\infty + \boldsymbol{\sigma}_a = \mathbf{D}_m(\boldsymbol{\varepsilon}_\infty + \boldsymbol{\varepsilon}_a) \quad \text{outside } \Gamma_a \tag{1.2}$$

By applying the theory of eigenstrains and eigenstresses to the problem, referred to as the *equivalent inclusion method*, it is assumed that the solid is homogeneous with elastic stiffness $\mathbf{D}_m$ everywhere but the area occupied by the inclusion contains eigenstrains $\boldsymbol{\Delta\varepsilon}$. The problem may now be rewritten as:

$$\boldsymbol{\sigma}_\infty + \boldsymbol{\sigma}_a = \mathbf{D}_m(\boldsymbol{\varepsilon}_\infty + \boldsymbol{\varepsilon}_a - \boldsymbol{\Delta\varepsilon}) \quad \text{inside } \Gamma_a \tag{1.3}$$

$$\boldsymbol{\sigma}_\infty + \boldsymbol{\sigma}_a = \mathbf{D}_m(\boldsymbol{\varepsilon}_\infty + \boldsymbol{\varepsilon}_a) \quad \text{outside } \Gamma_a \tag{1.4}$$

The necessary condition for equivalency between equations 1.1 and 1.3 reads:

$$\mathbf{D}_a(\boldsymbol{\varepsilon}_\infty + \boldsymbol{\varepsilon}_a) = \mathbf{D}_m(\boldsymbol{\varepsilon}_\infty + \boldsymbol{\varepsilon}_a - \boldsymbol{\Delta\varepsilon}) \quad \text{inside } \Gamma_a \tag{1.5}$$

Rearranging this equation and substituting the actual strains $\boldsymbol{\varepsilon}_\infty + \boldsymbol{\varepsilon}_a$ with $\boldsymbol{\varepsilon}$ lead to:

$$\mathbf{D}_m\boldsymbol{\Delta\varepsilon} = (\mathbf{D}_m - \mathbf{D}_a)\boldsymbol{\varepsilon} \quad \text{inside } \Gamma_a \tag{1.6}$$

This equation is written in terms of strains but it is necessary to write it in terms of stresses so $\boldsymbol{\varepsilon}$ is substituted with $\mathbf{D}_a^{-1}\boldsymbol{\sigma}$ and $\mathbf{D}_m\boldsymbol{\Delta\varepsilon}$ with $\boldsymbol{\Delta\sigma}$:

$$\boldsymbol{\Delta\sigma} = (\mathbf{D}_m - \mathbf{D}_a)\mathbf{D}_a^{-1}\boldsymbol{\sigma} \quad \text{inside } \Gamma_a \tag{1.7}$$

where $\boldsymbol{\sigma}$ is the actual stress field inside the inclusion and $\boldsymbol{\Delta\sigma}$ is the eigenstress or the unbalanced stress field which is contained within the actual stress field. Equation 1.7 is the basic equation in the method and instead of solving it directly through the Eshelby tensor it is solved iteratively. Examining the equation it is noticeable that $\boldsymbol{\Delta\sigma}$ is assigned

the opposite sign if the inclusion material is stiffer than the matrix material and vice versa.

The components of stiffness matrix $\mathbf{D}$ for an isotropic material in plane stress are calculated as:

$$\mathbf{D} = \begin{bmatrix} \frac{E}{1-\nu^2} & \frac{\nu E}{1-\nu^2} & 0 \\ \frac{\nu E}{1-\nu^2} & \frac{E}{1-\nu^2} & 0 \\ 0 & 0 & \frac{2E}{2(1+\nu)} \end{bmatrix} \tag{1.8}$$

and for plane strain:

$$\mathbf{D} = \begin{bmatrix} \frac{E(1-\nu)}{(1+\nu)(1-2\nu)} & \frac{\nu E}{(1+\nu)(1-2\nu)} & 0 \\ \frac{\nu E}{(1+\nu)(1-2\nu)} & \frac{E(1-\nu)}{(1+\nu)(1-2\nu)} & 0 \\ 0 & 0 & \frac{2E}{2(1+\nu)} \end{bmatrix} \tag{1.9}$$

where E is Young's modulus and ν is Poisson's ratio. The stress and strain vectors are written as:

$$\boldsymbol{\sigma} = \begin{Bmatrix} \sigma_x \\ \sigma_y \\ \sigma_{xy} \end{Bmatrix} \qquad \boldsymbol{\varepsilon} = \begin{Bmatrix} \varepsilon_x \\ \varepsilon_y \\ \varepsilon_{xy} \end{Bmatrix} \tag{1.10}$$

Equation 1.5 may be visualized from the following analogy where the elasticity problem of the heterogeneous solid is transformed into an equivalent elasticity problem of a homogeneous solid (fig. 1.2).

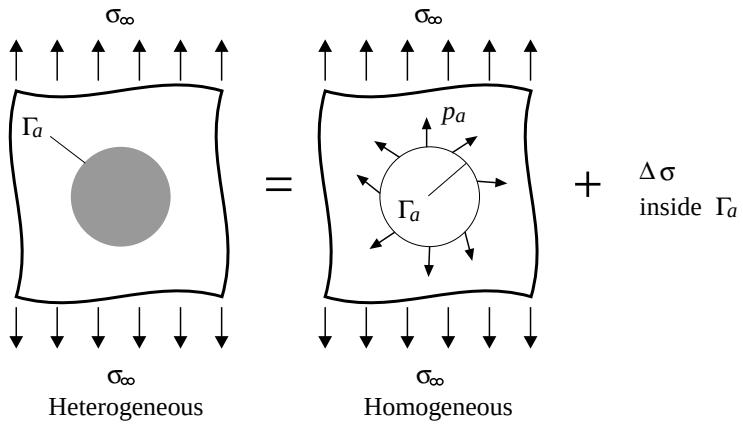

Figure 1.2: Equivalency between a heterogeneous and a homogeneous solid.

In the heterogeneous solid the material properties for the inclusion differ from the matrix and the stress field may be described by equations 1.1 and 1.2. In the equivalent homogeneous solid the material properties are the same for both the inclusion and the matrix but in addition an unbalanced stress field is introduced inside the area enclosed by the boundary contour Γ_a. Due to the unbalanced stress field tractions $\mathbf{p}_a$ exist at the boundary and the stress field may be described by equations 1.3 and 1.4. These tractions create a disturbance of the stress field in the solid and may be written as:

$$\mathbf{p}_a = -\boldsymbol{\Delta\bar{\sigma}}\mathbf{n}_a = \begin{bmatrix} \Delta\sigma_x & \Delta\sigma_{xy} \\ \Delta\sigma_{xy} & \Delta\sigma_y \end{bmatrix} \mathbf{n}_a \quad \text{on} \quad \Gamma_a \tag{1.11}$$

where $\mathbf{n}_a$ is a unit outward normal to the boundary curve Γ_a of the inclusion. The stress field may be written as:

$$\boldsymbol{\sigma} = \boldsymbol{\sigma}^* - \boldsymbol{\Delta\sigma} \quad \text{inside} \quad \Gamma_a \tag{1.12}$$

$$\boldsymbol{\sigma} = \boldsymbol{\sigma}^* \quad \text{outside} \quad \Gamma_a \tag{1.13}$$

where $\boldsymbol{\sigma}^*$ is an equilibrium stress field when the stiffness of the inclusion $\mathbf{D}_a$ is changed to $\mathbf{D}_m$, and the tractions $\mathbf{p}_a$ at the interface Γ_a and the remote boundary tractions $\boldsymbol{\sigma}_\infty$ are acting. Thus $\boldsymbol{\sigma}^*$ is the stress field including the disturbance and $\boldsymbol{\sigma}$ is the stress field, which also includes the eigenstress inside the inclusion.

As seen from figure 1.2, the unknown parameter in the equivalent problem is $\boldsymbol{\Delta\sigma}$. To determine this an iterative procedure is applied. The idea of the iterative procedure is to calculate the stress field inside the inclusion using the existing value of $\boldsymbol{\Delta\sigma}$. When the new stress field is known, the unbalanced stress field is recalculated. The procedure is repeated until the change of the stress field becomes small enough.

As a starting point in the iterative procedure the stress field $\boldsymbol{\sigma}$ in the solid is assumed to be equal to the applied tractions $\boldsymbol{\sigma}_\infty$. Uniform tractions are applied in the y-direction:

$$\left\{ \begin{array}{c} \sigma_x \\ \sigma_y \\ \sigma_{xy} \end{array} \right\} = \left\{ \begin{array}{c} 0 \\ \sigma_\infty \\ 0 \end{array} \right\} \tag{1.14}$$

The unbalanced stress field inside the inclusion is then obtained from equation 1.7. The tractions $\mathbf{p}_a$ are obtained from equation 1.11, in which the unit outward normal to the circular contour is $\mathbf{n}_a = \{\cos\alpha, \sin\alpha\}^T$. To determine the stress field produced by the tractions $\mathbf{p}_a$ in a homogeneous solid the theory of a concentrated force applied at a point in an infinite homogeneous elastic space is used (Muskhelishvili [16]). The stress field may be written as a function of two analytical functions of the complex variable $z = re^{i\theta}$:

$$\begin{aligned} \sigma_x + \sigma_y &= 2(\Phi(z) - \overline{\Phi(z)}) \\ \sigma_x - i\sigma_{xy} &= \Phi(z) + \overline{\Phi(z)} - \overline{z}\Phi'(z) - \Psi(z) \end{aligned} \tag{1.15}$$

For a concentrated force applied at a point O the functions $\Phi(z)$ and $\Psi(z)$ are (fig. 1.3):

$$\begin{aligned} \Phi(z) &= \frac{P_x + iP_y}{2\pi(1+\kappa)} \frac{1}{z} \\ \Psi(z) &= \frac{\kappa(P_x - iP_y)}{2\pi(1+\kappa)} \frac{1}{z} \end{aligned} \tag{1.16}$$

where

$$\kappa = \left\{ \begin{array}{ll} (3-\nu)/(1+\nu) & \text{for plane stress} \\ 3 - 4\nu & \text{for plane strain} \end{array} \right. \tag{1.17}$$

The functions $\Phi(z)$ and $\Psi(z)$ are inserted into equation 1.15 and by solving this with respect to the stress components the normal and shear stresses due to a concentrated force at a point (x_P, y_P) in the global cartesian coordinate system become:

$$\sigma_x^P = \frac{-P_x \cos\theta}{2\pi r(1+\kappa)}(4\sin^2\theta - 3 - \kappa) + \frac{P_y \sin\theta}{2\pi r(1+\kappa)}(4\sin^2\theta - 5 + \kappa)$$

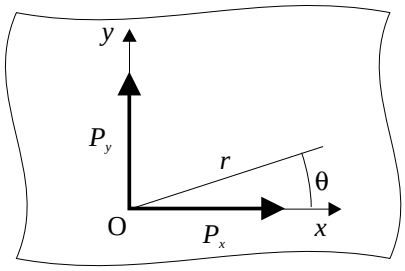

Figure 1.3: Coordinate system for the concentrated forces.

$$\sigma_y^P = \frac{-P_x \cos\theta}{2\pi r(1+\kappa)}(-4\sin^2\theta - 1 + \kappa) + \frac{P_y \sin\theta}{2\pi r(1+\kappa)}(-4\sin^2\theta + 1 - \kappa) \quad (1.18)$$

$$\sigma_{xy}^P = \frac{-P_x \sin\theta}{2\pi r(1+\kappa)}(4\sin^2\theta - 3 - \kappa) + \frac{P_y \cos\theta}{2\pi r(1+\kappa)}(-4\sin^2\theta + 1 - \kappa)$$

$\mathbf{r}$ (fig. 1.4) is the vector connecting the point (x_P, y_P), at which P_x and P_y are applied, and the point (x, y), at which the stresses are calculated. The angle θ is angular deviation between the direction of P_x and $\mathbf{r}$.

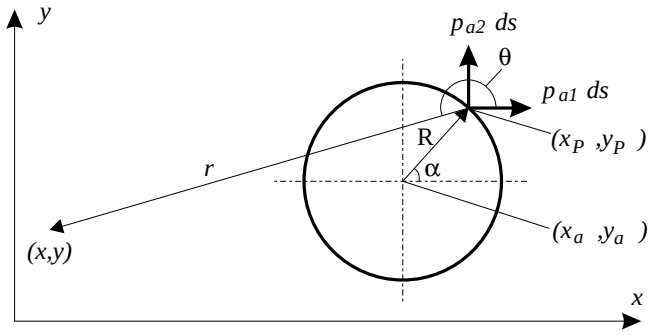

Figure 1.4: Geometry used to calculate the stress field at a point (x, y) due to interface tractions $\mathbf{p}_a$.

To apply this theory to the inclusion problem the boundary curve Γ_a is subdivided into segments of length ds, and the tractions $\mathbf{p}_a$ are replaced by concentrated forces $\mathbf{p}_a ds$ per unit thickness. This means that at any angle α, a set of two concentrated forces $p_{a1}ds$ and $p_{a2}ds$ acts along x and y direction, respectively. The vector $\mathbf{r}$ and its length r are expressed as:

$$\mathbf{r} = \{(x - x_a - R\cos\alpha), (y - y_a - R\sin\alpha)\}$$

$$r = \sqrt{(x - x_a - R\cos\alpha)^2 + (y - y_a - R\sin\alpha)^2} \quad (1.19)$$

where (x_a, y_a) represents the centre of the inclusion. Instead of expressing θ explicitly, which leads to non–periodic function, it will be expressed implicitly in the form:

$$\cos\theta = \frac{\mathbf{r}\cdot\mathbf{v}}{rv} \qquad \sin\theta = \frac{\hat{\mathbf{r}}\cdot\mathbf{v}}{rv} \quad (1.20)$$

where $\mathbf{v} = \{1, 0\}^T$ is a unit vector in the x direction. P_x and P_y in equation 1.18 are replaced by $p_{a1}ds$ and $p_{a2}ds$ respectively, ν is substituted with ν_m (subscript denotes Poisson's ratio for matrix) and r, $\sin\theta$ and $\cos\theta$ are substituted as in equations 1.19 and 1.20. The stress field is calculated at a point inside the inclusion (Eq. 1.18) and superposed along Γ_a. This results in the stress field $\boldsymbol{\sigma}_a$ caused by the tractions $\mathbf{p}_a$ on the interface Γ_a:

$$\boldsymbol{\sigma}_a = \oint_{\Gamma_a} \begin{Bmatrix} \sigma_x^P \\ \sigma_y^P \\ \sigma_{xy}^P \end{Bmatrix} ds \tag{1.21}$$

As the inclusion is circular, the length ds is expressed as $Rd\alpha$. The integration is performed numerically using a trapezoidal rule. The new stress field inside Γ_a in the homogeneous solid is obtained by:

$$\boldsymbol{\sigma}^* = \boldsymbol{\sigma}_\infty + \boldsymbol{\sigma}_a \tag{1.22}$$

The stress field $\boldsymbol{\sigma}$ inside Γ_a in the heterogeneous solid is found from equation 1.12 using the old value of $\boldsymbol{\Delta\sigma}$. The new, unbalanced stress field $\boldsymbol{\Delta\sigma}$ is calculated using equation 1.7, and tractions $\mathbf{p}_a$ are recalculated from equation 1.11. The calculations are repeated until the change of $\mathbf{p}_a$ becomes small enough. The change is determined on the basis of the norm:

$$||\mathbf{p}_a|| = \oint_{\Gamma_a} |\mathbf{p}_a|\, ds \tag{1.23}$$

where $|\mathbf{p}_a|$ is the length of the vector $\mathbf{p}_a$ equal to $\sqrt{p_{a1}^2 + p_{a2}^2}$ and ds is again substituted by $Rd\alpha$. The convergence criterion is:

$$\frac{||\mathbf{p}_a||^{k+1}}{||\mathbf{p}_a||^k} - 1 \leq e \tag{1.24}$$

where k is the iteration number and e is a given small, acceptable error. The iterative procedure is summarized in Table 1.1.

The procedure converges quite rapidly to the analytical solution (Muskhelishvili [16] and appendix A) which also can be seen from the following example.

The ratio between Young's moduli for the inclusion and matrix material is $E_a/E_m = 23$, Poisson's ratio for the inclusion material is $\nu_a = 0.3$ and Poisson's ratio for the matrix material is $\nu_m = 0.35$. The accepted error is taken to be $e = 0.0001$, the radius of the inclusion is $R = 10\,\text{points}^2$. The tractions applied at the boundaries are $\boldsymbol{\sigma}_\infty = \{0, 1, 0\}^T\,\text{N/mm}^2$ and plane strain is assumed. The procedure converges to the analytical solution with the given precision of the stress components after 9 iterations (Tab. 1.2).

After convergence is reached, the uniform stress field $\boldsymbol{\sigma}$ inside the inclusion is known (Eq. 1.12) and the stress field at any point outside the inclusion may now be determined. This is done by calculating the unbalanced stress field from equation 1.7 using the calculated stress field inside the inclusion. Then the tractions on the interface Γ_a are calculated from equation 1.11. Given any coordinate outside the inclusion equations 1.21, 1.22 and 1.13 can be used to determine the stress field. The solution is an approximation to the analytical solution and its accuracy depends on the numerical integration and the number of iterations. In order to visualize the results the σ_y stress component is shown in figure 1.5.

[2] Points are related to scaleable pixels of an image screen and are scaled depending on magnification.

Table 1.1: The iteration procedure for one inclusion.

initial state $\boldsymbol{\sigma}^{(0)} = \boldsymbol{\sigma}_\infty$

$\boldsymbol{\Delta\sigma}^{(0)} = (\mathbf{D}_m - \mathbf{D}_a)\mathbf{D}_a^{-1}\boldsymbol{\sigma}^{(0)}$

$\mathbf{p}_a^{(0)} = -\boldsymbol{\Delta\bar{\sigma}}^{(0)}\mathbf{n}_a$

iterations $k = 1, 2, \cdots$

$\boldsymbol{\sigma}_a^{(k)} = \oint_{\Gamma_a} \boldsymbol{\sigma}^{P(k-1)}\, ds$

$\boldsymbol{\sigma}^{*(k)} = \boldsymbol{\sigma}_\infty + \boldsymbol{\sigma}_a^{(k)}$

$\boldsymbol{\sigma}^{(k)} = \boldsymbol{\sigma}^{*(k)} - \boldsymbol{\Delta\sigma}^{(k-1)}$

$\boldsymbol{\Delta\sigma}^{(k)} = (\mathbf{D}_m - \mathbf{D}_a)\mathbf{D}_a^{-1}\boldsymbol{\sigma}^{(k)}$

$\mathbf{p}_a^{(k)} = -\boldsymbol{\Delta\bar{\sigma}}^{(k)}\mathbf{n}_a$

stop iteration when $||\mathbf{p}_a||^{(k+1)} \,/\, ||\mathbf{p}_a||^{(k)} - 1 \leq e$

end

Table 1.2: Iterative process for one inclusion.

k	σ_x/σ_∞	σ_y/σ_∞	$\sigma_{xy}/\sigma_\infty$	e_{cal}
1	-0.0753	1.2931	0.0	0.30369
2	-0.1194	1.3848	0.0	0.07800
3	-0.1393	1.4150	0.0	0.02520
4	-0.1474	1.4253	0.0	0.00874
5	-0.1505	1.4290	0.0	0.00312
6	-0.1517	1.4303	0.0	0.00113
7	-0.1522	1.4308	0.0	0.00041
8	-0.1523	1.4309	0.0	0.00015
9	-0.1524	1.4310	0.0	0.00005

1.2 Stress Field for Multiple Inclusions

Contrary to the solution for a single inclusion the stress field interaction between the inclusions must be taken into account. The basic idea of accounting for this interaction is to determine the stress field inside an inclusion as before but also include the interacting stress field from the neighbouring inclusions. More precisely the problem is divided into a number of subproblems corresponding to the number of inclusions (fig. 1.6).

In each subproblem the heterogeneous solid is substituted with a homogeneous solid where an unbalanced stress field has been introduced. But as opposed to the single inclusion problem also the interacting stresses from the remaining inclusions are added

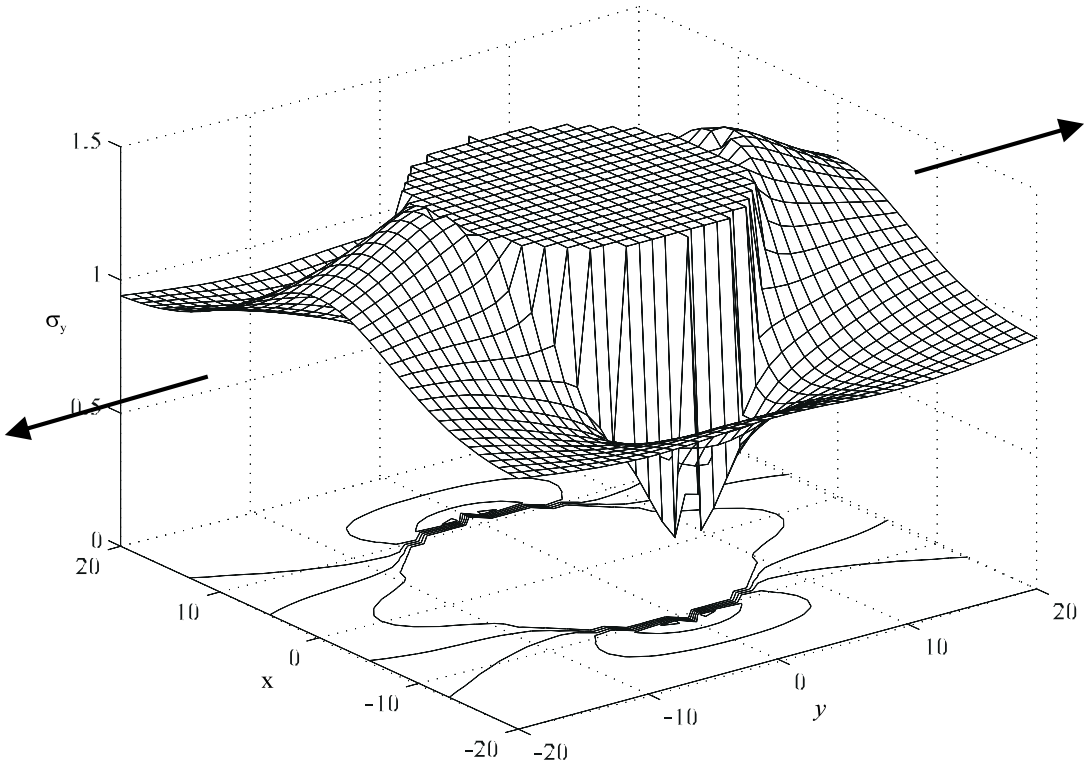

Figure 1.5: σ_y stress component for a single inclusion.

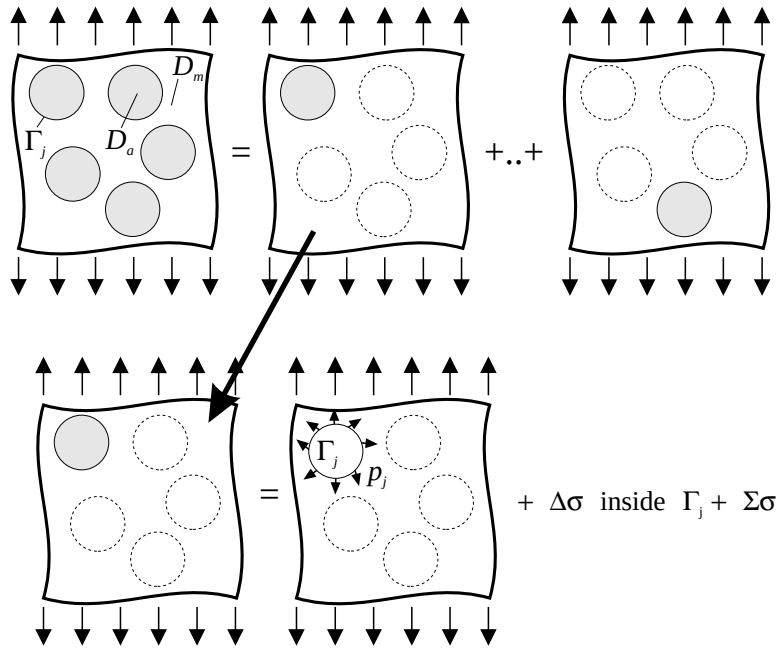

Figure 1.6: Superposition scheme for the plane solid containing multiple inclusions.

to the stress field inside the area covered by the inclusion. In order to establish a method, which accounts for these interaction effects the iterative procedure for the single inclusion is extended.

Now the problem consists of an infinitely extented plane solid containing multiple inclusions, which may be randomly dispersed and subjected to unidirectional uniform tractions $\boldsymbol{\sigma}_\infty$ at the remote boundaries. The solid contains N inclusions all of circular shape, and the boundary curves for the inclusions are denoted Γ_j where $j = 1, \cdots, N$. All the inclusions have the same elastic stiffness $\mathbf{D}_a$ and the matrix has the elastic stiffness $\mathbf{D}_m$. Radii of the inclusions are all equal to R.

In this case, the basic equation for the single inclusion problem (Eq. 1.7) is applied for each inclusion:

$$\boldsymbol{\Delta\sigma}_j = (\mathbf{D}_m - \mathbf{D}_a)\mathbf{D}_a^{-1}\boldsymbol{\sigma}_j \qquad j = 1, \cdots, N \tag{1.25}$$

These unbalanced stresses at each inclusion introduce tractions at the boundaries Γ_j of the inclusions:

$$\mathbf{p}_j = -\boldsymbol{\Delta\bar{\sigma}}_j \mathbf{n}_j \qquad j = 1, \cdots, N \tag{1.26}$$

Similar to equation 1.12 the resulting stress field for each inclusion is determined as:

$$\boldsymbol{\sigma}_j = \boldsymbol{\sigma}_j^* - \boldsymbol{\Delta\sigma}_j \quad \text{inside} \quad \Gamma_j \tag{1.27}$$

where $\boldsymbol{\sigma}_j^*$ is the equilibrium stress field where the homogeneous solid is exposed to tractions $\mathbf{p}_j$ for $j = 1, \cdots, N$ and the applied tractions at the remote boundaries. Thus, the equilibrium stress field is calculated as:

$$\boldsymbol{\sigma}_j^* = \boldsymbol{\sigma}_\infty + \sum_{i=1}^{N} \boldsymbol{\sigma}_{ij} \qquad j = 1, \cdots, N \tag{1.28}$$

where $\boldsymbol{\sigma}_{ij}$ is the stress field at the j'th inclusion as if the i'th inclusion is alone in the matrix. If $j = i$, the uniform stress field inside the j'th inclusion itself is calculated. If $j \neq i$, the i'th inclusion is alone in the matrix and the stress field at the j'th inclusion is calculated. The interacting stresses $\boldsymbol{\sigma}_{ij}$ are calculated as:

$$\boldsymbol{\sigma}_{ij} = \oint_{\Gamma_i} \boldsymbol{\sigma}_{ij}^P \, ds \qquad j = 1, \cdots, N \tag{1.29}$$

where $\boldsymbol{\sigma}_{ij}^P$ are the stress components from equation 1.18. This stress field varies over the region covered by the j'th inclusion but it is only calculated at the centre point. The stress field in all the inclusions is asummed uniform and this is an approximation. The errors in the approximation become insignificant the larger the distance between the inclusions becomes. The extended iterative procedure is shown in table 1.3.

As a starting point $\boldsymbol{\sigma}_{ij}$ is calculated using a standard solution for one inclusion from the complex potential theory (Muskhelishvili [16] and appendix A) and the resulting stress field is $\boldsymbol{\sigma}_j = \boldsymbol{\sigma}_j^*$ as $\boldsymbol{\Delta\sigma}_j = 0$. The resulting stress field at each inclusion $\boldsymbol{\sigma}_j$ is used to calculate the unbalanced stress fields in all the inclusions using equation 1.25. The tractions $\mathbf{p}_j$ at each contour of the inclusions are found using equation 1.26. This is the initial state of the iterative procedure and the iterations start with calculating

Table 1.3: The iteration procedure for multiple inclusions.

---

initial state $\quad \boldsymbol{\sigma}_j^{*(0)} = \boldsymbol{\sigma}_\infty + \sum_{i=1}^{N} \boldsymbol{\sigma}_{ij}^{(0)}$

$\boldsymbol{\sigma}_j^{(0)} = \boldsymbol{\sigma}_j^{*(0)}$

$\boldsymbol{\Delta\sigma}_j^{(0)} = (\mathbf{D}_m - \mathbf{D}_a)\mathbf{D}_a^{-1}\boldsymbol{\sigma}_j^{(0)}$

$\mathbf{p}_j^{(0)} = -\boldsymbol{\Delta}\bar{\boldsymbol{\sigma}}_j^{(0)}\mathbf{n}_j$

iterations $\quad k = 1, 2, \cdots$

$\sum_{i=1}^{N} \boldsymbol{\sigma}_{ij}^{(k)} = \sum_{i=1}^{N} \oint_{\Gamma_i} \boldsymbol{\sigma}_{ij}^{P(k-1)}\, ds$

$\boldsymbol{\sigma}_j^{*(k)} = \boldsymbol{\sigma}_\infty + \sum_{i=1}^{N} \boldsymbol{\sigma}_{ij}^{(k)}$

$\boldsymbol{\sigma}_j^{(k)} = \boldsymbol{\sigma}_j^{*(k)} - \boldsymbol{\Delta\sigma}_j^{(k-1)}$

$\boldsymbol{\Delta\sigma}_j^{(k)} = (\mathbf{D}_m - \mathbf{D}_a)\mathbf{D}_a^{-1}\boldsymbol{\sigma}_j^{(k)}$

$\mathbf{p}_j^{(k)} = -\boldsymbol{\Delta}\bar{\boldsymbol{\sigma}}_j^{(k)}\mathbf{n}_j$

stop iteration when $\quad ||\mathbf{p}_j||^{(k+1)} \,/\, ||\mathbf{p}_j||^{(k)-1} \leq e$

each line is calculated for $\quad j = 1, \cdots, N$

end

---

the interacting stress fields $\boldsymbol{\sigma}_{ij}$ from all inclusions acting upon the j'th inclusion using equation 1.29. The stress fields $\boldsymbol{\sigma}_j^*$ are recalculated using equation 1.28. The resulting stress fields $\boldsymbol{\sigma}_j$ inside the inclusions are found using equation 1.27. The calculations are repeated until the change of $\mathbf{p}_j$ becomes small enough for all N inclusions. The change is determined on the basis of the norm expressed by equation 1.24.

When convergence is reached the stress fields inside the inclusions may be used to calculate the stress field in the matrix. Knowing the resulting stress field in all inclusions, the unbalanced stress field and tractions at the boundaries of the inclusions are easily calculated. The tractions are included in equation 1.29 where j represents the coordinates of the point in the matrix at which the stress field should be calculated. The final stress field is determined by equation 1.28.

For the purpose of comparison the stress field calculated with the presented iterative procedure is compared with the finite element method for the arrangement of inclusions shown in figure 1.7.

The same material parameters as in section 1.1 are used, and the stress field is calculated along the x axis placed between two inclusions above and one inclusion below. The uniform tractions at the remote boundaries correspond to a unit overall stress. Plane stress is assumed and for the three stress components the results from two methods seem to be consistent.

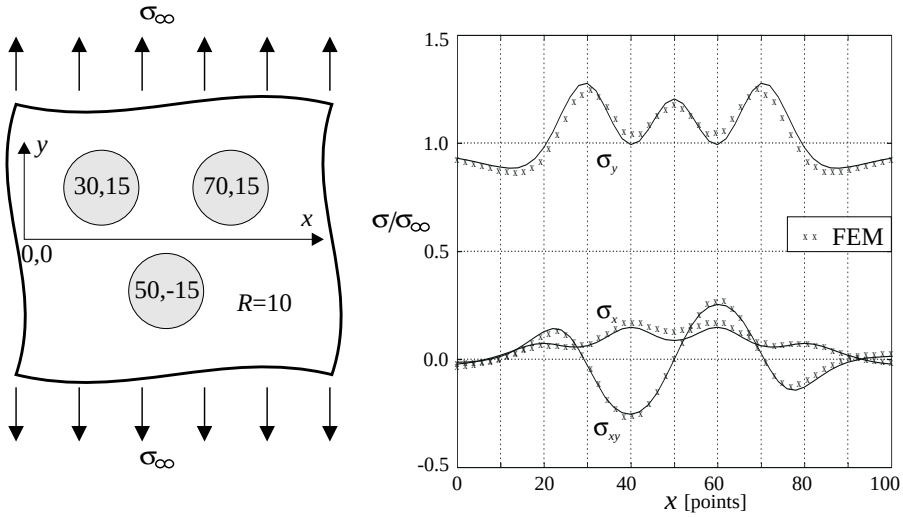

Figure 1.7: Comparison of stress components obtained from the iterative procedure and the finite element method (coordinates are indicated within the fibers in points).

Chapter

2

Determination of Stress Intensity Factors

The method of determining the stress intensity factors for cracks existing in a composite material, where they interact with each other as well as interact with the surrounding inclusions, may be performed in a straight forward manner. It is necessary to account for the interaction effects which arise between the inclusions and cracks in order to obtain the stress field distribution along the crack faces, and a superposition scheme needs to be established.

The distribution of both inclusions and cracks is of vital importance for the determination of stress intensity factors. Unit cells for ordered distributions need only to contain a small area of a distribution whereas unit cells for disordered distributions need to cover a larger area. Therefore, the method needs to account for the interaction effects from multiple inclusions and cracks.

Contrary to the stress analysis method presented in chapter 1 where the stress field is determined through an iterative process, the interacting stress field on a crack is determined directly by applying an averaging technique for the interacting pressure distributions. The stress analysis method is one of the basic elements in the method and is used to include the stress field disturbance from the inclusions. The direct solution includes the use of a transmission factor, which accumulates the amount of interaction only depending on the material properties and the geometrical arrangement of inclusions and cracks.

The literature devoted to fracture mechanics and determination of stress intensity factors is very comprehensive and in the following only works closely related to the present work will be quoted. Erdogan *et al.* [4] presented a method to determine the stress intensity factors for an arbitrarily oriented crack situated in a composite material with sparsely distributed, circular inclusions, i.e. only one inclusion and one crack need to be considered. The method is based on superposition of two problems. One problem, which simply determines the stress field in the matrix as if only the inclusion is present and the solid is exposed to an external load. The second problem takes into account the interaction effect between the inclusion and the crack as if the only external load is at the crack line. The superposition leads to a system of singular integral equations, which are solved numerically. Kachanov [9] presented a method of stress analysis in an elastic solid with multiple randomly distributed cracks using a superposition scheme. The key assumption in Kachanov's methods is to neglect the variation of stresses on

a crack and thus assume uniform average tractions on a crack. Pijaudier-Cabot and Bažant [17] considered the interaction between a crack and an inclusion and a crack and multiple randomly distributed inclusions. The method provides information about the stress field and stress intensity factors. Hu *et al.* [8] considered multiple void–crack interaction. They used a superposition technique to divide the problem into a number of single–hole and single–crack problems, and as analysis tool they applied *the method of pseudotractions.*

In this chapter a superposition scheme, which accounts for the interaction between inclusions and cracks, is derived and discussed in detail. In section 2.1 the stress intensity factors for two interacting cracks in a solid are determined and this includes the derivation of the transmission factor for the particular case of two cracks. In section 2.2 the stress intensity factors are determined for the case of one crack and one inclusion. This also includes derivation of the transmission factor for this particular case. In section 2.3 the superposition scheme is extended to include the interaction between multiple inclusions and cracks using the basic elements of crack–crack and crack–inclusion–crack interaction. During the derivation examples are presented in order to illustrate the method.

2.1 Stress Intensity Factors for Two Cracks

In order to introduce the idea of the superposition scheme a simple example with two interacting cracks is presented in the following. Besides being explanatory, the crack–crack interaction is also one of the fundamental parts in the superposition scheme for multiple inclusions and cracks. It includes the derivation of the *direct transmission factor* denoted by $\mathbf{\Lambda}^D$, which, in the case of two cracks, accounts for the interaction on one crack given the pressure at the other crack. The stress intensity factors for the case of two collinear cracks are determined using the superposition scheme and compared with results from an analytical solution. The derivation of the superposition scheme is based on the type of crack interaction which Kachanov [9] proposed.

The problem to be solved consists of two cracks located in an infinitely extented plane solid which is exposed to unidirectional uniform tractions $\boldsymbol{\sigma}_\infty$ at the remote boundaries. The crack location is arbitrary both with respect to inter–position and the angle at which the cracks are rotated. The crack faces are denoted by Γ_1 and Γ_2 and the cracks have distinct lengths. The problem is substituted with superposition of two subproblems (fig. 2.1).

The first subproblem consists of an infinite continuous solid exposed to tractions at the remote boundaries. The second subproblem consists of the two cracks located in an infinite solid with traction free remote boundaries but with applied pressure distributions at the crack faces corresponding to the first subproblem. An equilibrium equation for each crack may then be written as:

$$\bar{\boldsymbol{\sigma}}'\mathbf{n}_i + \mathbf{p}_i = 0 \qquad \text{on} \quad \Gamma_i \qquad i = 1, 2 \tag{2.1}$$

The first subproblem is easily solved by calculating the stress field $\bar{\boldsymbol{\sigma}}'$ at the imaginary crack lines in their local coordinate system. The second subproblem is solved by dividing it into two additional subproblems each containing only one crack (fig. 2.2).

In each of these new subproblems the cracks are loaded with the yet unknown pressures $\tilde{\mathbf{p}}_1$ and $\tilde{\mathbf{p}}_2$. The unknown pressure distributions consist both of the applied pressure

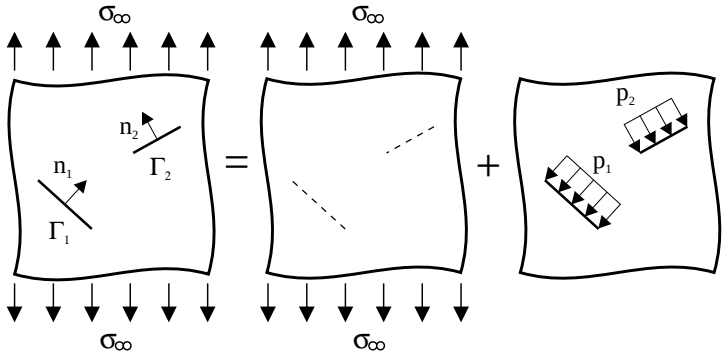

Figure 2.1: Superposition scheme for two interacting cracks located in an infinite solid.

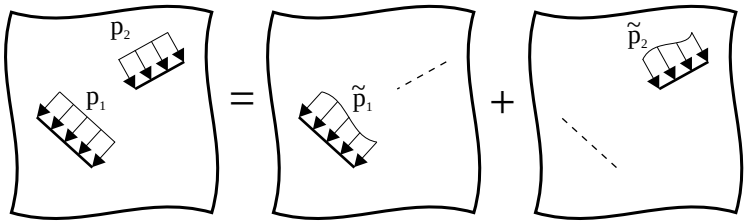

Figure 2.2: Superposition scheme for the crack–crack interaction problem.

calculated by equation 2.1 and interaction terms:

$$\begin{aligned} \tilde{\mathbf{p}}_1 &= \mathbf{p}_1 + \mathbf{p}_{2,int} \qquad \text{on} \quad \Gamma_1 \\ \tilde{\mathbf{p}}_2 &= \mathbf{p}_2 + \mathbf{p}_{1,int} \qquad \text{on} \quad \Gamma_2 \end{aligned} \tag{2.2}$$

The pressure $\mathbf{p}_{2,int}$ is the interacting pressure on crack 1 from the unknown pressure $\tilde{\mathbf{p}}_2$ of crack 2 and vice versa for $\mathbf{p}_{1,int}$. It is assumed that the interacting pressure $\mathbf{p}_{2,int}$ arises due to an average pressure distribution on crack 2 $\langle\tilde{\mathbf{p}}_2\rangle = \langle\mathbf{p}_2\rangle + \langle\mathbf{p}_{1,int}\rangle = \mathbf{p}_2 + \langle\mathbf{p}_{1,int}\rangle$ (the brackets $\langle\ \rangle$ denote averaging over Γ_i). Then, the interacting pressure may be written as a function of the average pressure distribution. The unknown pressure on both crack 1 and 2 is now written as:

$$\begin{aligned} \tilde{\mathbf{p}}_1 &= \mathbf{p}_1 + \mathbf{p}_{2,int}(\langle\tilde{\mathbf{p}}_2\rangle) \qquad \text{on} \quad \Gamma_1 \\ \tilde{\mathbf{p}}_2 &= \mathbf{p}_2 + \mathbf{p}_{1,int}(\langle\tilde{\mathbf{p}}_1\rangle) \qquad \text{on} \quad \Gamma_2 \end{aligned} \tag{2.3}$$

As the interacting pressure depends on an average pressure distribution it is suitable to introduce a transmission factor. This factor relates the average pressure distribution on one crack to the interacting pressure distribution on the other crack. Introducing the transmission factor leads to:

$$\begin{aligned} \tilde{\mathbf{p}}_1 &= \mathbf{p}_1 + \mathbf{\Lambda}^D_{21}\langle\tilde{\mathbf{p}}_2\rangle \qquad \text{on} \quad \Gamma_1 \\ \tilde{\mathbf{p}}_2 &= \mathbf{p}_2 + \mathbf{\Lambda}^D_{12}\langle\tilde{\mathbf{p}}_1\rangle \qquad \text{on} \quad \Gamma_2 \end{aligned} \tag{2.4}$$

The transmission factor is a full 2×2 matrix and is derived as follows. The interacting stress field on crack 1 may be written as:

$$\bar{\boldsymbol{\sigma}}_1 = \bar{\boldsymbol{\sigma}}^t_{21}\langle\tilde{p}_{2,x}\rangle + \bar{\boldsymbol{\sigma}}^n_{21}\langle\tilde{p}_{2,y}\rangle \qquad \text{on} \quad \Gamma_1 \tag{2.5}$$

where $\langle \tilde{p}_{2,x} \rangle$ and $\langle \tilde{p}_{2,y} \rangle$ are the components of the average pressure distribution $\langle \tilde{\mathbf{p}}_2 \rangle$ on crack 2. $\bar{\boldsymbol{\sigma}}^t_{21}$ and $\bar{\boldsymbol{\sigma}}^n_{21}$ are "standard" stress fields generated along the imaginary crack line of crack 1 due to a unit uniform pressure distribution at crack 2 for tangential and normal loading, respectively (appendix B). $\bar{\boldsymbol{\sigma}}_1$ is transformed into the local coordinate system for crack 1 denoted by a prime. In order to express the interacting pressure on crack 1 the transformed stress field is multiplied by a unit outward normal $\mathbf{n}_1 = \{0, 1\}^T$ to crack 1:

$$\begin{aligned}
\mathbf{p}_{2,int} &= \bar{\boldsymbol{\sigma}}'_1 \mathbf{n}_1 \\
&= \bar{\boldsymbol{\sigma}}^{t'}_{21} \mathbf{n}_1 \langle \tilde{p}_{2,x} \rangle + \bar{\boldsymbol{\sigma}}^{n'}_{21} \mathbf{n}_1 \langle \tilde{p}_{2,y} \rangle \\
&= \left\{ \begin{array}{c} \sigma^t_{xy} \\ \sigma^t_{yy} \end{array} \right\}'_{21} \langle \tilde{p}_{2,x} \rangle + \left\{ \begin{array}{c} \sigma^n_{xy} \\ \sigma^n_{yy} \end{array} \right\}'_{21} \langle \tilde{p}_{2,y} \rangle \\
&= \left[\begin{array}{cc} \sigma^t_{xy} & \sigma^n_{xy} \\ \sigma^t_{yy} & \sigma^n_{yy} \end{array} \right]'_{21} \left\{ \begin{array}{c} \langle \tilde{p}_{2,x} \rangle \\ \langle \tilde{p}_{2,y} \rangle \end{array} \right\} \\
&= \boldsymbol{\Lambda}^D_{21} \langle \tilde{\mathbf{p}}_2 \rangle
\end{aligned} \tag{2.6}$$

The transmission factor only depends on the geometrical arrangement of cracks and it may be calculated independently of the magnitude of the uniform pressure $\langle \tilde{\mathbf{p}}_2 \rangle$. Given a point along the imaginary crack line of crack 1 the interacting pressure may now be determined. The direct transmission factor $\boldsymbol{\Lambda}^D_{21}$ represents the crack(2)–crack(1) interaction type and similar to this derivation the transmission factor $\boldsymbol{\Lambda}^D_{12}$ may be expressed.

One way to solve the problem is to average the unknown pressures in equations 2.4 so that the only unknown vectors are $\langle \tilde{\mathbf{p}}_1 \rangle$ and $\langle \tilde{\mathbf{p}}_2 \rangle$. This constitutes four equations with four unknowns and this is easily solved, but as a large number of cracks may be needed in the unit cell, equations 2.4 are solved using another approach. In this solution it is assumed as first order interaction that the unknown pressure used to calculate the interacting pressure equals the applied tractions. The pressure distribution on crack 1 becomes:

$$\tilde{\mathbf{p}}_1 = \mathbf{p}_1 + \boldsymbol{\Lambda}^D_{21} \langle \mathbf{p}_2 \rangle \qquad \text{on} \quad \Gamma_1 \tag{2.7}$$

By calculating the unknown pressure distribution in this way an error arises because all of $\langle \tilde{\mathbf{p}}_2 \rangle$ has not been accounted for. The average pressure on crack 1 now becomes $\langle \tilde{\mathbf{p}}_1 \rangle = \langle \mathbf{p}_1 + \boldsymbol{\Lambda}^D_{21} \langle \mathbf{p}_2 \rangle \rangle = \langle \mathbf{p}_1 \rangle + \langle \boldsymbol{\Lambda}^D_{21} \rangle \langle \mathbf{p}_2 \rangle$. This creates an additional pressure on crack 2 equal to $\boldsymbol{\Lambda}^D_{12}(\langle \mathbf{p}_1 \rangle + \langle \boldsymbol{\Lambda}^D_{21} \rangle \langle \mathbf{p}_2 \rangle)$ and this again creates an additional pressure on crack 1 equal to $\boldsymbol{\Lambda}^D_{21} \langle \boldsymbol{\Lambda}^D_{12} \rangle (\langle \mathbf{p}_1 \rangle + \langle \boldsymbol{\Lambda}^D_{21} \rangle \langle \mathbf{p}_2 \rangle)$. This term accounts for the second order interaction and it is added to equation 2.7 and the pressure distribution for both crack 1 and 2 may now be written as:

$$\begin{aligned}
\tilde{\mathbf{p}}_1 &= \mathbf{p}_1 + \boldsymbol{\Lambda}^D_{21} \langle \mathbf{p}_2 \rangle + \boldsymbol{\Lambda}^D_{21} \langle \boldsymbol{\Lambda}^D_{12} \rangle (\langle \mathbf{p}_1 \rangle + \langle \boldsymbol{\Lambda}^D_{21} \rangle \langle \mathbf{p}_2 \rangle) \qquad \text{on} \quad \Gamma_1 \\
\tilde{\mathbf{p}}_2 &= \mathbf{p}_2 + \boldsymbol{\Lambda}^D_{12} \langle \mathbf{p}_1 \rangle + \boldsymbol{\Lambda}^D_{12} \langle \boldsymbol{\Lambda}^D_{21} \rangle (\langle \mathbf{p}_2 \rangle + \langle \boldsymbol{\Lambda}^D_{12} \rangle \langle \mathbf{p}_1 \rangle) \qquad \text{on} \quad \Gamma_2
\end{aligned} \tag{2.8}$$

The process may be extended to include higher order interactions but their magnitude is insignificant even for small distances between cracks.

It is now possible to calculate the non–uniform pressure distribution on the cracks knowing the applied tractions and the geometrical arrangement of the cracks. Being able to determine the pressure distribution on the crack faces the stress intensity factors for both mode I and II crack opening may be determined using the following singular

integrals:

$$K_I(\pm c) = \frac{1}{\sqrt{\pi c}} \int_{-c}^{c} \sqrt{\frac{c \pm x}{c \mp x}}\, \tilde{\mathbf{p}} \cdot \mathbf{n}\, dx \qquad \text{on} \quad \Gamma_i \tag{2.9}$$

$$K_{II}(\pm c) = \frac{1}{\sqrt{\pi c}} \int_{-c}^{c} \sqrt{\frac{c \pm x}{c \mp x}}\, \tilde{\mathbf{p}} \cdot \hat{\mathbf{n}}\, dx \qquad \text{on} \quad \Gamma_i \tag{2.10}$$

where c is the half crack length, $\mathbf{n}$ is a unit outward normal to the crack faces and $\tilde{\mathbf{p}}$ is the non–uniform pressure on the crack faces.

As an example the stress intensity factors are calculated for the configuration of two collinear cracks shown in figure 2.3. An analytical solution exists for this particular case. The stress intensity factor K_I is normalized with respect to the stress intensity factor K_{I0} for a crack in an infinite, homogeneous solid, in which $K_{I0} = \sigma_\infty \sqrt{\pi c}$.

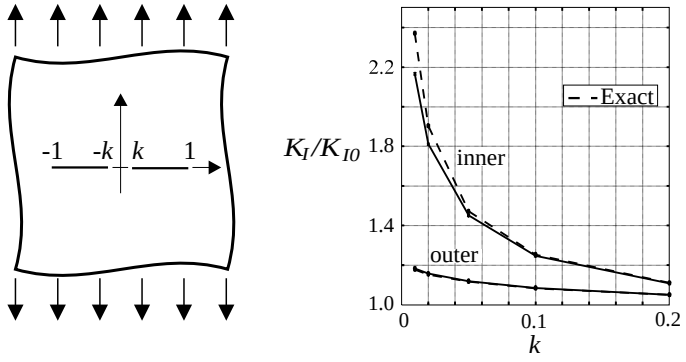

Figure 2.3: Stress intensity factor for a configuration with two collinear cracks.

The stress intensity factors calculated with the presented superposition scheme are compared with the exact results (Tada *et al.* [26]). The calculated stress intensity factors slightly underestimate the exact results at the inner crack tip. If the interaction effects are not included, the stress intensity factors are equal to one.

2.2 Stress Intensity Factors for One Inclusion and One Crack

Another fundamental part of the superposition scheme for multiple inclusions and cracks is the interaction between one inclusion and one crack. It also includes the derivation of a transmission factor and in this case it accounts for the crack–inclusion–crack interaction. The crack creates an interacting stress field inside the inclusion and this again creates an interacting pressure distribution on the crack face. This type of transmission factor is referred to as the *indirect transmission factor* denoted by $\mathbf{\Lambda}^I$. Results from the superposition scheme are compared with results from other similar methods. The basic idea in the superposition scheme was stated by Pijaudier-Cabot and Bažant [17] but as it will be seen later in this section, the method is improved giving more accurate results.

The infinitely extented plane solid, which now consists of both an inclusion and a crack, is subjected to unidirectional, uniform tractions $\boldsymbol{\sigma}_\infty$ at the remote boundaries. The

matrix and inclusion materials of the solid are linear elastic with stiffness $\mathbf{D}_m$ and $\mathbf{D}_a$ respectively. The crack length is $2c$, the radius of the inclusion is R and the crack may be oriented arbitrarily with an angle θ. The boundary curve of the crack and inclusion is denoted Γ_c and Γ_a respectively. Similar to the problem with two cracks presented in the previous section, the problem is divided into two subproblems (fig. 2.4).

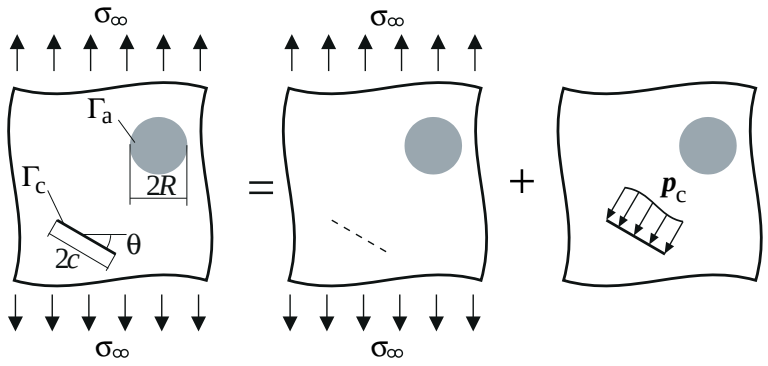

Figure 2.4: Superposition scheme for a crack interacting with an inclusion.

The first subproblem in the superposition scheme consists of the solid containing only the inclusion and loaded by the remote tractions. This problem can be solved by applying the iterative procedure from section 1.1. The second subproblem in the superposition scheme consists of the solid containing the inclusion and the crack with traction free remote boundaries but a pressure distribution corresponding to the first subproblem has been applied to the crack face. By superposition of the two problems, an equilibrium condition for the crack face Γ_c may be written as:

$$\bar{\boldsymbol{\sigma}}'\mathbf{n}_c + \mathbf{p}_c = 0 \qquad \text{on} \quad \Gamma_c \tag{2.11}$$

where $\bar{\boldsymbol{\sigma}}'$ is the stress field solution of the first subproblem calculated in the transformed local coordinate system at the imaginary crack face, and $\mathbf{n}_c = \{0, 1\}^T$ is the outward normal to Γ_c. In the second subproblem the pressure distribution on the crack surface Γ_c causes interface tractions on the inclusion surface Γ_a and this causes an interacting stress field on the crack surface Γ_c. The problem will be solved by dividing it into two other subproblems and applying another superposition scheme (fig. 2.5).

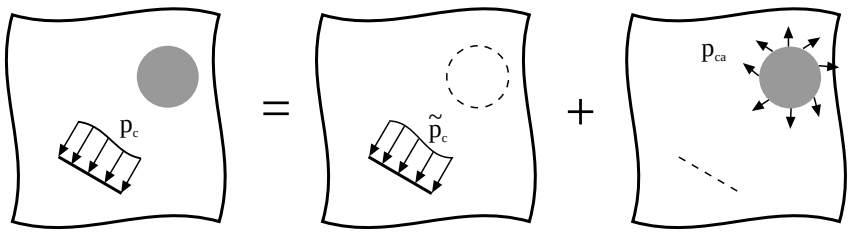

Figure 2.5: Superposition scheme for crack–inclusion–crack interaction problem.

In the first subproblem the solid without the inclusion is loaded by the yet unknown pressure distribution $\tilde{\mathbf{p}}_c$ at the crack surface Γ_c. This causes a stress field $\bar{\boldsymbol{\sigma}}_c$ inside the

imaginary inclusion, which results in interface tractions $\mathbf{p}_{ca} = -\boldsymbol{\Delta}\bar{\boldsymbol{\sigma}}_c\mathbf{n}_a$ on the contour Γ_a. In the second subproblem the solid without any crack but with the inclusion is loaded by the tractions $\mathbf{p}_{ca}$. This causes an interacting pressure distribution $\mathbf{p}_c^a$ on the imaginary crack surface Γ_c. Superposition of the two subproblems yields:

$$\mathbf{p}_c = \tilde{\mathbf{p}}_c + \mathbf{p}_c^a \qquad \text{on} \quad \Gamma_c \tag{2.12}$$

It is assumed that the interacting pressure distribution $\mathbf{p}_c^a$ depends on the average pressure distribution $\langle\tilde{\mathbf{p}}_c\rangle$ and similar to the problem with two cracks a transmission factor is introduced. The transmission factor relates the interaction which $\langle\tilde{\mathbf{p}}_c\rangle$ causes due to the presence of the inclusion. Equation 2.12 may now be rewritten as:

$$\mathbf{p}_c = \tilde{\mathbf{p}}_c + \mathbf{p}_c^a(\langle\tilde{\mathbf{p}}_c\rangle) = \tilde{\mathbf{p}}_c + \boldsymbol{\Lambda}_{cac}^I\langle\tilde{\mathbf{p}}_c\rangle \qquad \text{on} \quad \Gamma_c \tag{2.13}$$

Also in this case the transmission factor is a full 2×2 matrix and is derived as follows. The stress field generated by a uniform load of unit intensity at the crack line is expressed in appendix B. From this the stress field inside the imaginary inclusion is:

$$\bar{\boldsymbol{\sigma}}_c = \bar{\boldsymbol{\sigma}}_c^t\langle\tilde{p}_{c,x}\rangle + \bar{\boldsymbol{\sigma}}_c^n\langle\tilde{p}_{c,y}\rangle \tag{2.14}$$

where $\langle\tilde{p}_{c,x}\rangle$ and $\langle\tilde{p}_{c,y}\rangle$ are the unknown components of the average pressure distribution $\langle\tilde{\mathbf{p}}_c\rangle$ for shear and normal loading, respectively. $\bar{\boldsymbol{\sigma}}_c^t$ and $\bar{\boldsymbol{\sigma}}_c^n$ are the "standard" stress components from the crack for mode II and mode I loading respectively. $\bar{\boldsymbol{\sigma}}_c$ is averaged inside the contour Γ_a, i.e. the stress field is calculated at a number of points inside the imaginary inclusion and $\langle\bar{\boldsymbol{\sigma}}_c\rangle$ is the average value of these quantities. This implies that the stress field inside the inclusion is assumed to be uniform. The unbalanced stress field is calculated according to equation 1.7:

$$\begin{aligned}
\boldsymbol{\Delta}\boldsymbol{\sigma}_c' &= (\mathbf{D}_m - \mathbf{D}_a)\mathbf{D}_a^{-1}\langle\boldsymbol{\sigma}_c'\rangle \\
&= (\mathbf{D}_m - \mathbf{D}_a)\mathbf{D}_a^{-1}(\langle\boldsymbol{\sigma}_c^{t'}\rangle\langle\tilde{p}_{c,x}\rangle + \langle\boldsymbol{\sigma}_c^{n'}\rangle\langle\tilde{p}_{c,y}\rangle) \\
&= \boldsymbol{\Delta}\boldsymbol{\sigma}_c^{t'}\langle\tilde{p}_{c,x}\rangle + \boldsymbol{\Delta}\boldsymbol{\sigma}_c^{n'}\langle\tilde{p}_{c,y}\rangle
\end{aligned} \tag{2.15}$$

where the prime indicates that the stress field has been transformed into the local coordinate system of the inclusion. The interacting tractions on the boundary Γ_a are calculated according to equation 1.11:

$$\begin{aligned}
\mathbf{p}_{ca} &= -\boldsymbol{\Delta}\bar{\boldsymbol{\sigma}}_c'\mathbf{n}_a \\
&= -\boldsymbol{\Delta}\bar{\boldsymbol{\sigma}}_c^{t'}\mathbf{n}_a\langle\tilde{p}_{c,x}\rangle - \bar{\boldsymbol{\sigma}}_c^{n'}\mathbf{n}_a\langle\tilde{p}_{c,y}\rangle \\
&= \mathbf{s}^t\langle\tilde{p}_{c,x}\rangle + \mathbf{s}^n\langle\tilde{p}_{c,y}\rangle
\end{aligned} \tag{2.16}$$

The vectors $\mathbf{s}^t$ and $\mathbf{s}^n$ may be calculated knowing the geometrical arrangement of the inclusion and the crack and the material properties. The two components of $\mathbf{p}_{ca}$ are:

$$\left\{ \begin{array}{c} p_{ca,x} \\ p_{ca,y} \end{array} \right\} = \left\{ \begin{array}{c} s_x^t\langle\tilde{p}_{c,x}\rangle + s_x^n\langle\tilde{p}_{c,y}\rangle \\ s_y^t\langle\tilde{p}_{c,x}\rangle + s_y^n\langle\tilde{p}_{c,y}\rangle \end{array} \right\} \tag{2.17}$$

The components $p_{ca,x}$ and $p_{ca,y}$ are multiplied by ds resulting in the concentrated forces $p_{ca,x}ds$ and $p_{ca,y}ds$ which act along the x and y direction, respectively. Inserting them into equation 1.18 leads to:

$$\bar{\boldsymbol{\sigma}}^P = \mathbf{F}_1 p_{ca,x}ds + \mathbf{F}_2 p_{ca,y}ds \tag{2.18}$$

where $\mathbf{F}_1$ and $\mathbf{F}_2$ are expressed as:

$$\begin{aligned}
\mathbf{F}_1 &= \begin{bmatrix} \frac{-\cos\theta}{2\pi r(1+\kappa)}(4\sin^2\theta - 3 - \kappa) & \frac{-\sin\theta}{2\pi r(1+\kappa)}(4\sin^2\theta - 3 - \kappa) \\ \frac{-\cos\theta}{2\pi r(1+\kappa)}(-4\sin^2\theta - 1 + \kappa) & \frac{-\sin\theta}{2\pi r(1+\kappa)}(4\sin^2\theta - 3 - \kappa) \end{bmatrix} \\
\mathbf{F}_2 &= \begin{bmatrix} \frac{\sin\theta}{2\pi r(1+\kappa)}(4\sin^2\theta - 5 + \kappa) & \frac{\cos\theta}{2\pi r(1+\kappa)}(-4\sin^2\theta + 1 - \kappa) \\ \frac{\sin\theta}{2\pi r(1+\kappa)}(-4\sin^2\theta + 1 - \kappa) & \frac{\cos\theta}{2\pi r(1+\kappa)}(-4\sin^2\theta + 1 - \kappa) \end{bmatrix}
\end{aligned} \tag{2.19}$$

Inserting the right hand side terms from equation 2.17 into equation 2.18 leads to:

$$\bar{\boldsymbol{\sigma}}^P = (\mathbf{F}_1 s_x^t + \mathbf{F}_2 s_y^t)\langle\tilde{p}_{c,x}\rangle ds + (\mathbf{F}_1 s_x^n + \mathbf{F}_2 s_y^n)\langle\tilde{p}_{c,y}\rangle ds \tag{2.20}$$

The stress field caused by the interface tractions $\mathbf{p}_{ca}$ is found by superposing components of equation 2.20 along the contour Γ_a:

$$\begin{aligned}
\bar{\boldsymbol{\sigma}}_c^a &= \oint_{\Gamma_a} \bar{\boldsymbol{\sigma}}^P \, ds \\
&= \langle\tilde{p}_{c,x}\rangle \oint_{\Gamma_a} (\mathbf{F}_1 s_x^t + \mathbf{F}_2 s_y^t) R \, d\alpha + \langle\tilde{p}_{c,y}\rangle \oint_{\Gamma_a} (\mathbf{F}_1 s_x^n + \mathbf{F}_2 s_y^n) R \, d\alpha \\
&= \mathbf{J}^t\langle\tilde{p}_{c,x}\rangle + \mathbf{J}^n\langle\tilde{p}_{c,y}\rangle
\end{aligned} \tag{2.21}$$

The stress field $\bar{\boldsymbol{\sigma}}_a^c$ may now be calculated along the crack line and the interacting pressure distribution is determined as:

$$\mathbf{p}_c^a = \bar{\boldsymbol{\sigma}}_c^{a\prime}\mathbf{n}_c = \mathbf{J}^t\mathbf{n}_c\langle\tilde{p}_{c,x}\rangle + \mathbf{J}^n\mathbf{n}_c\langle\tilde{p}_{c,y}\rangle = \begin{bmatrix} J_{xy}^t & J_{xy}^n \\ J_{yy}^t & J_{yy}^n \end{bmatrix} \begin{Bmatrix} \langle\tilde{p}_{c,x}\rangle \\ \langle\tilde{p}_{c,y}\rangle \end{Bmatrix} = \boldsymbol{\Lambda}_{cac}^I\langle\tilde{\mathbf{p}}_c\rangle \tag{2.22}$$

The transmission factor may be calculated knowing the position of the inclusion and the crack. Once $\boldsymbol{\Lambda}_{cac}^I$ is determined it may be used to calculate the interacting pressure distribution at any point of the crack. The transmission factor $\boldsymbol{\Lambda}_{cac}^I$ represents in this particular case the crack(c)–fiber(a)–crack(c) interaction type.

In order to determine the uniform pressure distribution $\langle\tilde{\mathbf{p}}_c\rangle$ it is assumed that the pressure distribution in equation 2.13 is uniform:

$$\begin{aligned}
\langle\mathbf{p}_c\rangle &= \langle\tilde{\mathbf{p}}_c\rangle + \langle\boldsymbol{\Lambda}_{cac}^I\rangle\langle\tilde{\mathbf{p}}_c\rangle \\
&= (\mathbf{I} + \langle\boldsymbol{\Lambda}_{cac}^I\rangle)\langle\tilde{\mathbf{p}}_c\rangle \qquad \text{on} \quad \Gamma_c
\end{aligned} \tag{2.23}$$

where $\mathbf{I}$ is a 2×2 identity matrix. Averaging $\boldsymbol{\Lambda}_{cac}^I$ over the crack line gives an average interacting pressure. Replacing $\mathbf{p}_c$ with $-\bar{\boldsymbol{\sigma}}'\mathbf{n}_c$ the unknown uniform pressure $\langle\tilde{\mathbf{p}}_c\rangle$ may be determined as:

$$\langle\tilde{\mathbf{p}}_c\rangle = -(\mathbf{I} + \langle\boldsymbol{\Lambda}_{cac}^I\rangle)^{-1}\langle\bar{\boldsymbol{\sigma}}'\mathbf{n}_c\rangle \tag{2.24}$$

The average pressure $\langle\bar{\boldsymbol{\sigma}}'\mathbf{n}_c\rangle$ is found by averaging the stress field calculated along the crack line using the theory from section 1.1. The unknown non–uniform pressure distribution $\tilde{\mathbf{p}}_c$ may now be calculated from equation 2.13 where $\mathbf{p}_c$ is determined from equation 2.11:

$$\tilde{\mathbf{p}}_c = -\boldsymbol{\sigma}'\mathbf{n}_c - \boldsymbol{\Lambda}_{cac}^I\langle\tilde{\mathbf{p}}_c\rangle \tag{2.25}$$

The non–uniform pressure distribution, which takes into account the interaction from the inclusion, may now be inserted into equations 2.9 and 2.10 in order to determine the stress intensity factors for both mode I and II crack opening.

Figure 2.6 and 2.7 show a comparison of stress intensity factors between three methods, Pijaudier-Cabot and Bažant's method, Erdogan's method and the improved method

presented here. Two situations are considered; a radial crack where the stress intensity factors are calculated at both crack tips, and a tangential crack where the stress intensity factors are identical at both crack tips due to the symmetry. The material properties are the same as in section 1.1 and $R/c = 2$, $\theta = 0$.

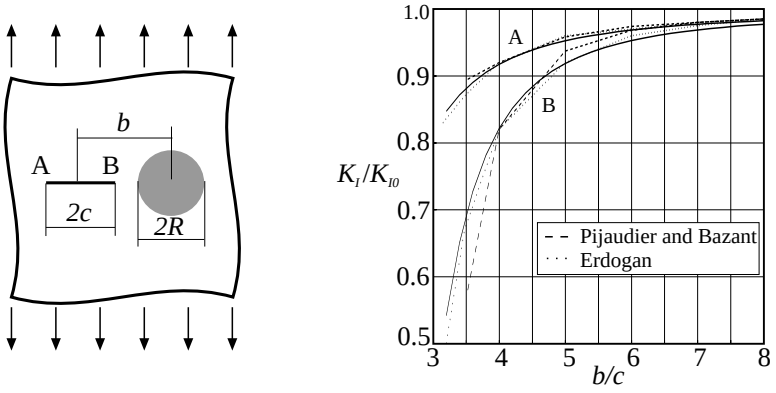

Figure 2.6: Stress intensity factors for a radial crack.

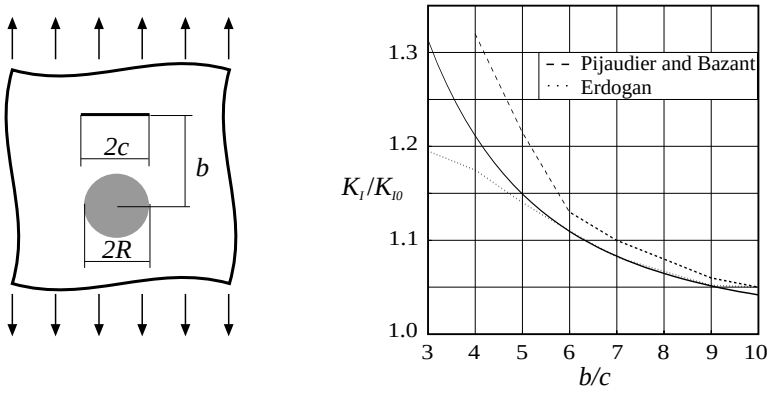

Figure 2.7: Stress intensity factors for a tangential crack.

The comparison shows that for a radial crack the calculation procedure turns out to be very accurate. The stress intensity factors for the tangential crack show that for $b/c < 5$ or $b < 2.5R$ the presented calculation procedure diverges from the other results. Erdogan's solution is assumed to be the most accurate and the results from this method also coincide with finite elements results. Thus comparing the calculation procedure presented here with the procedure that Pijaudier-Cabot and Bažant presented, the results are improved.

Figure 2.8 shows the stress intensity factors for a radial crack as in figure 2.6 for various crack orientation angles. Rotation angle is defined as shown in figure 2.4. The crack is located at $b/c = 4$. The calculations are compared with finite element results showing good agreement in the entire spectrum of the crack orientation angle.

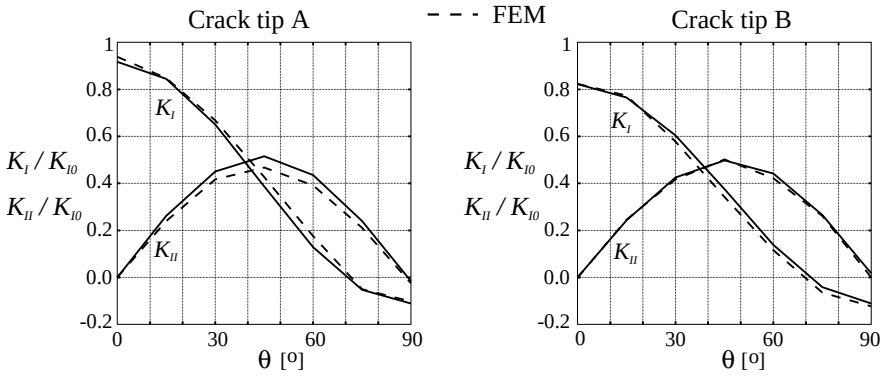

Figure 2.8: Stress intensity factors for various crack orientation angles for a radial crack with $b/c = 4$.

2.3 Stress Intensity Factors for Multiple Inclusions and Cracks

The superposition scheme for multiple inclusions and multiple cracks needs to include additional types of interaction effects. These interaction effects enter the superposition scheme so that the pressure distribution on the cracks accounts for the exact distribution of inclusions and cracks. The superposition scheme results in a unified strategy where various types of interaction effects explicitly may be determined. The basic idea for solving the problem is to combine the solutions of two existing methods. One of the methods, which considers the interaction between multiple cracks, has been presented by Kachanov [9] and is to some extent explained in section 2.1. The other method, which considers the interaction between multiple inclusions and one crack, was stated by Pijaudier-Cabot and Bažant [17] and is explained in sections 1.1, 1.2 and 2.2. The combination between the method states the solution for multiple inclusions and cracks.

The types of interaction effects presented in the previous sections only apply for particular situations, two cracks and one inclusion – one crack, respectively. The additional types of interaction effects, which need to be included, are presented later in this section. All of them involve derivation of the transmission factors but the derivations are omitted in this section as they are similar to the previous derivations. A numerical example with a configuration containing four inclusions and one crack is analysed. The stress intensity factor for the crack is determined using both the method based on the superposition scheme and the finite element method.

The infinitely extented plane solid, which now consists of multiple inclusions and cracks, is subjected to unidirectional, uniform tractions $\boldsymbol{\sigma}_\infty$ at the remote boundaries. The inclusions have all the same stiffness $\mathbf{D}_a$ and the matrix has the stiffness $\mathbf{D}_m$. The solid contains N_1 circular inclusions of radius R. The boundary curves are denoted Γ_i where $i = 1, \cdots, N_1$. The solid also contains N_2 cracks, each with distinct lengths and crack orientation angles denoted by $2c_i$ and θ_i, respectively. The boundary curves for the cracks are denoted Γ_i where $i = N_1 + 1, \cdots, N_1 + N_2$. Both the inclusions and cracks may be randomly located although overlap is not permitted. The problem is solved using

a superposition scheme composed of an initial and a subsidiary problems (fig. 2.9).

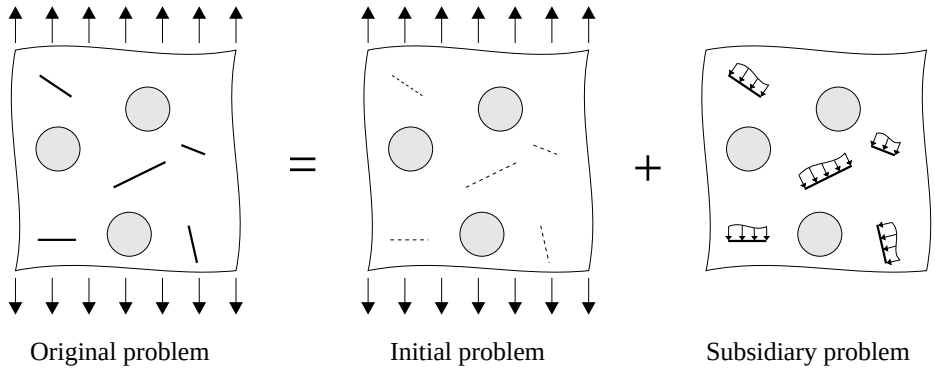

Figure 2.9: Superposition scheme for interaction between multiple inclusions and cracks.

The initial problem consists of the solid containing only the multiple inclusions. The subsidiary problem consists of the solid with traction free remote boundaries, but with tractions corresponding to the stress fields from the initial problem applied at each crack face. The superposition of the initial and subsidiary problem may be written as:

$$\bar{\boldsymbol{\sigma}}' \mathbf{n}_i + \mathbf{p}_i = 0 \qquad \text{on} \quad \Gamma_i \qquad i = N_1 + 1, \cdots, N_1 + N_2 \tag{2.26}$$

The initial problem may be solved using the iterative procedure presented in section 1.2. To solve the subsidiary problem it is divided into N_2 subproblems (fig. 2.10).

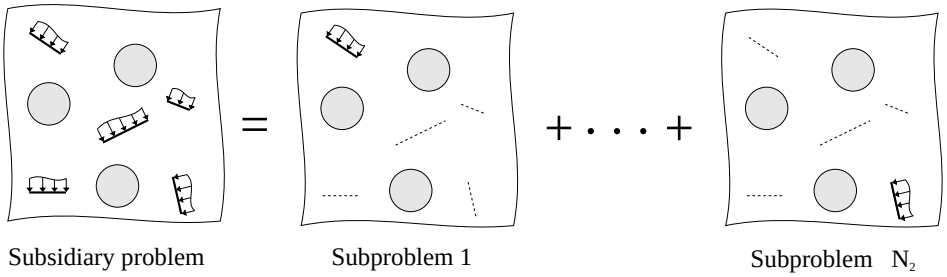

Figure 2.10: Superposition scheme for the subsidiary problem.

For each of the subproblems the interaction effect from both inclusion and imaginary cracks must be taken into account. In the previous sections the interaction effect is determined on the basis of two kinds of interaction. The first one considers the direct interaction between cracks and the second one, called indirect interaction, takes all other interaction effects between inclusions and cracks into account.

Direct Interaction:

The principles of the direct interaction between cracks are explained in section 2.1. The problem is solved using the first and second order interaction effects. The procedure needs to be expanded to include the interaction effects between multiple cracks. The basic idea is to superpose the interacting pressure distribution on one crack from the

other neighbouring cracks. The first and second order interaction effects are illustrated in figure 2.11 where the direct interaction is of interest.

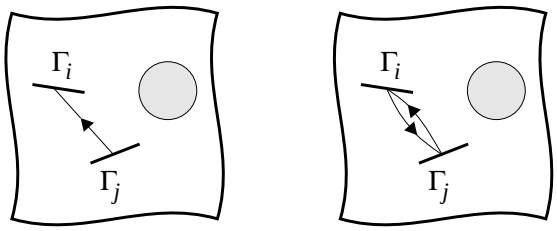

Figure 2.11: First and second order direct interactions.

The procedure in the derivation of the transmission factor between two cracks is the same for all cracks and it only depends on the geometrical arrangement of cracks. Thus the transmission factor $\mathbf{\Lambda}^D_{ji}$ represents the interacting pressure distribution on the i'th crack due to a unit uniform load on the j'th crack. In order to express the interacting pressure $\mathbf{p}^D_i$ on the i'th crack from the direct interaction the effects are superposed and are written as:

$$\mathbf{p}^D_i = \sum_{\substack{j=N_1+1 \\ j\neq i}}^{N_1+N_2} (\mathbf{\Lambda}^D_{ji}\langle \mathbf{p}_j\rangle + \mathbf{\Lambda}^D_{ji}\langle \mathbf{\Lambda}^D_{ij}\rangle(\langle \mathbf{p}_i\rangle + \langle \mathbf{\Lambda}^D_{ji}\rangle\langle \mathbf{p}_j\rangle)) \quad \text{on} \quad \Gamma_i \tag{2.27}$$

where $\mathbf{p}_j$ is the pressure distribution on the j'th crack determined from equation 2.26. Equation 2.27 represents the extension of equation 2.8 to the case of many cracks.

Indirect Interaction:

The principles of the indirect interaction are also presented previously but contrary to section 2.2 new interactions terms are included. Furthermore, the superposition scheme must be applied for multiple inclusions and cracks. Figure 2.12 shows the types of interaction, which are included in the indirect interaction scheme.

The indirect interaction scheme consists of the interaction from a second entity (inclusion or crack) and a third entity which affects the second one. The interaction type is named as follows:

1. crack(i)–inclusion(j)–crack(i)
2. crack(i)–inclusion(k)–inclusion(j)–crack(i)
3. crack(i)–crack(k)–inclusion(j)–crack(i)
4. crack(i)–inclusion(k)–crack(j)–crack(i)
5. crack(i)–crack(j)–crack(i)
6. crack(i)–crack(k)–crack(j)–crack(i)

The letter in the brackets corresponds to the boundary curves Γ and entities with the letter "i" denote first entity, the letter "j" denotes second entity, the letter "k" denotes

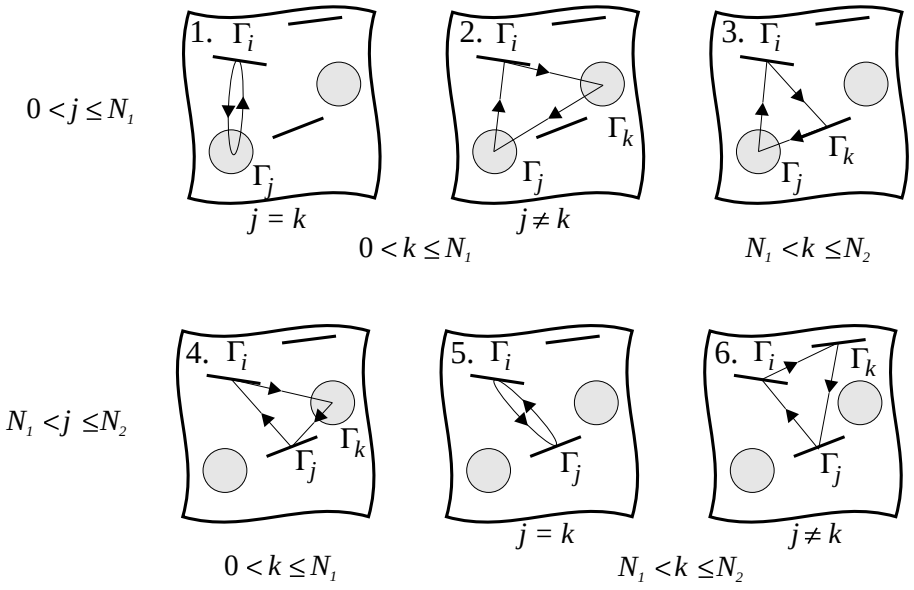

Figure 2.12: Indirect interaction scheme for multiple inclusions and cracks.

third entity. The crack(i)–inclusion(j)–crack(i) interaction type corresponds to the theory presented in section 2.2, but in this case it must be applied for multiple inclusions and cracks. The crack(i)–crack(j)–crack(i) interaction type is identical to the second order term in the direct interaction scheme so this is omitted in the following.

Interaction type 1 sums up the interaction effects on the i'th crack from all the inclusions acting as second entity:

$$\mathbf{p}_i^{I,1} = \sum_{j=1}^{N_1} \mathbf{\Lambda}_{iji}^{I,1} \langle \tilde{\mathbf{p}}_i \rangle \qquad \text{on} \quad \Gamma_i \tag{2.28}$$

where $\langle \tilde{\mathbf{p}}_i \rangle$ is the yet unknown pressure distribution on the i'th crack and the $\mathbf{\Lambda}_{iji}^{I,1}$ is the transmission factor which accounts for the interaction that arises when the pressure distribution on Γ_i creates interface tractions on Γ_j and this returns an interacting pressure distribution on Γ_i.

Interaction type 2 sums up the interaction effects on the i'th crack from all the inclusions where the inclusions act both as second and third entities:

$$\mathbf{p}_i^{I,2} = \sum_{j=1}^{N_1} \sum_{\substack{k=1 \\ k \ne j}}^{N_1} \mathbf{\Lambda}_{ikji}^{I,2} \langle \tilde{\mathbf{p}}_i \rangle \qquad \text{on} \quad \Gamma_i \tag{2.29}$$

The inequality $k \neq j$ is necessary as otherwise it is identical to interaction type 1.

Interaction type 3 sums up the interaction effects on the i'th crack from all the inclusions where the inclusions act as second entity and the cracks act as third entity:

$$\mathbf{p}_i^{I,3} = \sum_{j=1}^{N_1} \sum_{\substack{k=N_1+1 \\ k \ne i}}^{N_1+N_2} \mathbf{\Lambda}_{ikji}^{I,3} \langle \tilde{\mathbf{p}}_i \rangle \qquad \text{on} \quad \Gamma_i \tag{2.30}$$

In this case the inequality $k \neq i$ is introduced in order to avoid that the i'th crack becomes the third entity.

Interaction type 4 sums up the interaction effects on the i'th crack from all the cracks where the cracks act as second entity and the inclusions act as third entity:

$$\mathbf{p}_i^{I,4} = \sum_{\substack{j=N_1+1 \\ j\neq i}}^{N_1+N_2} \sum_{k=1}^{N_1} \mathbf{\Lambda}_{ikji}^{I,4} \langle \tilde{\mathbf{p}}_i \rangle \qquad \text{on} \quad \Gamma_i \tag{2.31}$$

The inequality $j \neq i$ is introduced in order to avoid that the i'th crack becomes the second entities.

Interaction type 6 sums up the interaction effects on the i'th crack from all the cracks where the cracks act both as second and third entity:

$$\mathbf{p}_i^{I,6} = \sum_{\substack{j=N_1+1 \\ j\neq i}}^{N_1+N_2} \sum_{\substack{k=N_1+1 \\ k\neq i, k\neq j}}^{N_1+N_2} \mathbf{\Lambda}_{ikji}^{I,6} \langle \tilde{\mathbf{p}}_i \rangle \qquad \text{on} \quad \Gamma_i \tag{2.32}$$

The inequality $k \neq i$ is introduced in order to avoid that the i'th crack becomes the third entity, the inequality $j \neq i$ is introduced in order to avoid that the i'th crack becomes the second entity and the $k \neq j$ makes sure that the second and third entity are different.

In each of the five interaction types the transmission factor needs to be derived separately as it applies for the particular interaction case. Combining all the terms in this indirect interaction scheme leads to:

$$\mathbf{p}_i^I = \sum_{j=1}^{N_1} \sum_{\substack{k=1 \\ k\neq i}}^{N_1+N_2} \mathbf{\Lambda}_{ikji}^I \langle \tilde{\mathbf{p}}_i \rangle + \sum_{\substack{j=N_1+1 \\ j\neq i}}^{N_1+N_2} \sum_{\substack{k=1 \\ k\neq i, k\neq j}}^{N_1+N_2} \mathbf{\Lambda}_{ikji}^I \langle \tilde{\mathbf{p}}_i \rangle \qquad \text{on} \quad \Gamma_i \tag{2.33}$$

The interaction pressure distribution $\mathbf{p}_i^I$ constitutes the total indirect interaction and it is similar to the interaction term in equation 2.13. ■

By adding the direct and indirect interaction leads to the following equation which is similar to equation 2.12:

$$\begin{aligned} \mathbf{p}_i &= \tilde{\mathbf{p}}_i + \mathbf{p}_i^D + \mathbf{p}_i^I \\ &= \tilde{\mathbf{p}}_i + \sum_{\substack{j=N_1+1 \\ j\neq i}}^{N_1+N_2} (\mathbf{\Lambda}_{ji}^D \langle \mathbf{p}_j \rangle + \mathbf{\Lambda}_{ji}^D \langle \mathbf{\Lambda}_{ij}^D \rangle (\langle \mathbf{p}_i \rangle + \langle \mathbf{\Lambda}_{ji}^D \rangle \langle \mathbf{p}_j \rangle)) \\ &\quad + \sum_{j=1}^{N_1} \sum_{\substack{k=1 \\ k\neq i}}^{N_1+N_2} \mathbf{\Lambda}_{ikji}^I \langle \tilde{\mathbf{p}}_i \rangle + \sum_{\substack{j=N_1+1 \\ j\neq i}}^{N_1+N_2} \sum_{\substack{k=1 \\ k\neq i, k\neq j}}^{N_1+N_2} \mathbf{\Lambda}_{ikji}^I \langle \tilde{\mathbf{p}}_i \rangle \qquad \text{on} \quad \Gamma_i \end{aligned} \tag{2.34}$$

To determine the uniform pressure distribution $\langle \tilde{\mathbf{p}}_i \rangle$ it is necessary to average equation 2.34:

$$\langle \mathbf{p}_i \rangle = \left[\mathbf{I} + \sum_{j=1}^{N_1} \sum_{\substack{k=1 \\ k\neq i}}^{N_1+N_2} \langle \mathbf{\Lambda}_{ikji}^I \rangle + \sum_{\substack{j=N_1+1 \\ j\neq i}}^{N_1+N_2} \sum_{\substack{k=1 \\ k\neq i, k\neq j}}^{N_1+N_2} \langle \mathbf{\Lambda}_{ikji}^I \rangle \right] \langle \tilde{\mathbf{p}}_i \rangle + \langle \mathbf{p}_i^D \rangle \qquad \text{on} \quad \Gamma_i \tag{2.35}$$

The unknown average pressure distribution may then be determined as:

$$\langle \tilde{\mathbf{p}}_i \rangle = \left[\mathbf{I} + \sum_{j=1}^{N_1} \sum_{\substack{k=1 \\ k\neq i}}^{N_1+N_2} \langle \mathbf{\Lambda}^I_{ikji} \rangle + \sum_{\substack{j=N_1+1 \\ j\neq i}}^{N_1+N_2} \sum_{\substack{k=1 \\ k\neq i,k\neq j}}^{N_1+N_2} \langle \mathbf{\Lambda}^I_{ikji} \rangle \right]^{-1} (\langle \mathbf{p}_i \rangle - \langle \mathbf{p}^D_i \rangle) \quad \text{on} \quad \Gamma_i \quad (2.36)$$

where $\langle \mathbf{p}_i \rangle$, which also is to be determined in $\langle \mathbf{p}^D_i \rangle$, is equal to $\langle \bar{\boldsymbol{\sigma}}' \mathbf{n}_i \rangle$. Having found the uniform pressure distribution it is now possible to determine the non–uniform pressure distribution on the i'th crack:

$$\begin{aligned} \tilde{\mathbf{p}}_i &= \mathbf{p}_i - \mathbf{p}^D_i - \mathbf{p}^I_i \\ &= -\bar{\boldsymbol{\sigma}}' \mathbf{n}_i + \sum_{\substack{j=N_1+1 \\ j\neq i}}^{N_1+N_2} (\mathbf{\Lambda}^D_{ji} \langle \bar{\boldsymbol{\sigma}}' \mathbf{n}_j \rangle + \mathbf{\Lambda}^D_{ji} \langle \mathbf{\Lambda}^D_{ij} \rangle (\langle \bar{\boldsymbol{\sigma}}' \mathbf{n}_i \rangle + \langle \mathbf{\Lambda}^D_{ji} \rangle \langle \bar{\boldsymbol{\sigma}}' \mathbf{n}_j \rangle))) \\ &\quad - \left[\sum_{j=1}^{N_1} \sum_{\substack{k=1 \\ k\neq i}}^{N_1+N_2} \mathbf{\Lambda}^I_{ikji} + \sum_{\substack{j=N_1+1 \\ j\neq i}}^{N_1+N_2} \sum_{\substack{k=1 \\ k\neq i,k\neq j}}^{N_1+N_2} \mathbf{\Lambda}^I_{ikji} \right] \langle \tilde{\mathbf{p}}_\mathbf{i} \rangle \quad \text{on} \quad \Gamma_i \end{aligned} \quad (2.37)$$

The stress intensity factors are determined using equation 2.9 and 2.10.

The present method is compared with the finite element method. The configuration consists of four inclusions in a symmetrical arrangement around a crack (fig. 2.13). Material parameters correspond to those used in the previous sections. The radius of the inclusions is R and the crack length $2c$ where $R/c = 2$. The stress intensity factors for both mode I and II are calculated at the crack tips. As the configuration is symmetric only stress intensity factors for one crack tip are depicted.

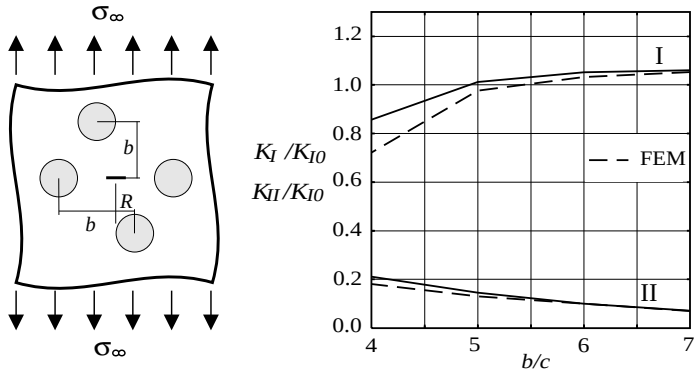

Figure 2.13: Comparison of stress intensity factors between the presented method and the finite element method.

The results from the two methods are consistent for $b/c > 5$ or $b < 2.5R$. This also goes for one inclusion and one crack. With a smaller ratio between Young's moduli of the inclusion and matrix material, the divergence of the results is less pronounced.

The procedure for the determination of the stress intensity factors of randomly dispersed cracks situated among randomly dispersed inclusions is in the following recapitulated:

- The stress components at each imaginary crack line are calculated using the iterative procedure of stress analysis as in section 1.2.
- The transmission factors for the different interaction types, both direct and indirect, are derived in similar way as for equations 2.6 and 2.22
- The uniform pressure distribution on each crack face is determined by applying the averaging technique (Eq. 2.36).
- The non–uniform pressure distribution may then be calculated from equation 2.37.
- The stress intensity factors are then determined from equations 2.9 and 2.10.

Chapter

3

Crack Growth Analysis

The crack growth in a fibrous composite material is of very complex nature as the material has an inhomogeneous microstructure. For the crack growth in the plane cross section perpendicular to the fiber direction cracks may develop in the pure matrix, at the interface between the matrix and the inclusions and through the inclusions. The description of these types of damage may be more or less comprehensive, e.g. the crack growth in the pure matrix is relatively simple to describe if the material is assumed to be perfectly homogeneous. However, considering the matrix on a microscale level the material appears to be inhomogeneous and the crack growth may be difficult to describe. Also if the crack tip meets an obstacle such as a void or an impurity, it may abruptly change its path and maybe also split into two crack paths. Thus it is very difficult to predict the real crack growth in a composite material if all factors must be taken into account and a simplification of the problem is necessary.

In order to estimate the crack path in the material with multiple inclusions and cracks, simple techniques are applied. These techniques may not be sufficient to predict the exact crack evolution in a real material but adequate to indicate a tendency and may lead to a characterization of crack growth depending on dispersion of inclusions and cracks. A complete and thorough investigation seems to be an enormous task for such a complex problem. It may lead to more accurate results, but not necessarily more useful results. Only two types of cracking are considered in the present crack growth analysis; pure matrix cracking without branching and interfacial cracking between the matrix and inclusions. Multiple cracks are considered as well, and adequate crack growth criteria are applied in order to determine the crack trajectories.

The prediction of crack growth plays an important role in the design of real structures. For composite materials, which are inhomogeneous, the crack growth is of much more complex nature than for conventional materials. Experiments (Daniel *et al.* [3]) show that during transverse loading of ceramic matrix composites the microcracks start to grow from the fiber-matrix interface as a radial crack. Also interface cracking occurs and the final crack path consists both of matrix and interface cracks, connected to each other. Sih [25] presented a method, in which the strain–energy–density factor is used to determine the crack extension under combined stress field, in which the crack is allowed to develop in an arbitrary direction. The stress intensity factors for both mode I and II are used to calculate the strain–energy–density factor. To determine whether

the cracks extend or not, the strain–energy–density factor is compared with a material dependent critical value. Zhu and Achenbach [28] presented a model where the crack growth is analysed for two scenarios; radial matrix cracking occurs first followed by interface cracking and vice versa. The interface is modelled with spring elements so that stiffness properties of the interface layer may be varied. The crack growth in the matrix is determined on the basis of a tensile stress criterion and at the interface the strain–energy–density criterion is used.

The pure matrix crack growth is presented in section 3.1 and is determined on the basis of the strain–energy–density factor (Sih [25]). The interfacial crack growth is presented in section 3.2 and is predicted on the basis of the strain–energy–density calculated around the inclusions. In section 3.3 an iterative procedure, which accounts for the crack growth in the case of multiple matrix and interface cracks, is proposed.

3.1 Crack Growth in the Pure Matrix

In order to determine the crack growth of multiple cracks situated among multiple inclusions the theory of the *minimum strain–energy–density* (Sih [25]) is applied. The theory takes into account the mixed mode problem and thus allows cracks to extend in a non–self–similar manner, i.e. during crack growth the crack may change to another mode. This property is necessary because the stress field at the position of the crack consists of both normal and shear loading due to the interaction effects. This means that the crack is exposed to normal loading (mode I) and shear loading (mode II). Therefore, the crack must be allowed to extend in all directions.

The minimum strain–energy–density theory is used in order to determine the crack growth in the pure matrix where the crack is exposed to the interacting stress field. The strain–energy–density factor may be written as:

$$S = a_{11}K_I^2 + 2a_{12}K_IK_{II} + a_{22}K_{II}^2 \tag{3.1}$$

where

$$\begin{aligned} a_{11} &= \frac{1}{16\mu}[(1+\cos\theta)(\kappa-\cos\theta)] \\ a_{12} &= \frac{1}{16\mu}\sin\theta[2\cos\theta-(\kappa-1)] \\ a_{22} &= \frac{1}{16\mu}[(\kappa+1)(1-\cos\theta)+(1+\cos\theta)(3\cos\theta-1)] \end{aligned}$$

where K_I and K_{II} are the stress intensity factors for mode I and II, μ is the shear modulus related to Young's modulus as $E = 2\mu(1+\nu)$, ν is Possion's ratio and κ is an elastic constant, which is $(3-4\nu)$ for plane strain and $(3-\nu)/(1+\nu)$ for plane stress. The only unknown factor in equation 3.1 is the angle θ. The crack length is $2c$, and the local coordinate system (x', y') is attached to it. The angle θ measures the orientation of the crack with respect to a fixed coordinate system (x, y) (fig. 3.1).

The crack extension occurs in the direction, along which the strain–energy–density factor possesses a stationary (minimum) value $\partial S/\partial\theta = 0$. The crack initiates when this minimum value S_0 of the strain–energy–density factor reaches a critical value S_{cr}. The critical value is a material constant related to the fracture toughness of the material

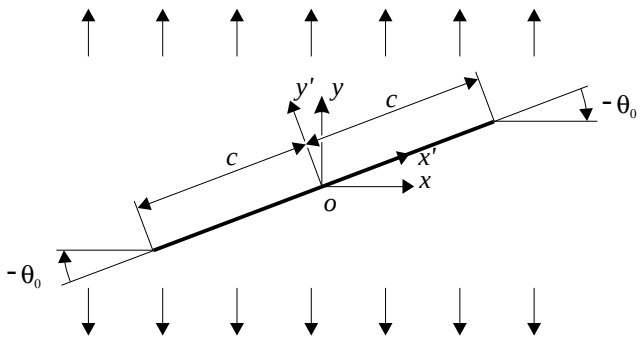

Figure 3.1: Crack geometry for an inclined crack in tension.

under mixed mode conditions. Thus the criterion provides information on whether the crack extends or not and in which angle it extends.

In the case of multiple cracks all the stress intensity factors are calculated and the corresponding minimum strain–energy–density factor S_0 is determined for each crack. It is assumed that the crack with the highest value of S_0 is most likely to extend at first. Whether the crack extends or not depends on the magnitude of the S_{cr}. Further crack growth is then determined from a new analysis where the stress intensity factors are recalculated including the interaction effects from the new crack. As an example of crack growth the configuration with two inclusions and one crack is considered (fig. 3.2).

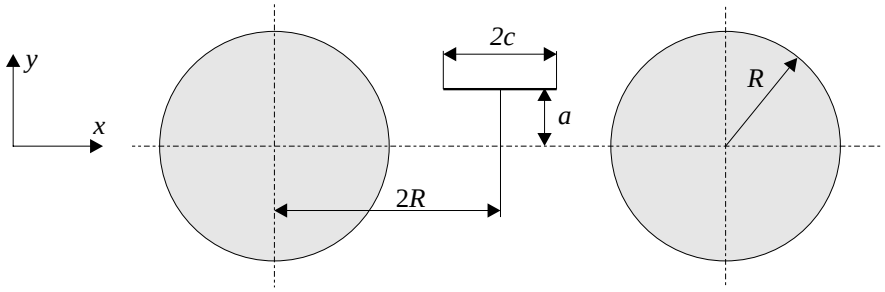

Figure 3.2: Configuration containing two inclusions and one crack.

Unit uniform tractions are applied in the y direction, i.e. normal to the crack surface. The ratio $R/c = 2$ and $a = c$. This configuration is symmetrical with respect to the vertical centre axis of the crack. If the configuration had been symmetrical with respect to the horizontal centre axis, i.e. $a = 0$, the crack would only be exposed to normal loading and thereby only pure mode I would be developed. The material constants are $E_a/E_m = 23$, $\nu_a = 0.3$ and $\nu_m = 0.35$. The variation of the strain–energy–density factor is calculated at the crack tips and S has its minimum value at an angle $\theta_0 = 0.18°$ (fig. 3.3a).

Assuming that the minimum value S_0 of the strain–energy–density factor exceeds the critical value S_{cr} the crack starts to grow. The crack extension length δc is estimated by the following simple relation:

$$\delta c = A_1(|K_I/K_{I0}| + |K_{II}/K_{I0}|)^2 \tag{3.2}$$

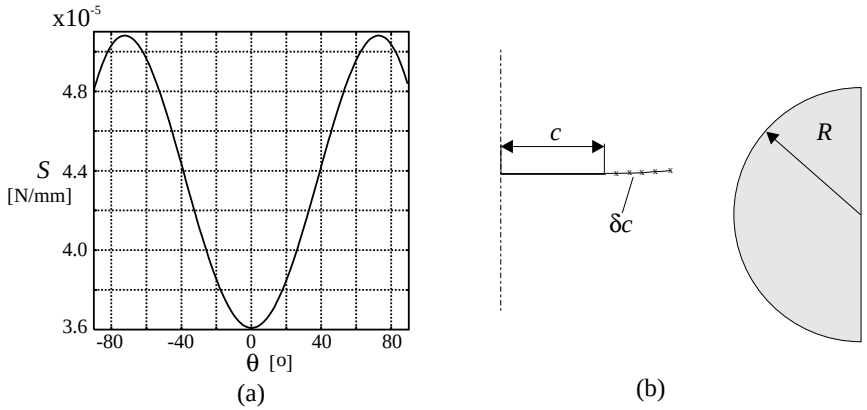

Figure 3.3: (a) Variation of the strain–energy–density factor, (b) the crack path after crack extension.

where A_1 is a constant. After extension the stress intensity factors are calculated at the new crack tip. To find these, K_I and K_{II}, for the new crack tip the interaction effects from the fibers are as usual included in the calculation of the stress field at the position of the new crack, but the interaction effects from the original crack are not included. Two sets of stress intensity factors now exist; one set for the crack tip of the original crack, which did not extend, and one set for the new crack tip. In figure 3.3b the crack path is shown for five crack extensions where the constant $A_1 = 0.5\,\mathrm{mm}$.

3.2 Crack Growth at the Interface

The determination of interface cracking can be of more complex nature than the pure matrix cracking as this includes cracking between dissimilar materials leading to oscillating stress intensity factors and the necessity for exact determination of the stress field. With the method presented in chapter 1 it is possible to calculate the stress field at a very small distance from the interface, but as the method includes an approximation of uniform stress field inside the inclusions, the stress field calculated near the interface will contain an error, which grows when approaching the interface. An error in the stress field will also introduce an error in the calculation of the stress intensity factors. Therefore, it will not be reasonable to calculate the stress intensity factors at the interface and use them to determine the crack growth. Instead a method, which compares the strain–energy–density in a small interface layer with a critical value, is applied.

It is assumed that a small annular layer exists around each inclusion and when cracking occurs it appears at the interface between the small annular layer and the matrix material, i.e. the interface cracking does not occur between the fiber and the annular layer. The stress field calculation may then be performed at a small distance from the inclusion corresponding to the thickness of the annular layer and the errors will not be so pronounced. The thickness of the annular layer as well as the magnitude of the critical value of the strain–energy–density may be chosen so that the real material is simulated. The existence of a small annular layer is readily accepted as the suppliers of the com-

posite materials use coating of the fibers to change the stiffness and strength properties. Also during the manufacturing process the two dissimilar materials interact with each other and create thereby a small interfacial layer. The stiffness properties for the small annular layer are in the numerical procedure the same as for the matrix.

The strain–energy–density is calculated using only stress components, which provoke interface cracking. These are the radial stress component σ_r leading to mode I crack opening and shear stress component $\sigma_{r\theta}$ leading to mode II crack opening. Only non-negative radial stress components are used in the calculations as negative values lead to compression between the crack surfaces. The strain–energy–density U is calculated as:

$$\begin{aligned} U &= \sigma_r \varepsilon_r + \sigma_{r\theta}\varepsilon_{r\theta} \\ &= \sigma_r(\sigma_r D^*_{11} + \sigma_{r\theta} D^*_{13}) + \sigma_{r\theta}(\sigma_r D^*_{31} + \sigma_{r\theta} D^*_{33}) \\ &= \sigma_r^2 D^*_{11} + \sigma^2_{r\theta} D^*_{33} \end{aligned} \tag{3.3}$$

where D^*_{ij} is the compliance and $D^*_{11} = 1/E$, $D^*_{33} = 2(1+\nu)/E$ and D^*_{13} is zero for isotropic materials. When the strain–energy–density U reaches a material dependent critical value U_{cr}, the interface crack propagates. The interface crack model is shown in figure 3.4a and the crack is represented by a straight line intersecting the annular layer. The crack tips are located on the contour of the small annular layer. The strain–energy–density is calculated at the crack tips and compared with the critical value. The strain–energy–density is calculated for the configuration with two fibers and no crack as a function of the circumferential angle α (fig. 3.4b).

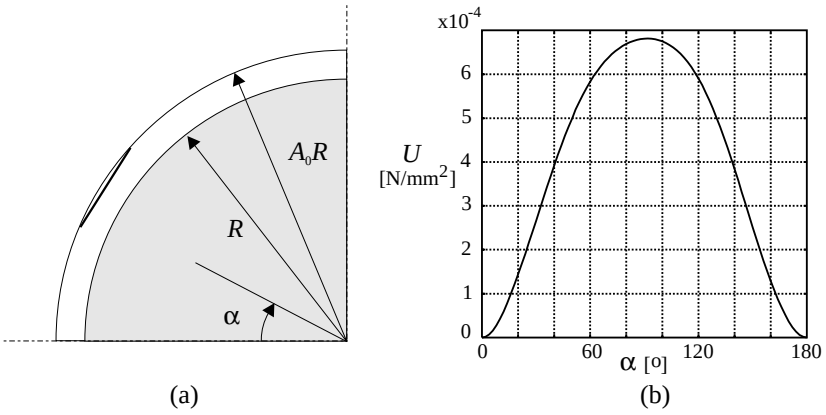

Figure 3.4: (a) Interface crack model, (b) strain–energy–density as a function of the circumferential angle α.

The strain–energy–density has its minimum for $\alpha \approx 0°$ indicating that cracks located here have less tendency to further crack growth than cracks located at $\alpha \approx 90°$ where the strain–energy–density has a maximum. If a crack and more inclusions are present, the magnitude of the strain–energy–density changes depending on the geometrical arrangement of the crack and inclusions.

The strain–energy–density is calculated in order to determine whether the cracks start to grow or not but it does not indicate in which direction the cracks develop. This estimation is made by calculating the principal axes of stress at the crack tips. All stress

components are used in this calculation and it is assumed that the crack extends in the direction of the 1st principal axis of stress. An example is shown in figure 3.5a where the axes of the local coordinate system with origin at the crack tip are denoted 1 and 2.

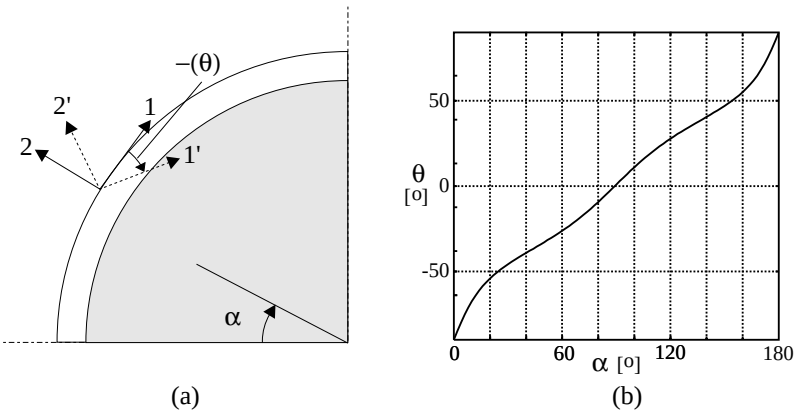

Figure 3.5: (a) Direction of crack extension, (b) crack extension angle θ as a function of the circumferential angle α.

The principal axes of stress are denoted by a prime and it turns out that the crack extends into the annular layer with an angle θ. This angle changes depending on the position and in figure 3.5b the direction of the 1st principal axis of stress as a function of the circumferential angle α is shown. It is obvious that for cracks situated along the interface where $\alpha < 90°$ the crack extension angle is directed towards the inclusion and vice versa for $\alpha > 90°$. This angle changes depending on the local stress field, which again is dependent on the dispersion of inclusions and cracks. Knowing whether the cracks extends or not and in which direction, only the crack extension length is needed. It is found by the following simple relation:

$$\delta c = A_2 U \tag{3.4}$$

where A_2 is a constant. As mentioned, the cracks seem to grow into the inclusion at some locations but as it is assumed that the inclusion is rigid and the crack extends circumferentially around the inclusions, the method must be adjusted. Consider the case where the crack tip of a growing crack is located near an inclusion (point a_1 fig. 3.6).

At this point the strain–energy–density factor is calculated and compared with S_{cr}. If the crack extends, the new crack tip will be located at point a_2 inside the contour defined by radius $A_0 R$. But as this is not permitted the crack tip is moved to point a_3. To determine whether the crack will extend further, the strain–energy–density is calculated and compared with U_{cr}. Again if the crack extends, the new crack tip is located at point a_4, but moved to point a_5. This procedure continues until the new crack tip is located outside the annular layer (point a_6).

At which angle the growing crack diverges into the matrix depends on the local stress field at the crack tip and this is dependent on the dispersion of inclusions and cracks. But also the loading direction is a decisive parameter, and therefore the crack is most likely to diverge at an angle near $\alpha = 90°$. The fact that the strength of the interface may

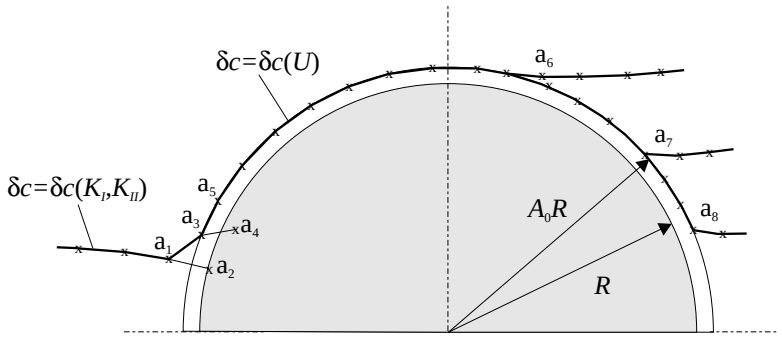

Figure 3.6: Crack trajectory around an inclusion.

be weaker than the strength of the matrix makes it feasible that the crack continues to develop at the interface of angles beyond 90°. In order to include this behaviour another criterion is introduced. The criterion states that if the strain–energy–density calculated at the crack tip is larger than a critical value $\tilde{U}_{cr}$ related to the strength of the interface then the crack continues along the interface regardless of the 1st principal axis of stress. By changing the critical value the diverging angle is changed, e.g. to points a_7 and a_8. Figure 3.4b indicates for the particular situation without any crack that the diverging angle approaches 180° when lowering the critical value of the strain–energy–density. As an example of the influence of the critical value on the crack path, the case where a crack is situated in the vicinity of four inclusions aligned along inclined line can be considered (fig. 3.7).

The crack evolution is seen to change considerably when changing the critical value $\tilde{U}_{cr}$. The critical value for real materials may be estimated by observing when the real crack path coincides with the modelled crack path.

The damage evolution in the configuration shown in figure 3.2 may now be determined by applying the presented two crack growth criteria. Besides the material properties the following data are used: $A_0 = 1.15$, $A_1 = 0.5\,\text{mm}$, $A_2 = 9.5{\cdot}10^2\,\text{mm}^3/\text{N}$, $S_{cr} = 1.2\,\text{N/mm}$, $U_{cr} = \tilde{U}_{cr} = 1.2\,\text{N/mm}^2$. The crack evolution is based on 80 steps and both pure matrix and interface cracking occur in this case (fig. 3.8).

3.3 Combined Crack Growth

The presented crack growth criteria are implemented in the numerical iterative procedure, which accounts for the crack growth in a composite material with multiple inclusions and cracks (Tab. 3.1).

The question whether a matrix or an interface crack starts to grow must, as indicated, be determined using a self–imposed condition. One condition, which can be used, is to compare the normalized values S_0/S_{cr} and U/U_{cr} and let the largest one of these values be decisive for the crack initiation.

Finally, an example consisting of multiple inclusions and cracks is considered. The 48 inclusions are dispersed randomly and 10 cracks are initiated among the inclusions (fig. 3.9).

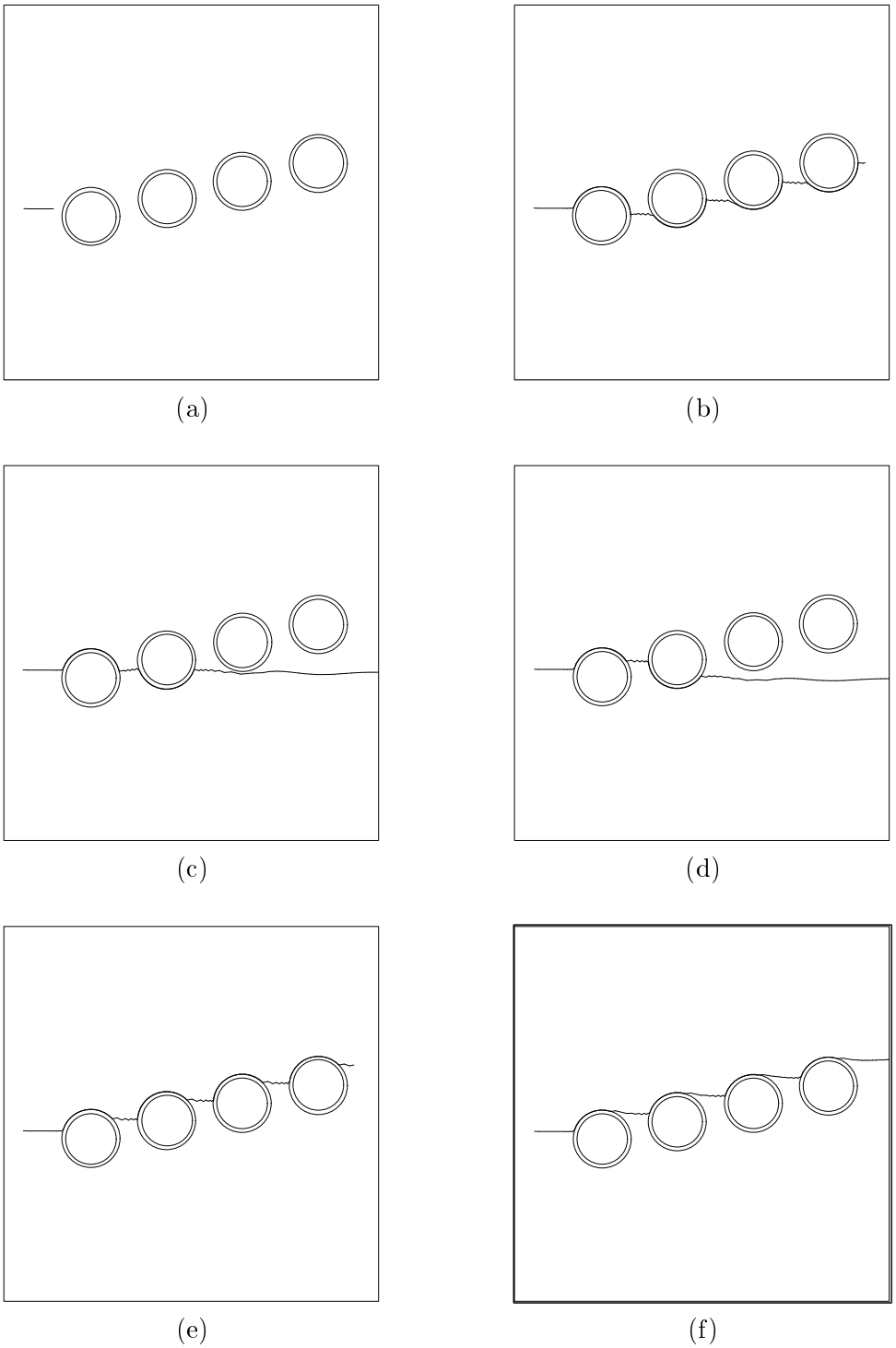

Figure 3.7: Crack path depending on the critical value; (a) initial configuration, (b) $\tilde{U}_{cr} = 0.1\,N/mm^2$, (c) $\tilde{U}_{cr} = 0.5\,N/mm^2$, (d) $\tilde{U}_{cr} = 1.0\,N/mm^2$, (e) $\tilde{U}_{cr} = 1.5\,N/mm^2$, (f) $\tilde{U}_{cr} = 2.0\,N/mm^2$.

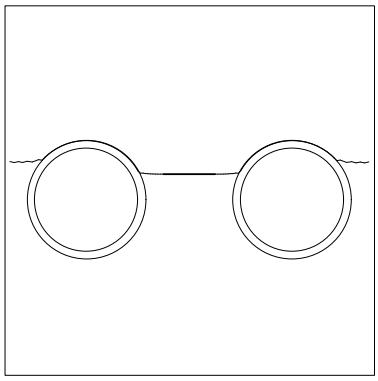

Figure 3.8: Damage evolution for the configuration with two cracks.

Table 3.1: The iterative procedure for the crack growth.

---

initial state Matrix and interface cracks are initiated
Determine the stress field and stress intensity factors
iterations
Calculate S_0 and U for matrix and interface cracks
Determine max(S_0) and max(U)
If $S_{0,max} > S_{cr}$ and $U_{max} > U_{cr}$
– determine whether a matrix or interface crack starts to grow by applying a self–imposed condition
If a matrix crack is to extend
– insert $S_{0,max}$ in equation 3.1 to determine θ_0
– determine crack extension length from equation 3.2
If a interface crack is to extend
– If $U > \tilde{U}_{cr}$ the crack continues immediately at the interface
Else determine 1st principal axis of stress
– determine crack extension length from equation 3.4
Recalculate stress field and stress intensity factors (incl. interaction from the new crack)
stop iteration when enough new cracks has been initiated
end

The material properties used in the model correspond to glass/epoxy and the input data are similar to those applied for the configuration with two fibers (Tab. 3.2).

Both matrix and interface cracks appear in this configuration and the final damage evolution is based on 250 steps. The computational time increases as new cracks are created because the interaction from the new cracks must be taken into account.

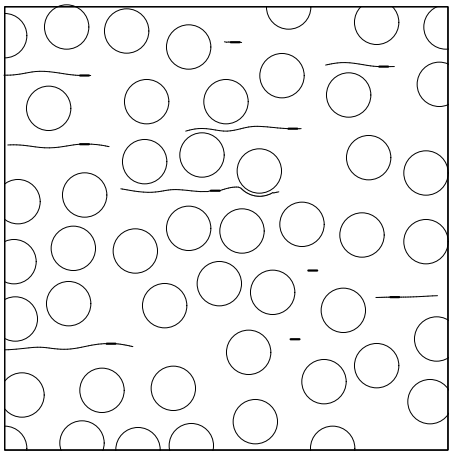

Figure 3.9: Damage evolution for the configuration with 48 inclusions and 10 cracks.

Table 3.2: Input data for the configuration with 48 inclusions and 10 cracks.

E_a	ν_a	E_m	ν_m	A_0	A_1	A_2	S_{cr}	U_{cr}	$\tilde{U}_{cr}$
[N/mm^2]		[N/mm^2]			[mm]	[mm^3/N]	[N/mm]	[N/mm^2]	[N/mm^2]
73000	0.3	3174	0.35	1.15	0.5	$9.5 \cdot 10^2$	1.2	1.2	1.2

Chapter

4

Quantification of the Microstructure Morphology

Having established methods to calculate the stress field, the stress intensity factors and the crack growth for a microstructure consisting of multiple inclusions and multiple cracks, other features related to the microstructure are now introduced. The analysis methods presented previously take into account the exact position of inhomogeneities (inclusions and cracks) but not how the constitution of the microstructure is characterized. The characterization may be accomplished by applying spatial statistics to the dispersion of inhomogeneities. Thus, it is interesting to relate the morphology of the microstructure to various properties of the material.

Inherent to the features related to the microstructure is the construction of a unit cell similar to the concept used in finite element modelling and other corresponding methods. In these analyses the microstructure is assumed to have some form of regularity and unit cells need only to include a part of the microstructure. The microstructure is then envisioned as a repetitious structure composed of the unit cells. In case of a disordered microstructure the unit cell must be enlarged to contain a pattern of inhomogeneities, which is representative throughout the microstructure of the composite material. Furthermore, as the microstructure needs to be described by statistical functions and parameters the unit cell must contain a sufficient number of inhomogeneities.

A feature related to the microstructure, which seems to be of interest, is the morphology of the microstructure, i.e. the geometrical arrangement of the inclusions and cracks. As the morphology of real inhomogeneous materials is ambiguous, it calls for methods to characterize the dispersion of inclusions and cracks. In this way it is possible to recognize and distinguish the different microstructures by means of spatial statistics. Having methods of characterization, different distributions may be classified so that a particular microstructure belongs to a pre–defined class. The key issue here is that only a few types of distributions corresponding to the number of classes need to be investigated in order to predict the response from a given microstructure. By comparing the given microstructure with the classified microstructures, for which knowledge has been accumulated, it is possible to estimate the properties of the material. This classification is used to decompose the ambiguity of the microstructure. The method may of course lead to some uncertainties, but immense time–saving makes it attractive. The different types

of distributions may include regular distributions, complete random distributions and everything in between, so it is necessary to select a few types, which are representative for some unidirectional fibrous composite materials. Distributions may be characterized and differentiated from each other by applying statistical descriptors to the geometrical arrangement of inclusions and cracks.

When calculating the response from a composite material, it is normally assumed that the dispersion of inhomogeneities has some form of regularity. This implies that all inclusions are exposed to the same amount of interaction and in order to include the non–regularity of fibers in real microstructures Brockenbrugh *et al.* [2] compared the elastic and plastic response from different regular distributions and a random distribution by use of finite element models. The regular distributions were modelled with unit cells containing only one fiber whereas the unit cell for the random distribution contained several fibers. As a result they showed that the plastic response was very much affected by the arrangement of inclusions. Therefore the arrangement of inclusions is important when calculating the properties of composite materials. The first step to understand the influence of the arrangement of inhomogeneities is to be able to describe the microstructure. In Pyrz [18] real and simulated microstructures of unidirectional fibrous composite materials are analysed using spatial statistics. Parameters and functions are used to characterize and distinguish different patterns of fibers. A further characterization of distributions of fibers by means of statistical descriptors has been carried out in Pyrz [19]. Also a classification of patterns has been established and analysed. Ways of determining the range of local geometrical disorder are presented in Pyrz [20] and functions, which take into account related field quantities of the microstructures, are investigated.

In section 4.1 a concept for the unit cell is introduced and the size of it is among other things determined by considering the interacting stress field between inclusions. In section 4.2 statistical descriptors, which take into account the local disorder, are applied in order to distinguish between various microstructures.

4.1 Construction of the Unit Cell

In order to perform the same type of analysis on the different classes of distributions as well as establishing a unified concept the construction of a unit cell is necessary. The unit cell must consist of the actual distribution, which is going to be analysed, and it must be possible to expose the distribution to given boundary conditions. The actual distribution of inclusions and cracks becomes representative for the whole microstructure of the material in a statistical sense. Thus, describing the whole microstructure or just the microstructure contained within the unit cell using statistical functions and parameters must lead to the same result. The boundary conditions may be given in form of other inclusions and cracks dispersed outside the actual distribution. The unit cell is then formed by a *sample area*, in which the actual distribution is generated, and this area is surrounded by a *boundary area* which interacts with the sample area. In the boundary area inclusions and cracks may be dispersed independently of the actual distribution so the same boundary conditions can be applied for various actual distributions.

The minimum number of inhomogeneities needed in order to provide statistical data is approximately 100 and in some of the subsequent analyses the sample area, which is defined as a square array, consists of 512×512 points which also limit the number of

possible locations of inhomogeneities. If 100 inclusions, each of radius 10 points, are dispersed within the sample area, then the maximum volume fraction is $\approx 12\%$. Parts of the inclusions may be located beyond the edge of the sample area but their centres are contained within the sample area. Therefore, the indicated volume fraction is a maximum value assuming that no parts of the fiber are beyond the edge of the sample area. The size of the boundary area may be chosen on the basis of *zone of influence* calculations. Thus knowing how far inclusions must be apart so that the interaction can be neglected, provides information of the size of the boundary area. A configuration, which is of importance in zone of influence calculations, is the interaction between two inclusions (fig. 4.1).

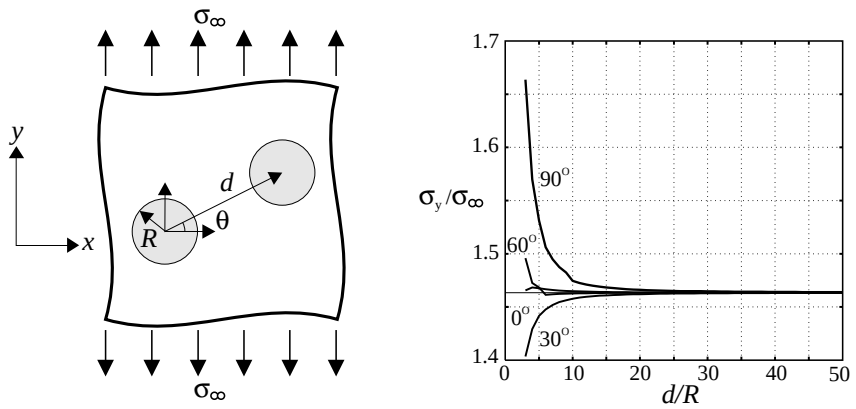

Figure 4.1: Zone of influence for two inclusions with varying inter–distance and inter–orientation represented by the σ_y stress component.

The σ_y stress component is calculated in one of the inclusions for varying inter–distances and inter–orientations. For $\theta = 0^\circ$ corresponding to horizontally aligned inclusions, the influence is almost insignificant compared to the others where the influence has the largest effect for $\theta = 90^\circ$ due to the direction of the applied load. Taking all inter–orientations into account the influence is negligible when the ratio between the inter–distance d and radius of the inclusion R becomes larger than 20. For the unit cell with a sample area consisting of 512×512 points the boundary area must be at least 200 points wide. The interaction which arises when several inclusions are located in a row is also important. Therefore, the zone of influence between multiple verticaly aligned inclusions is considered (fig. 4.2).

The σ_y stress component is calculated in the "0" inclusion when successively adding more inclusions. In this case the stress component increases when adding more inclusions but the slope of the curve decreases at approximately $i \approx 8$. This means that the distance, at which the interaction becomes insignificant, is $d_8 = 24R$ and the boundary area must be at least 240 points if the sample referred to previously is considered. If the inclusions are aligned horizontally, a corresponding tendency is found but the effect will be less pronounced.

The zone of influence calculations provides information which may be used to determine the size of the boundary area. In this particular case with a sample area consisting of

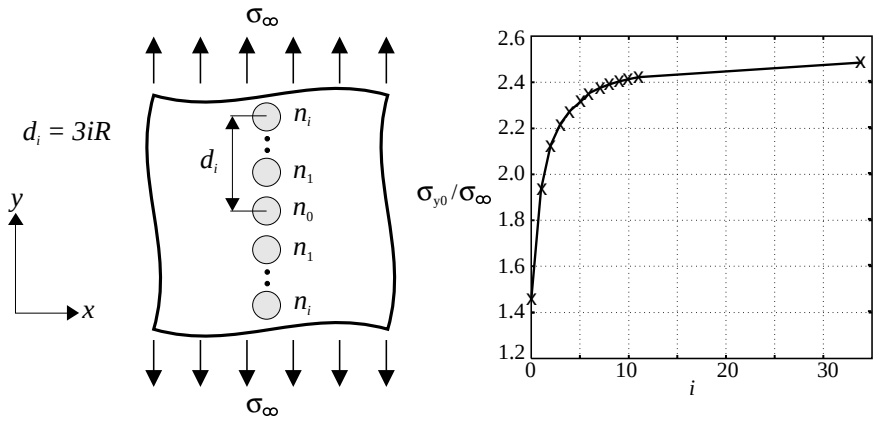

Figure 4.2: Zone of influence calculated for successively added inclusions represented by the σ_y stress component in inclusion "0".

512×512 points the boundary area must be at least 240 points wide on each side of the sample area so by making the whole area 1024×1024 points the conditions are fulfilled (fig. 4.3).

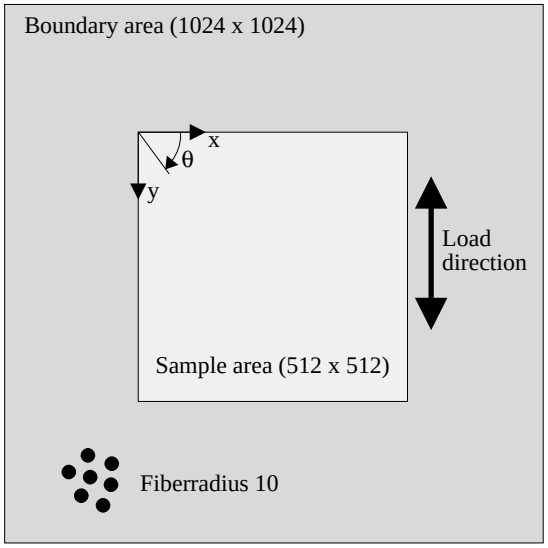

Figure 4.3: Unit cell.

Inclusions may now be dispersed randomly within the unit cell and if the same volume fraction is desired in all parts of the unit cell the number of inclusions in the boundary area must be 3 times the number of inclusions in the sample area. The size of the unit cell may of course be chosen in a different way, but the one presented here forms the basic concept. For radius equal to 10 points the appropriate number of inclusions lies between 100 - 300. Cracks may also be dispersed in the unit cell and similar zone of influence calculations can be performed in order to obtain the acceptable size of the unit cell.

4.2 Geometrical Characterization of Point Patterns

The characterization of microstructures may be performed by applying spatial statistics in which the positions of inclusions and cracks are taken into account. But before the methods of characterization are presented it is necessary to establish a few representative classes of distributions. The choice of distribution classes must rest upon a qualified subjective selection and in agreement with Pyrz [20] four classes of distributions are chosen and are called: *regular*, *hard–core*, *single cluster* and *triple cluster* (fig. 4.4).

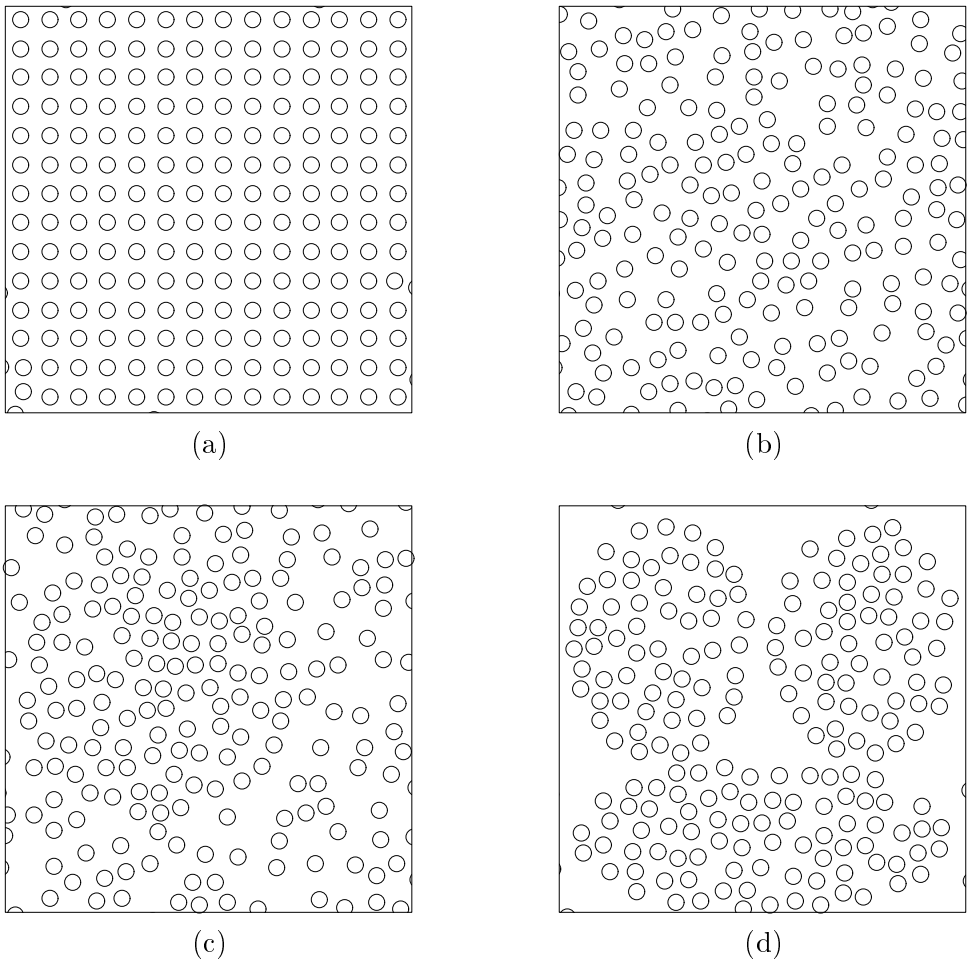

Figure 4.4: Distribution classes; (a) regular, (b) hard–core, (c) single cluster, (d) triple cluster.

The distributions contain approximately 200 inclusions dispersed in the sample area made of 512×512 points. The radius of the inclusions is 10 points and boundary conditions are not subscribed in this particular case. The distributions represent four distinct categories, to which some real microstructures may belong in the statistical sense. Other inhomogeneities may also be represented by the distributions as long as they can be described by a point pattern. The distributions represent in the following inclusions described by their centre points. The regular distribution corresponds to the normally

assumed dispersion of inclusions and is used as reference distribution when comparing different parameters for the material. The distribution is generated as a square array with equal distance between inclusions in the vertical and horizontal directions. The inclusions in the hard–core model are dispersed in such a way that the x and y coordinates are chosen independently using a uniform, random distribution except that the inclusions are not allowed to overlap. In the uniform, random distribution each point is equally likely to be chosen. The single cluster distribution consists of a dense dispersion of inclusions within an enclosed area (cluster). Inside the cluster the inclusions are dispersed using the hard–core conditions. Outside the cluster the inclusions are sparsely dispersed using the hard–core model. The triple cluster has three randomly dispersed clusters in which inclusions are dispersed using the same procedure as for single cluster but contrary to this no inclusions are generated outside the clusters and this introduces matrix rich areas.

Another interesting class of distribution is the *Poisson* distribution. In this distribution, points are dispersed in such a way that each position is equally likely to be chosen regardless of the finite dimension of inclusions. The inter–point distances form a Poisson distribution. This type of distribution has no physical interest when dealing with real microstructures as the inter-point distances may be zero, but as a statistical distribution it serves as a useful comparison.

Although the different distributions may be characterized and separated visually, it is also useful to apply statistical descriptors. The statistical descriptors can be various functions depending on the geometrical arrangement of points. One parameter, which is of interest, is the inter–inclusion distance and a characterization of this may be performed by considering the *nearest neighbour distance*, *second–order intensity function* and *pair distribution function*. These spatial descriptors have been applied in the description of fibrous composite materials by Pyrz [18], [19], [20] and [21] and the following analysis serves as a presentation of the descriptors. They are applied in the characterization of the distributions shown in figure 4.4 and various properties of the descriptors are investigated in order to verify their ability towards the distinction of point's patterns.

Nearest Neighbour

The nearest neighbour distance for an inclusions is determined by the distance to the nearest inclusion measured by inclusion centres. Thus, the number of data for a distribution corresponds to the number of inclusions. For the four classes of patterns the nearest neighbour distances are determined and the normalized cumulative distributions of the data are shown in figure 4.5a.

The cumulative distribution is normalized with respect to the total number of inclusions and the various distributions are easily distinguished. The triple cluster distribution has the steepest curve as the inclusions are densely dispersed leading to small nearest neighbour distances. This also holds for the single cluster distribution. This is caused by the hard–core distribution outside the cluster, in which the inclusions are sparsely dispersed. For the regular distribution the nearest neighbour distance is deterministic and only one distance can be detected. The statistical data are given in form of discrete values and in order to obtain consistency in the description the cumulative data have been curve–fitted with the following continuous function:

$$F(x) = 1 - e^{-m(x-x_{min})^n} \tag{4.1}$$

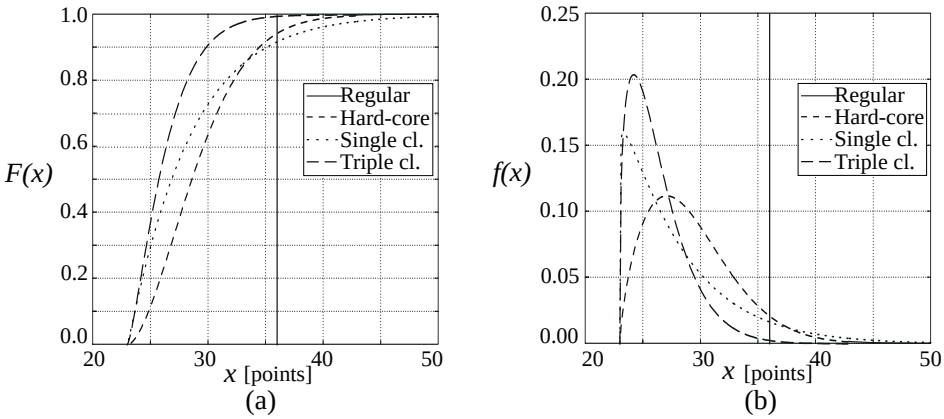

Figure 4.5: The nearest neighbour distances determined for the four classes of patterns expressed as; (a) normalized cumulative distribution, (b) probability density function.

where x is the nearest neighbour distance and x_{min} is the minimum nearest neighbour distance detected. The parameters m and n are found by the method of least–square curve–fitting. The function corresponds to the Weibull distribution function. By differentiation of equation 4.1 with respect to x:

$$f(x) = mn(x - x_{min})^{n-1}\, e^{-m(x-x_{min})^n} \tag{4.2}$$

The function $f(x)$ is the probability density function for nearest neighbour distances (fig. 4.5b). Also, the probability density function is able to distinguish between different patterns. Here it is seen that the triple cluster distribution has the most frequently nearest neighbour distance at $x \approx 24$ points. For the single cluster and hard–core distribution the curves are flatten out. Again only one distance is possible in the regular distribution. Having the discrete data and an expression for the probability density, the statistical moments may be calculated according to table 4.1.

The statistical moments can be used to describe various distributions of data and they are calculated for the four distribution classes using both the continuous and the discrete method (Tab. 4.2).

The statistical moments also provide information about the distributions and the four classes may be distinguished. There is good agreement between the moments calculated with the continuous and the discrete functions and as expected the mean value of nearest neighbour distance for the triple cluster distribution is the lowest as inclusions are dispersed very close. Another conspicuous observation is that the variance of the single cluster distribution is larger than for the other distributions. This is caused by the existence of both a dense distribution inside the cluster area leading to small inter–inclusion distances and a dilute distribution outside the cluster area leading to large inter–inclusion distances. For the point's patterns as presented here the determination of the nearest neighbour distances serves as an informative descriptor.

Table 4.1: Continuous and discrete functions for determining the statistical moments.

Parameter		Continuous	Discrete
Mean	μ	$\int_{-\infty}^{+\infty} x f(x)\,dx$	$\frac{1}{N}\sum_{j=1}^{N} x_j$
Variance	σ^2	$\int_{-\infty}^{+\infty} (x-\mu)^2 f(x)\,dx$	$\frac{1}{N-1}\sum_{j=1}^{N}(x_j-\mu)^2$
Standard deviation	σ	$\sqrt{\sigma^2}$	$\sqrt{\sigma^2}$
Mean deviation	σ_m	$\int_{-\infty}^{+\infty} \lvert x-\mu\rvert f(x)\,dx$	$\frac{1}{N-1}\sum_{j=1}^{N}\lvert x_j-\mu\rvert$
Coefficient of skewness	η	$\frac{1}{\sigma^3}\int_{-\infty}^{+\infty} (x-\mu)^3 f(x)\,dx$	$\frac{1}{N}\sum_{j=1}^{N}\left(\frac{x_j-\mu}{\sigma}\right)^3$

Table 4.2: Statistical moments for the four distribution types calculated using both continuous and discrete functions (the latter ones are shown in brackets), distances are measured in points.

Parameter	Regular	Hard–core	Single cluster	Triple cluster
μ	36	29.2 (29.7)	28.3 (28.9)	26.3 (26.8)
σ^2	–	14.3 (14.3)	25.7 (26.4)	6.5 (6.1)
σ	–	3.8 (3.8)	5.1 (5.1)	2.6 (2.5)
σ_m	–	3.0 (3.0)	3.8 (3.7)	2.0 (2.0)
η	–	0.9 (0.9)	1.9 (1.9)	1.3 (1.0)

The second–order intensity function

Another function, which can be used to discriminate different point patterns, is the second–order intensity function, for which the theoretical derivation is presented in Ripley [24]. The function is defined as the number of further points expected to lie within a distance r of an arbitrary point divided by the number of point per unit area. The second–order intensity function is written as:

$$K(r) = \frac{A}{N^2}\sum_{k=1}^{N}\frac{I_k(r)}{w_k} \tag{4.3}$$

where A is the sampling area, N is the total number of points in the sample, $I_k(r)$ is the number of points within a circle with centre at point k and radius r, w_k is a correction

factor, which is calculated as the proportion of the circumference contained within A to the whole circumference with radius r. The correction factor is included if points outside the sampling area are not taken into account in the calculation of $K(r)$. The second–order intensity function calculated for an infinite Poisson distribution is exactly πr^2. For the four classes of distributions and the Poisson distribution the second–order intensity function is calculated in order to make a comparison (fig. 4.6).

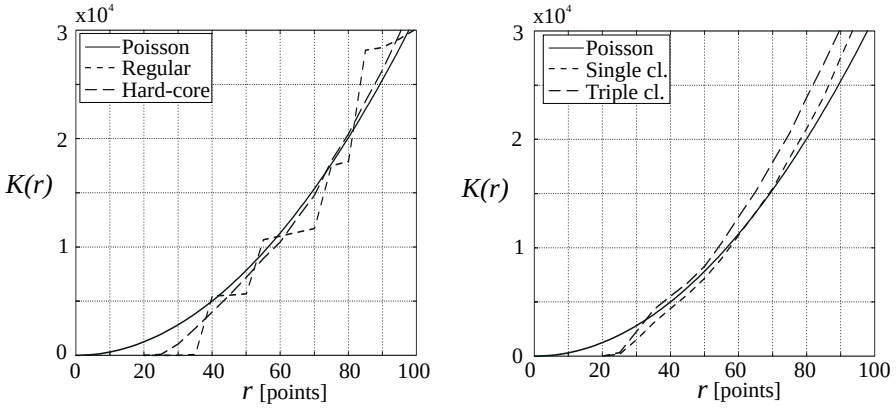

Figure 4.6: Second–order intensity function calculated for the four classes of distributions along with the Poisson distribution.

The second–order intensity function is only calculated for a radius range 0..100 points and the correction factor is included for the four distributions as no inclusions have been introduced at the boundary. In the radius range shown the hard–core distribution is very close to the Poisson distribution as the only difference between them is the finite size of inclusions in the hard–core model. The shape of the second–order intensity function for the regular distribution is formed as a "staircase" because only for deterministic distances of r in equation 4.3 additional inclusions are encountered. For the triple cluster distribution the second–order intensity function lies above the Poisson distribution because of the close dispersion of inclusions. Thus, the function $I_k(r)$ encounters relatively more inclusions for small distances than the other distributions. The second–order intensity function for the single cluster distribution lies between the triple cluster and the hard–core distribution as it both consists of a dense and a dilute dispersion of inclusions. To visualize the influence of the correction factor the second–order intensity function is calculated for the regular and hard–core distribution with and without the correction factor (fig. 4.7).

The curves in figure 4.7a, which lie above the Poisson distribution, correspond to the second–order intensity function with correction factor and those below without correction factor. With the correction factor the second–order intensity function goes to infinitly as the proportion of the circumference contained within A tends towards zero. Without the correction factor the function approaches a constant value as additional inclusions for large radial distance will not be encountered. In figure 4.7b, where a part of the curve has been enlarged, the second–order intensity functions with correction factor also lie above those without. In the enlarged figure the discrimination between different classes is much better. The slight declination of the "stairs" in the regular distribution is caused

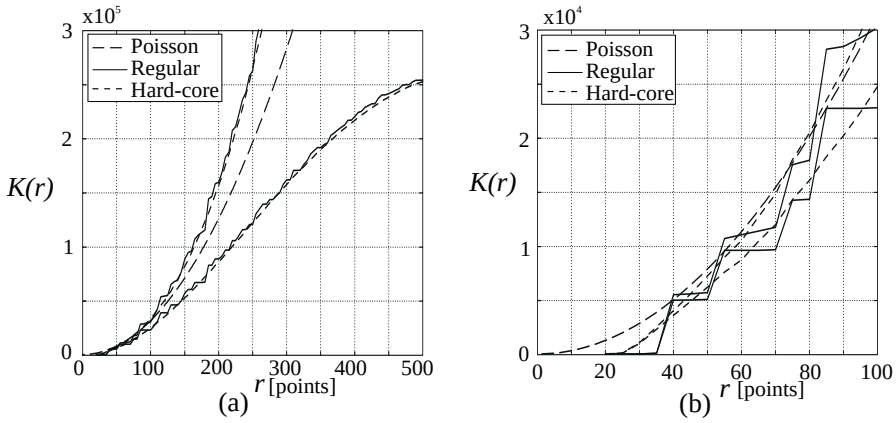

Figure 4.7: Second–order intensity function calculated for the regular and hard–core distributions; (a) for radius range 0..500 *points , (b) for radius range* 0..100 *points.*

by the correction factor and the curve without correction factor has straight horizontal lines.

Pair distribution function

Pertaining the information of the second-order intensity function, a related function is now introduced. This is the pair distribution function and it is related to the second–order intensity function as:

$$g(r) = \frac{1}{2\pi r}\frac{dK(r)}{dr} \tag{4.4}$$

The function provides information about the intensity of inter–distances so that local maxima indicate the most frequent distances and local minima the least frequent distances. The differentiation of the second–order intensity function must be performed numerically as it is a so-called *generalized function* which is not analytically differentiable. In the numerical differentiation the choice of step length is of vital importance for the result. Therefore, the pair distribution function serves as a measure of the tendency rather than an exact description. Using a step length of 5 points compared to the 512×512 points of the sample area the pair distribution function is calculated for the four classes of distributions and the Poisson distribution (fig. 4.8).

As the second–order intensity function for a Poisson distribution is known analytically as πr^2, the pair distribution function may also be found analytically and this leads to $g(r) = 1$. The pair distribution function for the hard–core distribution fluctuates closely around the Poisson distribution as it is a Poisson distribution with the exception that inclusions have a finite dimension. The regular distribution should consist of peaks representing the deterministic dispersion of points, but due to the numerical differentiation the peaks are broadened. Also because of the slight decline of the second–order intensity function for the regular distribution it has non–zero values between the peaks. The triple cluster distribution has higher intensity of inter–inclusion distances in the vicinity

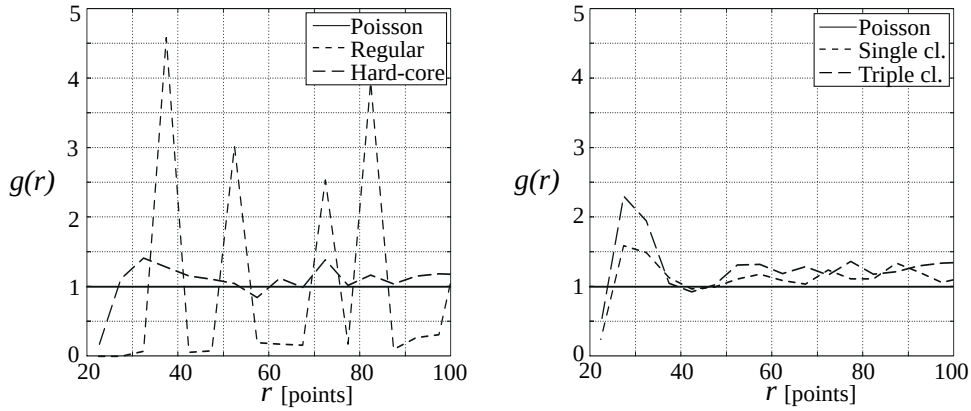

Figure 4.8: Pair distribution function calculated for the four classes of distributions along with the Poisson distribution.

of $r \approx 30$ points than the single cluster distribution and this is caused by high clustering of inclusions.

An interesting feature of the pair distribution function is that it can be used to detect the range of local geometrical disorder, i.e. for which values of r the second–order intensity function and the pair distribution function can be used to describe the disorder of the dispersion of inclusions. As an example approximately 3000 inclusions are generated using a hard–core and a cluster model. The latter model consists of 90 cluster areas (fig. 4.9).

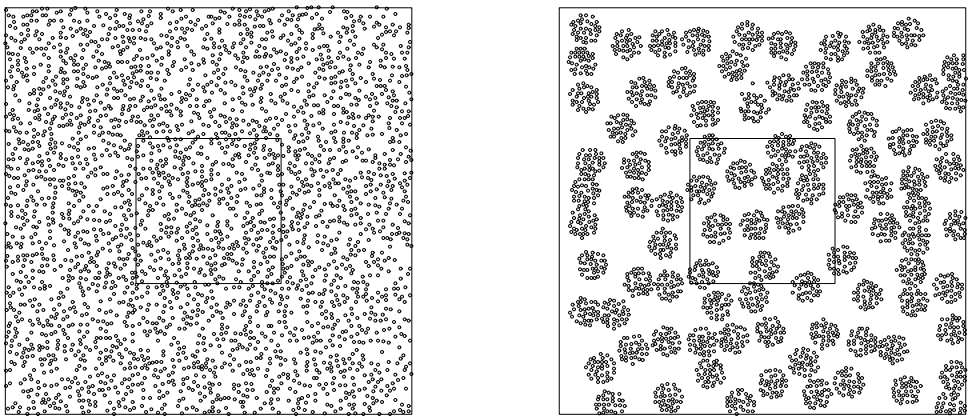

Figure 4.9: Distributions with approximately 3000 inclusions; (a) hard–core, (b) 90 clusters.

The second–order intensity function and the pair distribution function are only calculated in the enclosed sample area and by that the correction factor for edge effect is avoided. As stated before, this factor is not consistent for large distances, as the curve diverges from

the real path. The second–order intensity function is calculated for short–range distances 0..0.2 assuming the sample area to be a unit square, and as previously mentioned the patterns may be discriminated (fig. 4.10b).

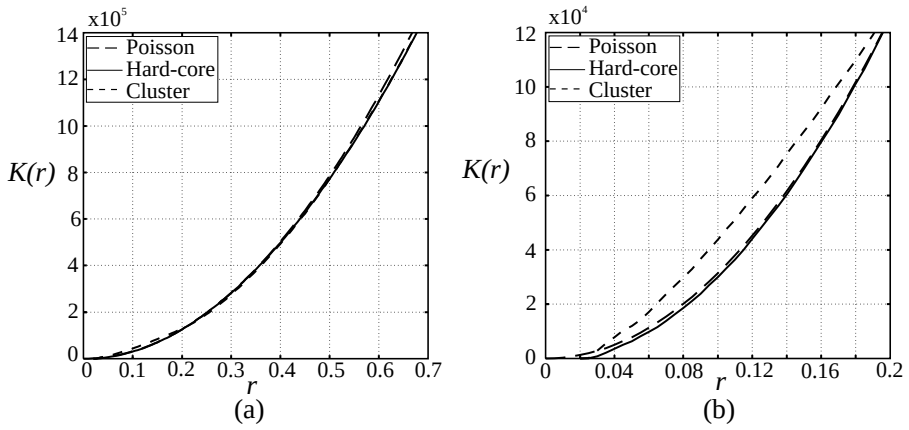

Figure 4.10: Second–order intensity function calculated for hard–core and cluster distributions; (a) long–range 0..0.7*, (b) short–range* 0..0.2*.*

The function is also calculated for long–range distances 0..0.7 and for this range the patterns cannot be discriminated (fig. 4.10a). This is caused by the fact that the second–order intensity function only takes into account the local disorder. To determine the range of locality the pair distribution function is calculated. The function is calculated for short–range distances and the two patterns exhibit different behaviour due to the various degree of clustering (fig. 4.11b).

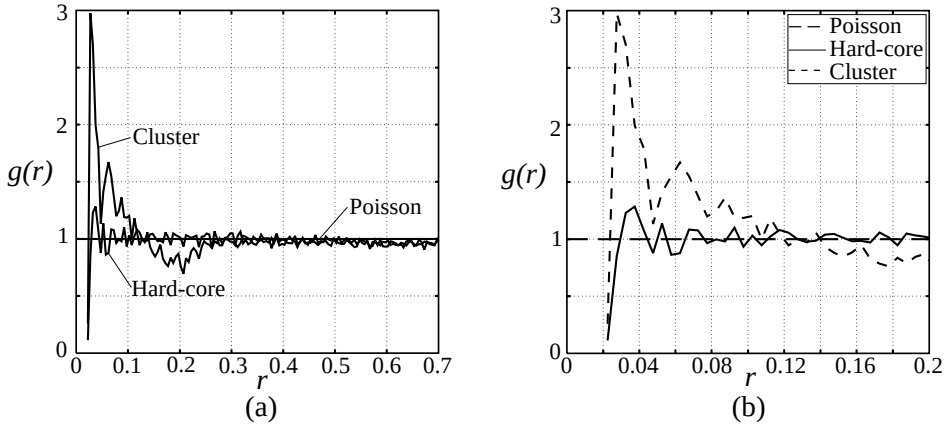

Figure 4.11: Pair distribution function calculated for hard–core and cluster distributions; (a) long–range 0..0.7*, (b) short–range* 0..0.2*.*

The local maximum at $r \approx 0.03$ for the cluster distribution corresponds to the aggregation

of inclusions inside the clusters. The local minimum at $r \approx 0.2$, which lies below the Poisson distribution, corresponds to relatively few large inter–inclusion distances. The function is also calculated for long–range distances and the range of locality may be determined on the basis of figure 4.11a where the patterns cannot be discriminated for $r > 0.25$. Thus for values of r larger than 0.25 the local disorder described by the second–order intensity function and pair distribution function will be smeared out.

Chapter

5

Local Stress Field Correlation with Fiber Distribution

The microstructure variability influences the response of a composite material and therefore it is reasonable to include the constitution of the microstructure in analyses of materials. Field quantities may be determined and correlated with the geometrical aspects of the microstructure. Stress level distribution in the fibers and local stress field around the fibers are field quantities which are of interest. Correlation between the distribution of fibers and field quantities can indicate the sensitivity towards crack nucleation.

The problem is very complex because it is possible to form an infinite number of different types of fiber distributions and therefore it is necessary to select only a few types of distributions in order to decompose the problem and reduce the number of analyses. Distributions must represent particular types of microstructures as well as cover a wide range of them. Also the distributions are sampled from a small area out of a whole microstructure and therefore it is important to investigate the influence of various boundary conditions.

The amount of interaction between the individual fibers varies as a consequence of non–regular arrangements of fibers. Corresponding to the method presented in section 1.2 the stress field inside the fibers is assumed constant and the various interaction results in different stress levels in the fibers. Contrary to the varying stress levels in non–regular arrangements of fibers the regular arrangements of fibers result in equal stress levels in the fibers as the amount of interaction on each fiber is the same. The fiber arrangement also affects the local stress field in the matrix material as fiber stresses are responsible for the interaction. Therefore, it is an important parameter in the prediction of response of a composite material.

It is reasonable to assume that cracks in a stressed material may be created in the vicinity of the fibers as they introduce a large variation of the local stress field. Especially the maximum values of the local stress field around the fibers may create both interface and matrix cracking. Thus, it is interesting to calculate maxima of the local stress field around each fiber and correlate this information with the geometrical properties of the microstructure. Then it is possible to indicate a particular fiber arrangement's tendency

to the creation of cracks. A preliminary investigation of this subject has been carried out in Pyrz [20] where among other things the influence of fiber arrangements has been established using the *marked correlation function*. The function is able to detect the correlation between the microstructure and quantities attached to the fibers.

In section 5.1 representative fiber distributions are chosen and various boundary conditions are selected. The resulting stress fields in the fibers are presented in section 5.2 and a correlation between geometrical parameters of the fiber distribution and the stress field distribution is discussed. In section 5.3 the local stress field around the fibers is determined and various arrangements of fibers seem to be more or less susceptible to crack initiation. Finally in section 5.4 three real microstructures are analysed.

5.1 Selection of Fiber Distributions

The already mentioned four distribution types cover the normally assumed regular distribution, the almost total random distribution and various degrees of clustering, so besides representing a few characteristic distributions they also cover the most common microstructures. A more thorough description of the distribution types is given in section 4.2. Both the effects of changing the boundary conditions and the volume fraction are considered in the selection of fiber distributions.

The fibers are distributed within a unit cell as in figure 4.3 which consists of a boundary area and a sample area exposed to unidirectional loading. The total area is 1024×1024 points, the sample area is 512×512 points and the fibers are distributed with radius equal to 10 points. Variation of the boundary conditions and the volume fraction for the different types of fiber distributions include the generation of four models (Tab. 5.1).

Table 5.1: Distribution models for the different types of fiber distributions.

	Sample area		Boundary area	
Model	Volume fraction	No. fibers	Volume fraction	No. fibers
I	0.12	100	0.12	300
II	0.24	200	0.24	600
III	0.24	200	0.12	300
IV	0.24	200	0.24	600

The individual distributions are in the following referred to by the name of distribution and model number, e.g. single cluster(III) corresponds to single cluster distribution generated using the concept in model III. The fiber distributions with high volume fraction in the sample area (model II, III and IV) are similar to the distributions shown in figure 4.4. The fiber distributions with low volume fraction in the sample area (model I) are shown in figure 5.1 where also the fiber distribution in the boundary area has been applied.

For the regular distribution type with low volume fraction the spacing between fibers (centre to centre distance) in both horizontal and vertical directions is 51 points and for high volume fraction the spacing is 36 points. For low volume fraction the single cluster distribution type has a circular cluster area with a radius of 135 points and contains 60 of the 100 fibers. For high volume fraction the radius is 170 points and contains 100 of the

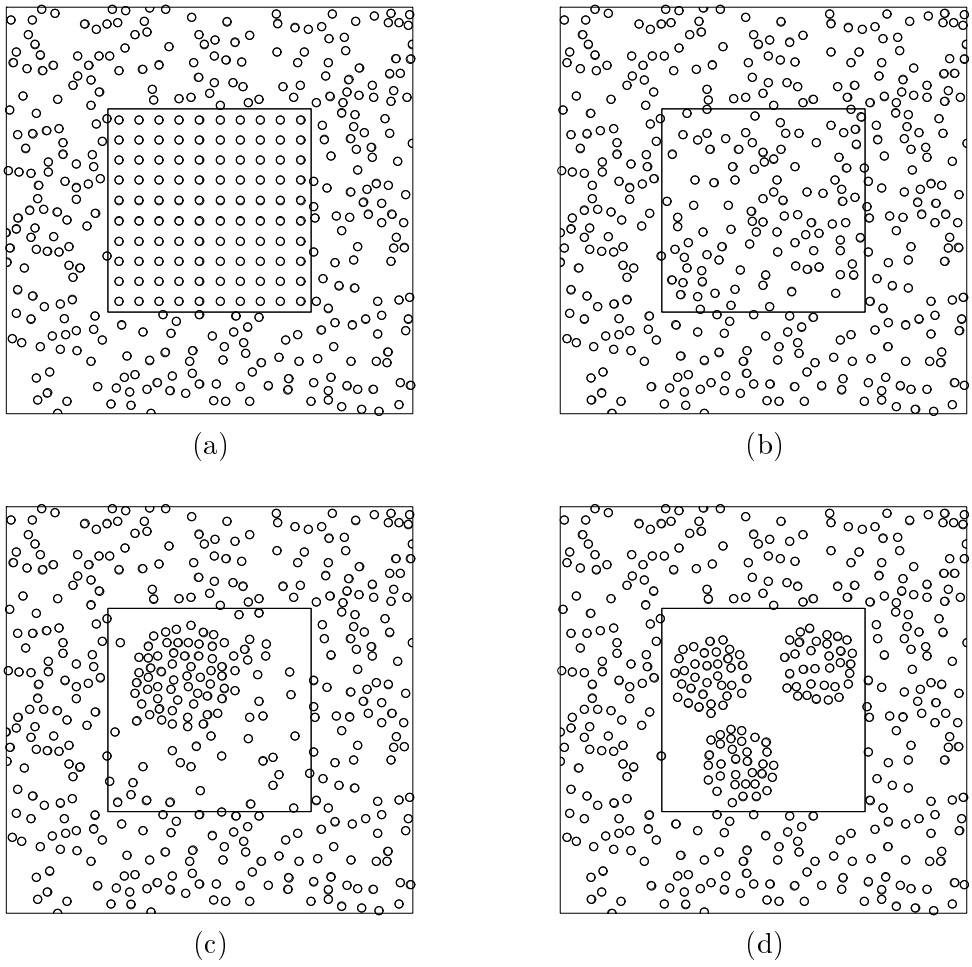

Figure 5.1: The four types of fiber distributions with low volume fraction in the sample area and the applied boundary conditions; (a) regular(I), (b) hard–core(I), (c) single cluster(I), (d) triple cluster(I).

200 fibers. The triple cluster distribution type for low volume fraction is made of three equally sized circular cluster areas with radius 100 points containing each a third of the fibers. For high volume fraction the three cluster areas are of elliptic shape where two of them have semi–minor and semi–major axes equal to 110 and 145 points respectively, containing 60 fibers each. The third cluster has semi–minor and semi–major axis equal to 95 and 225 points respectively, containing 80 fibers. For the hard–core distributions with high and low volume fraction the fibers are generated with their centres within the sample area.

Each of the distribution types is supplemented with boundary conditions and in order to establish a unified concept the fiber distributions generated using the selected model have the same type of boundary condition. The fiber distributions generated using model I and III are exposed to the same type of boundary conditions and they are given in form of a low volume fraction hard–core distribution (fig. 5.2a). Correspondingly, the fiber distributions generated using model II are exposed to a high volume fraction hard–core distribution (fig. 5.2b).

The boundary conditions are generated so that the fibers in the boundary area and sample area do not intersect. The fiber distributions generated with model IV have all periodic boundary conditions. In this case the boundary area depends on the actual distribution in the sample area and the microstructure is characterized as a repetitious unit cell (fig. 5.3).

Two of the most important parameters describing the geometry of the microstructure are the nearest neighbour distance and the nearest neighbour orientation. As shown in section 4.2 the nearest neighbour distance is able to detect the degree of clustering through the statistical moments and therefore serves as a useful parameter. The effect of the nearest neighbour orientation can be evaluated through the stress field distribution in the fibers. Of course the stress field is affected by the inter–distances but also by inter–orientations as seen from figure 4.1 where different angles between fibers lead to various stress fields for equal inter–distances. The calculations of the nearest neighbour orientation are performed so that the direction perpendicular to the loading direction corresponds to 0° and the direction parallel to the loading direction corresponds to 90°. Furthermore, the angles are sampled in the following way:

$$\theta = \begin{cases} \theta & \text{if} \quad 0 \leq \theta < 90 \\ 180 - \theta & \text{if} \quad 90 \leq \theta < 180 \\ \theta - 180 & \text{if} \quad 180 \leq \theta < 270 \\ 360 - \theta & \text{if} \quad 270 \leq \theta < 360 \end{cases} \tag{5.1}$$

The mean value and the variance of the nearest neighbour distances and orientations are for all the distributions sampled within the sample area but the boundary area may interfere at the edge of the sample area (Tab. 5.2).

The mean values and variances of both nearest neighbour distances and orientations differ for model II, III and IV because of various boundary conditions although the sample areas are identical. It may also be noted that the mean value and variance of distances for the triple cluster distributions are relatively lower than for the others due to the high degree of clustering. The mean values and variances of distance are higher for model I than for the other models due to a lower volume fraction, which results in a more sparsely distributions of fibers. The inter–orientations do not provide any information regarding the degree of clustering but as seen later it will be very informative for stress field distribution in the fibers. The mean values of nearest neighbour orientation are not calculated for the regular distributions (model I, II and III) as these are deterministic and are only influenced by the various boundary conditions. For the perfectly regular distribution (model IV) the mean value of orientation is exactly equal to both 0° and 90° due to the equal spacing between fibers.

For all types of distributions and models the same material parameters and remote loading conditions are used. Thus the ratio between Young's moduli for the fiber and matrix material is $E_a/E_m = 23$, Poisson's ratio for the fiber material $\nu_a = 0.30$ and Poisson's ratio for the matrix material $\nu_m = 0.35$. The material parameters correspond to the glass/epoxy composite. The remote loading is equal to unity and plane strain is assumed in the stress analysis.

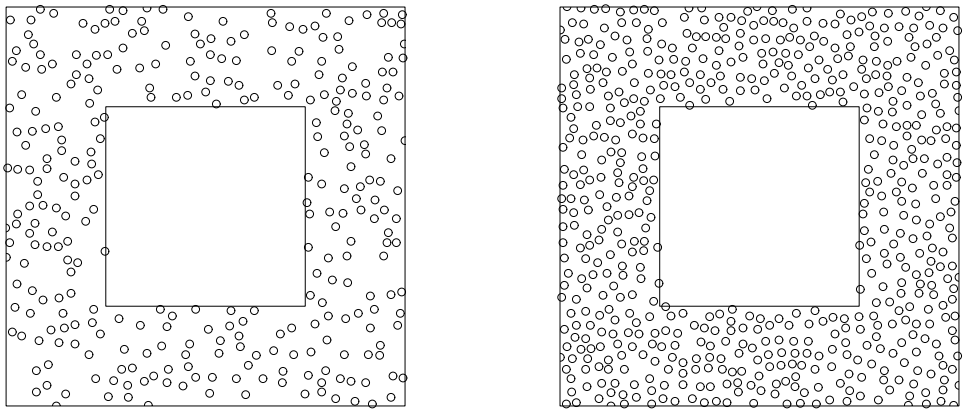

(a) (b)

Figure 5.2: Boundary areas generated with hard–core distribution; (a) low volume fraction (model I and III), (b) high volume fraction (model II).

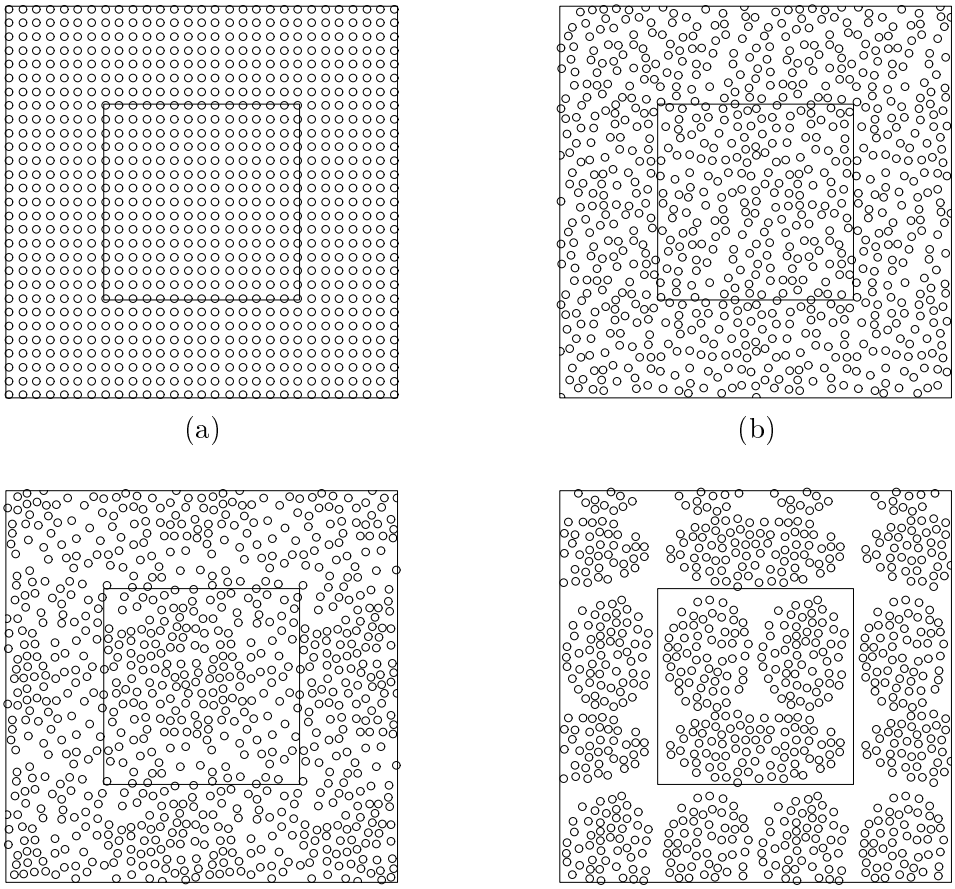

(a) (b)

(c) (d)

Figure 5.3: Fiber distributions with periodic boundary conditions; (a) regular(IV), (b) hard–core(IV), (c) single cluster(IV), (d) triple cluster(IV).

Table 5.2: Mean value and variance of nearest neighbour distances and orientations for all distributions and models, distances are measured in points and orientations in degrees.

	Nearest neighbour distance		Nearest neighbour orientation	
Distribution type	Mean	Variance	Mean	Variance
regular(I)	48.8	28.1	-	-
hard–core(I)	35.2	73.7	50.2	831
single cluster(I)	32.4	95.8	49.3	918
triple cluster(I)	27.0	8.3	49.7	1107
regular(II)	35.5	2.6	-	-
hard–core(II)	29.3	12.6	43.3	894
single cluster(II)	28.5	18.7	41.2	1020
triple cluster(II)	26.8	6.0	47.2	1091
regular(III)	35.7	2.0	-	-
hard–core(III)	29.0	16.0	47.4	1012
single cluster(III)	29.1	20.3	43.7	1020
triple cluster(III)	26.9	6.0	46.4	1093
regular(IV)	36.0	-	0/90	-
hard–core(IV)	28.6	13.5	46.5	986
single cluster(IV)	28.8	16.5	43.4	1018
triple cluster(IV)	26.9	6.1	46.4	1111

5.2 Fiber Stress Distribution

The stress field inside the fibers depends on the local interaction between fibers and the method presented in section 1.2 accounts for this interaction. The interaction either increases or decreases the stress field inside the fibers relative to the solution for one fiber.

The stress field inside a fiber for varying inter–distances and inter–orientations between two fibers is shown in figure 4.1. The stress level for the inter–orientation angle $\theta = 0^\circ$ is approximately equal to the stress level in the case of only one fiber. Thus, the interaction between two fibers aligned horizontally is relatively small. For $\theta = 30^\circ$ the stress decreases and for $\theta = 60, 90^\circ$ it increases as compared to the single fiber solution. Information about the local interaction is provided by the figure but the possibility of arranging fibers is numerous and therefore it is necessary to consider other configurations. This is done by calculating the stress field for the various types of distribution. The stress field inside the fibers is represented by the von Mises stress and in figure 5.4 the stress field is shown for distributions generated using model II.

It is obvious that the arrangement of fibers affects the stress field inside the fibers and consequently it also affects the local stress field in the matrix. The regular distribution of fibers shows only a small variation of the stress field as the fibers all are exposed to the same amount of interaction. Only at the edge of the sample area a disturbance is observed which is caused by the hard–core fiber distribution in the boundary area.

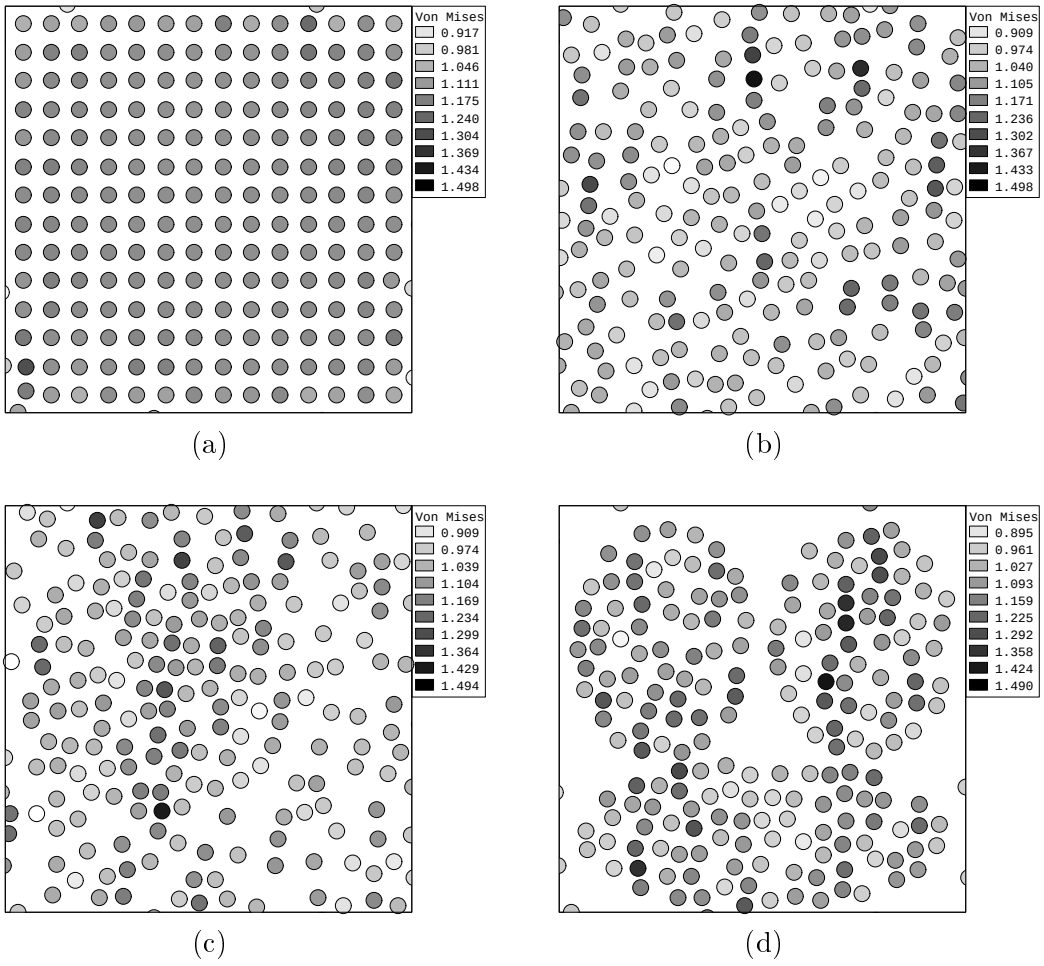

Figure 5.4: Von Mises stress plot for the distribution classes, normalized with σ_∞; (a) regular(II), (b) hard–core(II), (c) single cluster(II), (d) triple cluster(II).

The other three distributions all show varying stress fields in the fibers and for excessive clustering of fibers a large variation of the stress level is detected. This may also be shown by calculating the cumulative distribution function and the probability density function of the stress field distribution inside the fibers (fig. 5.5).

The normalized cumulative and probability density functions are determined by a curve–fitting procedure similar to the procedure described in section 4.2. Only stress field data within the sample area are included in the calculations. The probability density function for the regular distribution exhibits a peak–like shape corresponding to identical interacting stresses. For the other three distributions the shape becomes more broaden as the fibers become more clustered. Applying the probability density function for both model I and II the mean value and variance of the von Mises stress distribution may be calculated according to the statistical moments listed in section 4.2 (Tab. 5.3).

For the regular distribution the mean value of the von Mises stress increases considerably when increasing the volume fraction. Looking into the problem, the nearest neighbour orientation is located at 0° and 90°. From figure 4.1 it is observed that if the fibers are

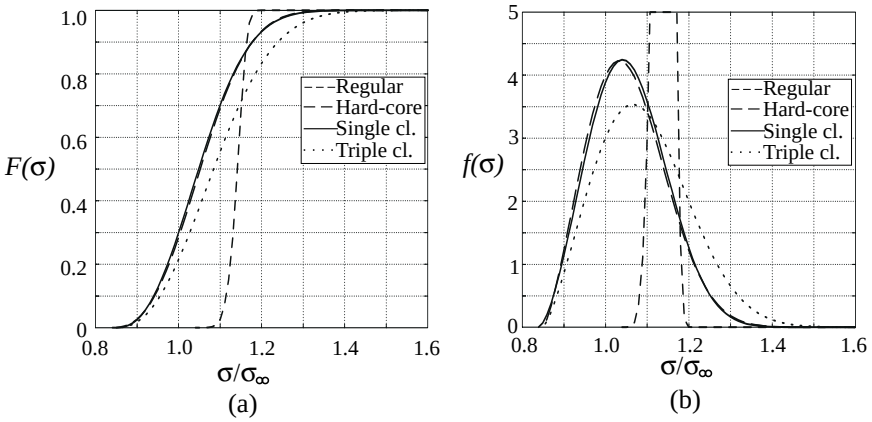

Figure 5.5: Distribution of the von Mises stress calculated in the sample area of model II; (a) normalized cumulative distribution, (b) probability density.

Table 5.3: Mean value and variance of the von Mises stress inside the fibers within the sample area for the four distributions generated with model I and II, normalized with σ_∞.

Parameter	Regular	Hard–core	Single Cluster	Triple Cluster
Mean(I)	1.074	1.044	1.053	1.097
Variance(I)	0.0005	0.0097	0.0056	0.0111
Mean(II)	1.139	1.054	1.057	1.092
Variance(II)	0.0008	0.0083	0.0081	0.0119
Normalized von Mises stress for the single fiber: 1.035				

aligned horizontally the interaction is moderate but if the fibers are aligned vertically the interaction is very influential. So for higher volume fraction in the regular distribution where the inter–distances of the vertically aligned fibers become smaller the stress level increases. Generally for the non–regular distributions the mean value of the von Mises stress seems to increase when the distributions become more clustered (measured by mean values of the nearest neighbour distances) both with respect to the type of distribution and the volume fraction. An exception is the triple cluster distribution where the mean value decreases for a higher volume fraction. The reason for this behaviour is that not only the mean nearest neighbour distance affects the stress field distribution but also the mean nearest neighbour orientation. Again the combined effect can be visualized from figure 4.1 where some angles lead to an increase and other angles lead to a decrease of the stress field inside the fibers. For the range of mean nearest neighbour orientations listed in table 5.2, which is approximately $40°$ –$50°$, the effect is enhanced for increasing angles or reduced for decreasing angles. When lowering the angle the stress level decreases and vice versa. From the nearest neighbour distances a lowering of the mean value leads to an increase of the stress level. Combining the information of how nearest neighbour distance and orientation affect the stress level, a rough estimate of the influence of these

parameters may be given by considering the correlation between the mean value of the von Mises stress and the ratio between the mean value of the nearest neighbour distance and the nearest neighbour orientation (fig. 5.6).

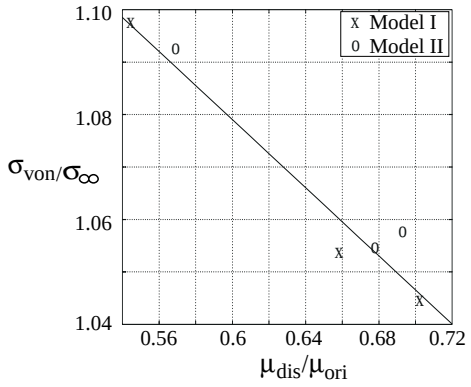

Figure 5.6: Correlation between the mean value of the von Mises stress and the ratio between the mean value of the nearest neighbour distance and the nearest neighbour orientation.

The correlation only represents a tendency and several simulations need to be performed in order to obtain consistent results. In the particular case of the triple cluster distribution the mean nearest neighbour distance is almost equal for both low and high volume fraction but the mean nearest neighbour orientation is lower for the high volume fraction. This results in a smaller ratio between mean nearest neighbour distance and orientation for the high volume fraction than for the low volume fraction and thus also a small value of the mean stress field.

It must be concluded that the stress field distribution is very much affected by the nearest neighbour distance through the volume fraction and the degree of clustering but an important parameter, which must also be taken into consideration, is the nearest neighbour orientation.

5.3 Local Stress Field Around the Fibers

The non–regularity of the microstructure leads to a varying stress field distribution inside the fibers. This varying stress field distribution adds even more variation to the stress field in the matrix and some areas of the matrix may be exposed to higher stress levels than other areas. These areas with higher stress levels are more sensitive towards the creation of cracks, and thus the non–regularity of fiber distributions affects the damage evolution.

It is informative to calculate maxima of the local stresses around each fiber as the stresses are mainly responsible for the creation of radial and tangential cracks. Thus calculating the stress field in a polar coordinate system with origin at the centre point of each fiber, the radial stress component σ_r is related to the tangential or interface cracks and the tangential stress component σ_θ is related to radial or matrix cracks (fig. 5.7).

The stress field is calculated in a small annular layer around each fiber and the sampling consists of a registration of maximum values of the tangential and radial stress components as well as the angles, at which these maxima are determined. The maximum values of the tangential stress component for the four types of distributions generated using model IV are shown in figure 5.8.

The dots represent the centre of the fibers, the length of the segments indicates the magnitude of the maximum value and the orientation of the segments shows the angle, at which the maximum values are determined. Obviously the variation of maximum values as well as the angles at which they occur are highly dependent on the distribution of fibers. Thus some arrangements of fibers are more sensitive towards the creation of cracks than others. In the regular distribution the maximum values only appear at two distinct locations whereas the other distributions exhibit a larger variation. This is a result of the interaction where the fibers in the regular distribution with periodic boundary conditions are exposed to the same amount of interaction and consequently the local stress field around the fibers only varies around the individual fiber. The corresponding maximum values of the radial stress component are shown in figure 5.9.

Also in this case the angles in regular distribution appear in two distinct angles and a larger variation exists for other distributions. However, the variation of the angles is not as pronounced as for the maximum tangential stress component and as seen later in this section this is caused by larger variation of the local stress field of the radial stress component.

The cumulative distribution function of maximum values is approximated by the function in equation 4.1 and the corresponding probability density function is found by differentiation of cumulative function. The probability density function of both the tangential and radial stress component for the four distributions generated by model II is shown in figure 5.10.

The maximum values are only determined for fibers within the sample area but are of course exposed to interaction from the fibers in the boundary area. The regular distribution forms a probability density function consisting of a peak–like value whereas the other distributions have more broaden shapes. The shape becomes even more broaden for increased clustering of fibers due to the large variation of the maximum values. The mean value of the maximum tangential stress component for the regular distribution is lower than for the other distributions. Conversely, the mean value of the radial stress component is higher than the other distributions. This provides some information as to which type of distribution is most sensitive to the nucleation of cracks. The mean value and variance of the maximum values of both tangential and radial stresses are shown in table 5.4.

The mean values of the tangential stress component for the all regular distributions are considerably lower than for the other distributions. For the other distributions the triple cluster distributions have the highest mean value. The mean value of radial stress component for the triple cluster is also higher than for the other distributions. However, the regular distributions exhibit higher susceptible to interface cracking than the hardcore and single cluster distributions for model II, III and IV (high volume fraction). Thus it may be concluded that matrix cracks are most likely to occur in non–regular distributions and interface cracks are most likely to occur in the high–clustered distributions followed by the regular distribution. The boundary conditions have some influence on the determination of maximum values, as the analysis of model II, III and IV reveals.

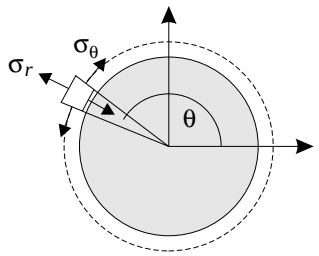

Figure 5.7: Tangential and radial stress components around the fibers.

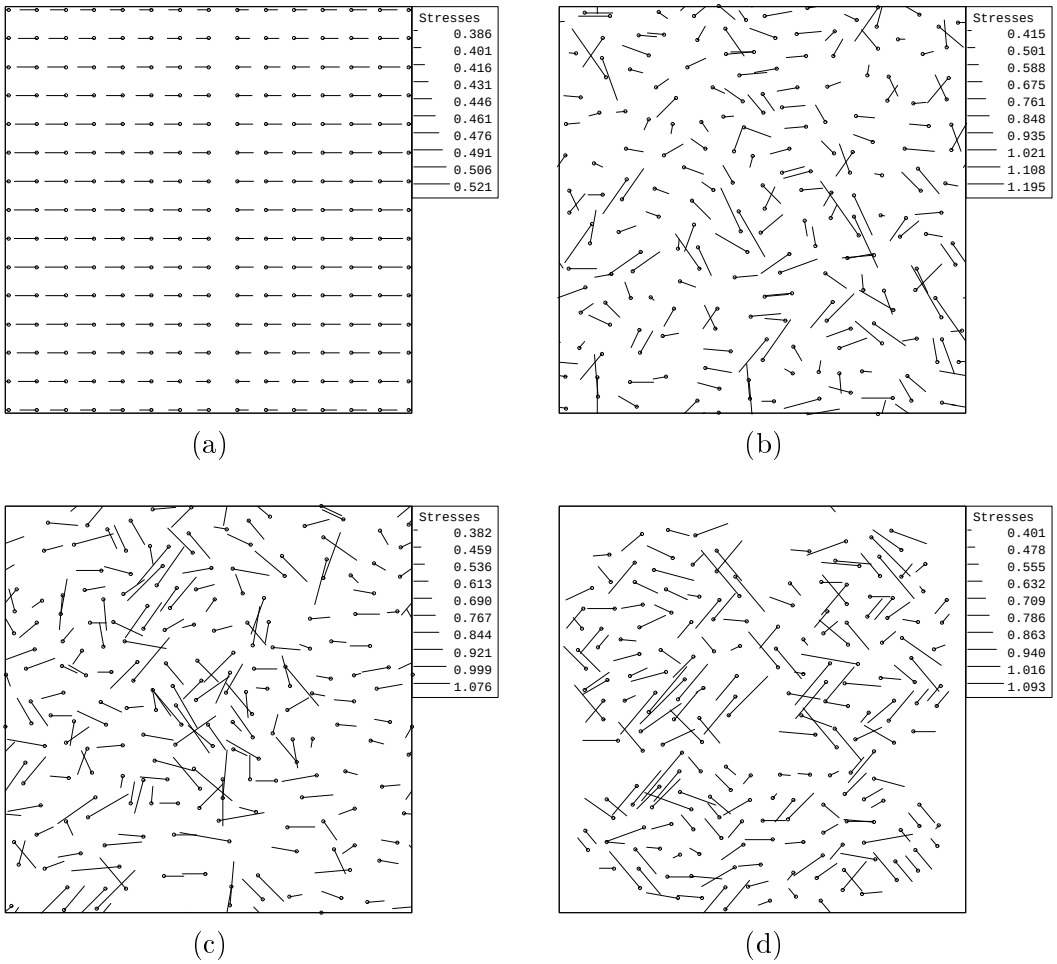

Figure 5.8: Distribution of the maximum tangential stress component for the four distributions, normalized with σ_∞; (a) regular(IV), (b) hard–core(IV), (c) single cluster(IV), (d) triple cluster(IV).

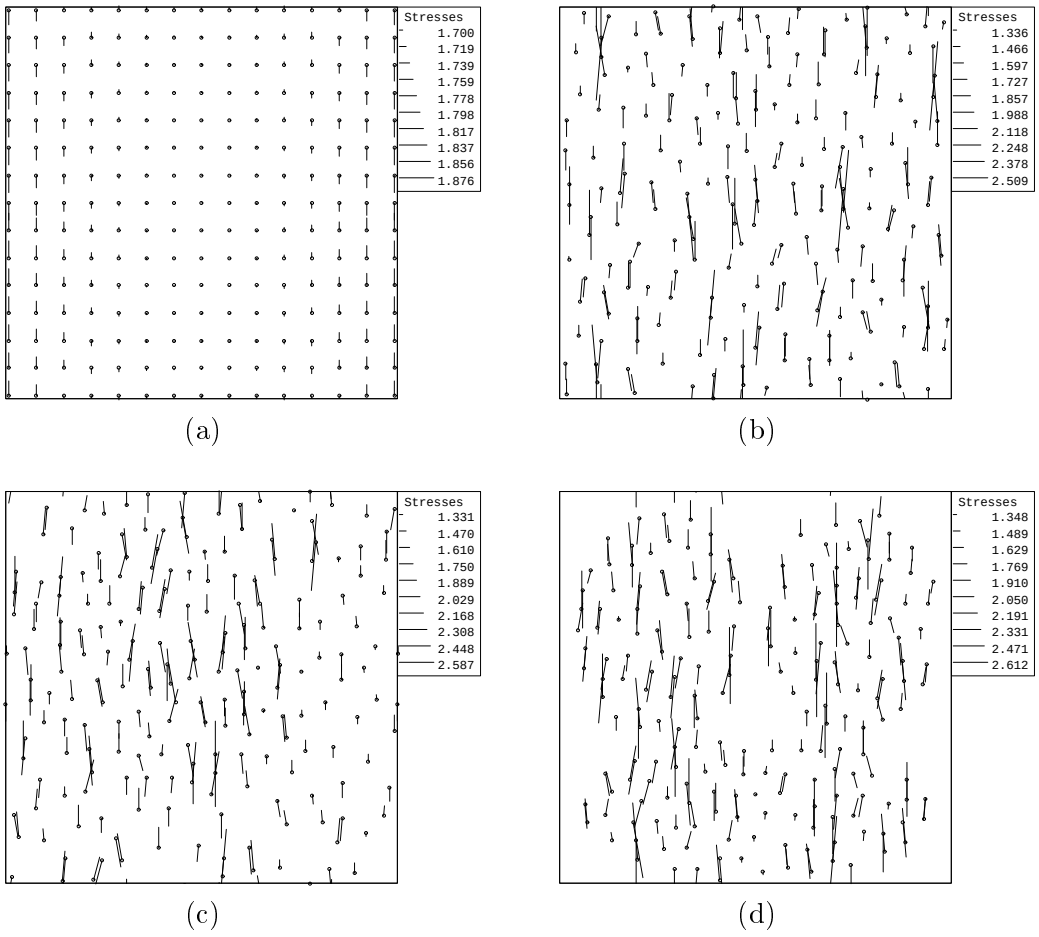

Figure 5.9: Distribution of the maximum radial stress component for the four distributions, normalized with σ_∞; (a) regular(IV), (b) hard–core(IV), (c) single cluster(IV), (d) triple cluster(IV).

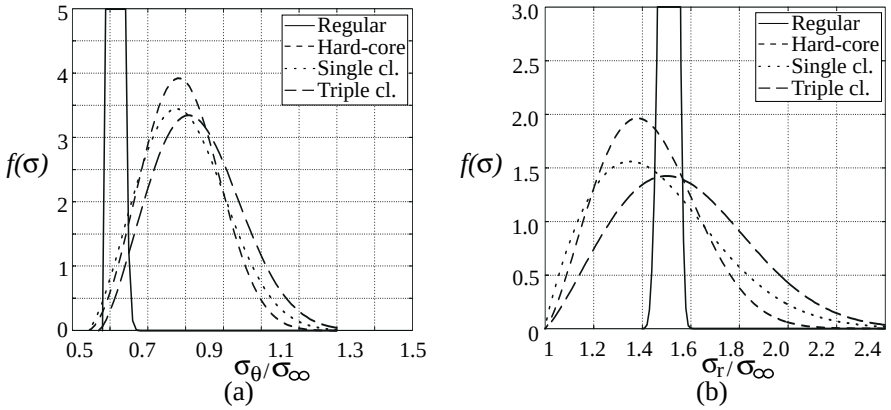

Figure 5.10: Probability density functions of the four distributions generated with model II; (a) tangential stress component, (b) radial stress component.

Table 5.4: Mean value and variance of maximum values calculated around fibers within the sample area for all distributions, normalized with σ_∞.

	Tangential stress		Radial stress	
Distribution type	Mean	Variance	Mean	Variance
regular(I)	0.47	0.0003	1.58	0.0017
hard–core(I)	0.57	0.0101	1.60	0.0523
single cluster(I)	0.58	0.0131	1.65	0.0502
triple cluster(I)	0.61	0.0162	1.73	0.0684
regular(II)	0.43	0.0016	1.72	0.0015
hard–core(II)	0.59	0.0098	1.62	0.0467
single cluster(II)	0.60	0.0136	1.64	0.0552
triple cluster(II)	0.64	0.0138	1.74	0.0676
regular(III)	0.42	0.0010	1.73	0.0017
hard–core(III)	0.62	0.0205	1.69	0.0764
single cluster(III)	0.59	0.0114	1.65	0.0481
triple cluster(III)	0.63	0.0142	1.74	0.0675
regular(IV)	0.41	0.0001	1.70	0.0003
hard–core(IV)	0.63	0.0182	1.66	0.0698
single cluster(IV)	0.61	0.0143	1.64	0.0503
triple cluster(IV)	0.66	0.0202	1.75	0.0762

The angles at which the maximum stress components occur are also influenced by the non–regularity of the microstructure. Figure 5.11 shows histograms for angles where maximum tangential stress component occurs. The histograms are presented for regular and triple cluster distributions generated by model IV.

For the regular distribution the angles are concentrated around two distinct angles $\theta = 0^\circ, 180^\circ$ whereas the angles for the triple cluster distribution have much larger variation. The corresponding angles for the radial stress component are shown in figure 5.12. The angles in the regular distribution are concentrated around two distinct angles $\theta = 90^\circ, 270^\circ$ and this is also the case for the triple cluster distribution with a slightly larger variation. The reason why the maximum values are concentrated around distinct angles can be visualized by considering the local stress field around one fiber where the interaction from the other fibers is omitted (fig. 5.13).

Maximum values occur at two distinct angles leading to eventual nucleation of cracks in these positions. The variation of the tangential stress component is not large and it may easily diverge from the distinct angles due to interaction. On the contrary, a strong interaction is needed to make the maximum radial stress component diverge from the distinct angles. This is also seen by comparing the angles from the triple cluster distribution where a large variation of angles exists for the maximum tangential stress. In order to characterize this behaviour, the average deviation of angles is calculated as:

$$\theta_{avgd} = \frac{1}{N} \sum_{i=1}^{N} |(\theta_i - \theta_{one})| \tag{5.2}$$

where θ_i is the angle at which maximum values occur, θ_{one} are the corresponding values

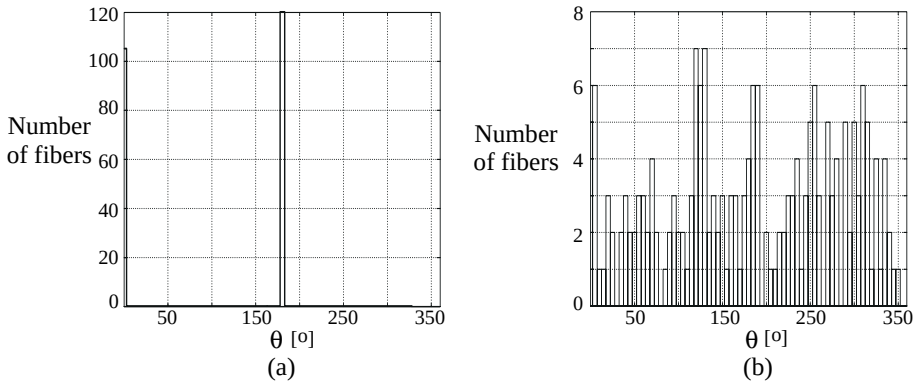

Figure 5.11: Distribution of registered angles of maximum tangential stress; (a) regular(IV), (b) triple cluster(IV).

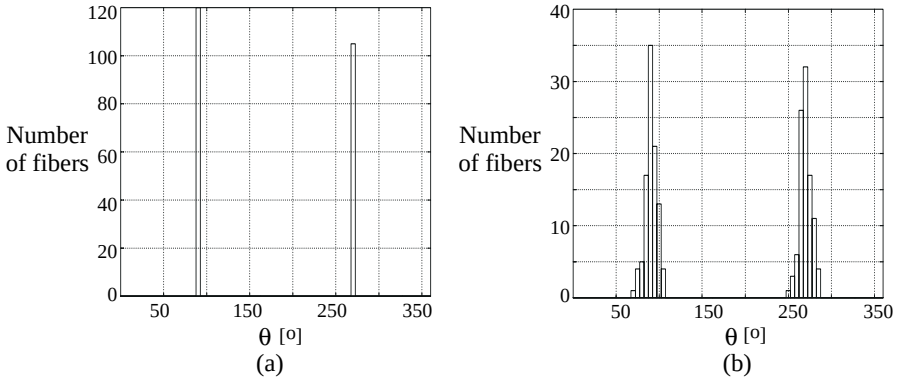

Figure 5.12: Distribution of registered angles of maximum radial stress; (a) regular(IV), (b) triple cluster(IV).

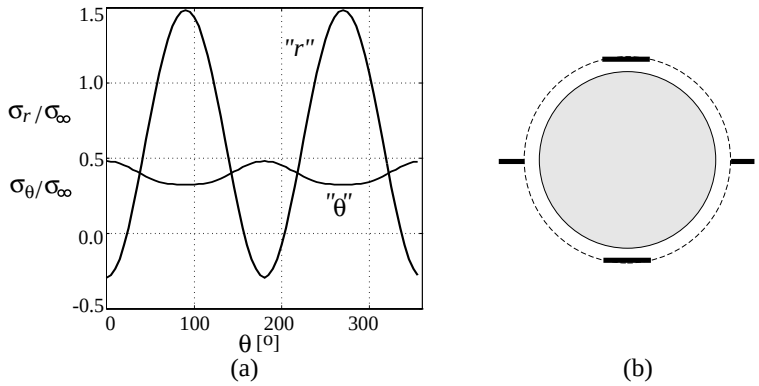

Figure 5.13: (a) Normalized tangential and radial stress components for the single fiber configuration, (b) possible locations of interface and matrix cracks.

for one fiber and N is the total number of fibers. The average deviation angles of the tangential and radial stress components for the four distributions are listed in table 5.5.

Table 5.5: Average deviation of angles of the maximum tangential and radial stress components, angles in degrees.

Distribution	Model I	Model II	Model III	Model IV
Tangential:				
regular	2.1	4.9	5.3	0.00
hard–core	21.6	31.7	36.5	36.6
single cluster	28.0	36.3	33.6	36.9
triple cluster	45.0	43.6	42.7	48.9
Radial:				
regular	0.10	0.08	0.05	0.00
hard–core	2.35	4.18	3.58	3.75
single cluster	3.30	4.25	4.13	4.16
triple cluster	3.80	5.42	5.28	5.10

The average deviation of angles is affected by the type of distribution and the triple cluster distribution is seen to be the most influencial. Also the volume fraction affects average deviation angles and it diverges more from the distinct values for fiber distributions with high volume fraction than for fiber distributions with low volume fraction. It may be concluded that the more clustered a microstructure becomes, the higher the average deviation angle becomes. The damage evolution in a composite material is then very much dependent on the arrangement of fibers both with respect to when (variation of maximum values) and where (variation of angles) the cracks nucleate.

5.4 Analysis of Real Microstructures

Three microstructures sampled from real materials are analysed in the following. The microstructures are extracted from three specimens made of the same material (Glass/-Epoxy) but exposed to various manufacturing processes. Thus according to Pyrz [21] specimen 1 is made with no pressure and specimen 2 and 3 are made with half and full pressure, respectively. The material properties correspond to those used in simulated microstructures. The real microstructures are divided into a sample area and a boundary area (fig. 5.14).

Radius of fibers is 7 points, the sample area is 512×512 points and the total area is 768×768 points. The number of fibers and the volume fraction in the sample area and boundary area are shown in table 5.6.

The volume fraction of fibers grows when the applied pressure is increased and the distribution of fibers changes. In order to discriminate the microstructures the second–order intensity function is calculated for the three distributions. The curve, which lies above the other curves corresponds to the microstructure from specimen 1, which is the

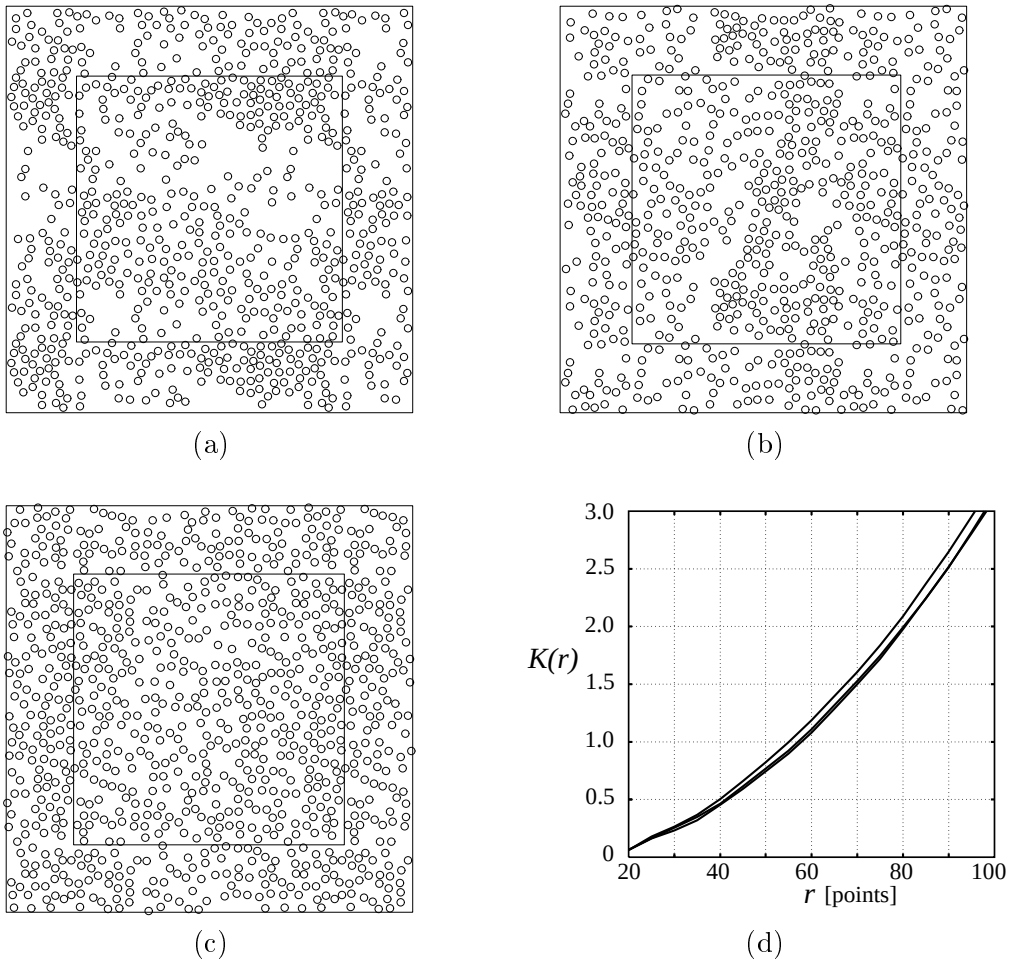

Figure 5.14: The three real microstructures; (a) no pressure, (b) half pressure, (c) full pressure, (d) second–order intensity functions.

Table 5.6: Volume fraction and number of fibers for the microstructures of three real materials.

	Sample area		Boundary area	
Specimen	Volume fraction	No. fibers	Volume fraction	No. fibers
1	0.20	333	0.21	454
2	0.21	351	0.19	408
3	0.24	415	0.25	533

most aggregated (fig. 5.14d). For specimen 2 and 3 the function is not able to make any considerable distinction. The microstructures from specimen 1 and 2 seem to consist of matrix rich areas and areas with a dense distribution of fibers. The microstructure from specimen 3 is more or less similar to the hard–core distribution with a slight tendency to clustering. The nearest neighbour distances and orientations were calculated for the

real microstructures and the results are shown in table 5.7.

Table 5.7: Mean value and variance of nearest neighbour distances and orientations for the real microstructures, distances are measured in points and orientations in degrees.

	Nearest neighbour distance		Nearest neighbour orientation	
Specimen	Mean	Variance	Mean	Variance
1	20.5	12.5	48.6	683
2	20.1	7.6	38.8	693
3	19.4	5.4	41.2	705

The mean value of the nearest neighbour distances for the three distributions is comparable although the volume fraction is different and both specimen 1 and 2 are more clustered than specimen 3. The more dense distribution of fibers in specimen 3 is indicated by a lower variance. As for the simulated microstructures the stress field distribution in the fibers as well as the maximum tangential and radial stress components and the corresponding angles were calculated (Tab. 5.8).

Table 5.8: Different parameters calculated for the three real microstructures, stresses are normalized with σ_∞ and angles are in degrees.

Parameter	Specimen 1	Specimen 2	Specimen 3
Fiber stress:			
mean	1.030	1.033	1.025
variance	0.010	0.012	0.011
Max. tangential stress:			
mean	0.64	0.62	0.659
variance	0.021	0.022	0.026
Max. radial stress:			
mean	1.61	1.59	1.59
variance	0.050	0.048	0.053
Avg. dev. angle:			
tangential	26.1	25.2	29.0
radial	4.59	3.86	4.16

For the microstructure with high volume fraction the mean value of the stress field distribution is smaller than the other two. In the same manner as the results for simulated microstructures are found, the correlation between nearest neighbour distances and orientations and stress field distribution may be performed. Comparing the results from material 1 and 3 it is obvious that a correlation exists. They have approximately the same mean value of distances and material 3 has smaller mean value of orientations resulting in a lower mean stress level. This is not so obvious when comparing material 2

with the other materials. Although the simple calculation of nearest neighbour distances and orientations does not provide a full quantification of these real microstructures it still serves as an informative parameter. The calculation of maximum tangential and radial stresses shows no particular dissimilarity between the three real materials.

Chapter

6

Fiber Distributions' Influence on Crack Parameters

Fibrous composite materials start to deteriorate in form of microcracks in the matrix material, debonding between the matrix material and the fibers etc. when load is applied. The geometry of the microstructure is responsible for the formation of failures because the fracture phenomena are highly localized. As the variety of damage mechanism is large, a complete solution of the problem is very difficult to obtain so in order to understand the problem some of the damage mechanisms need to be investigated separately.

The determination of the stress intensity factors for cracks situated among multiple fibers depends on the relative inter–position between fibers and cracks. In particular the nearest fibers and cracks have the strongest influence, referred to as *short–range* interaction. Fibers and other cracks not near to the crack are not very influential referred to as *long–range* interaction. The localization of the problem makes it difficult to perform any statistical analysis of randomly dispersed fibers and cracks effect on the stress intensity factors. Thus it is not reasonable to set up guidelines, which are able to predict the stress intensity factors for a crack situated among a randomly chosen distribution of fibers and microcracks if they do not take into account the relative position of the entities.

In order to explain the interaction effect some elementary problems are considered. They provide information as to how particular arrangement of fibers leads to toughening of the material and other arrangements tend to soften the material. The zone of influence may be estimated by setting up simple models and by doing that the limit for short–range and long–range interaction may be determined.

In some particular configurations of fibers and cracks it is possible to correlate the stress intensity factors with different fiber distributions using only geometrical descriptors. Due to the localization of the phenomena the fibers, which are closest to the crack, have the largest effect and must therefore also be accounted for. A function, which is able to attach the stress intensity factor to a particular arrangement of fibers, may be established.

In section 6.1 various scenarios of crack–fiber configurations are considered and used to obtain information on how the stress intensity factors change due to the interaction effect. In section 6.2 the fiber distribution's influence on the stress intensity factor is

quantified by applying a function, which accounts for the pattern arrangement. Finally in section 6.3 the correlation between the geometrical arrangement of fibers and the stress field inside the fibers is analysed.

6.1 Stress Intensity Factors for Various Fiber–Crack Configurations

The exact position of a crack relative to the position of fibers is decisive for the determination of stress intensity factors because of the stress field introduced by the existence of the fibers. Therefore it is of interest to examine various fiber–crack configurations. Some configurations may lead to shielding and some to enhancement of the fracture toughness, i.e. decrease or increase of the stress intensity factors. The following analysis is devoted to various scenarios consisting of elementary fiber–crack configurations.

Scenario 1

In the first scenario the effect of three particular alignments of fibers is investigated and the zone of influence for fibers interacting with a crack is estimated. The configurations are shown in figure 6.1.

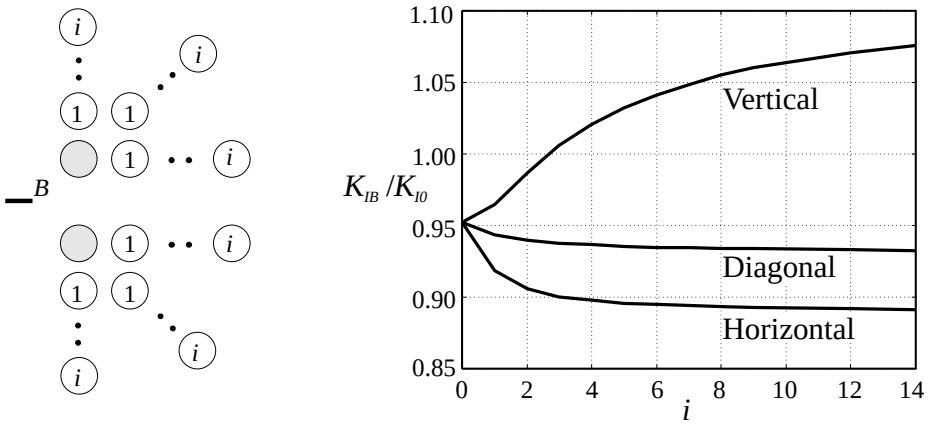

Figure 6.1: Stress intensity factors for the three fiber–crack configurations; horizontal, diagonal(45°), vertical.

The analysis is performed in such way that the initial configuration consists of two shaded fibers. For this configuration the mode I stress intensity factor is calculated. Due to the symmetrical arrangement of fibers the mode II stress intensity factor is zero. For each of the three analyses a pair of fibers is successively added in horizontal, diagonal or vertical direction, respectively. The ratio between the radius of fibers and the crack length is $R/c = 2$. Both the horizontal and vertical distances between the centre of the crack and the centre of the shaded fibers are $3R$. The other fibers are positioned in the horizontal, diagonal and vertical direction by adding to the coordinates of the shaded fibers $(i3R, 0)$, $(i3R, i3R)$ and $(0, i3R)$, respectively. The stress intensity factors

are calculated for successively added pair of fibers and i represents the number of added pairs, i.e. $i = 0$ corresponds to the configuration consisting of the two initial fibers.

When adding fibers in the horizontal and diagonal direction the stress intensity factor decreases and tends to a constant value after addition of more than 10 fibers. The stress intensity factor becomes higher than 1 when adding fibers in the vertical direction. The asymptotic value of the curve must be found for a larger number of fibers than the one shown in the figure. Thus the various positions of fibers influence the stress intensity factor and some configurations are seen to toughen the material while other configurations make the material more vulnerable to crack propagation. The zone of influence is larger in the loading direction than in the other directions.

Scenario 2

In the second scenario an asymmetric configuration is analysed and it consists of a crack situated between two small clusters of fibers at various positions (fig. 6.2).

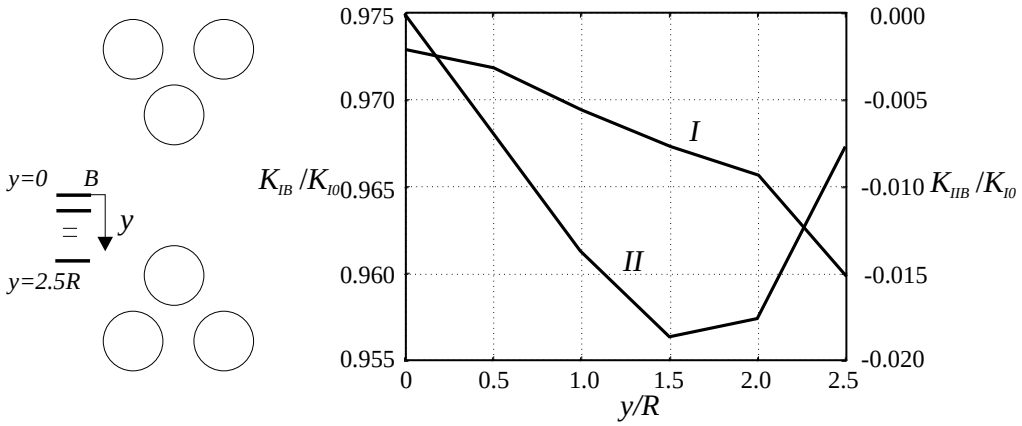

Figure 6.2: Stress intensity factors for an asymmetric fiber–crack configuration.

The crack is moved in the vertical direction leading to an asymmetric fiber–crack interaction. The ratio between the radius of fibers and the crack length is $R/c = 2$. For $y = 0$ the horizontal and vertical distances between the centre of the crack and the centre of the two nearest fibers are $3.5R$ and $3R$, respectively. The horizontal and vertical distances between the centre of the nearest fibers and the centre of the other fibers are $1.3R$ and $2.2R$, respectively. The mode I and II stress intensity factors are calculated at each position of the crack. For $y = 0$, which corresponds to the symmetrical case, the mode I stress intensity factor has its maximum and decreases for $y \neq 0$. This decrease is explained by the strong influence from the nearest fiber, which lowers the stress intensity factor at this particular position and thus increases the fracture toughness. In the symmetrical case the mode II stress intensity factor is equal to zero. In the asymmetric configurations for $y \neq 0$ the mode II stress intensity factor becomes non–zero. A consequence of non–zero mode II stress intensity factor is that the crack branches off if it was to extend. Thus, the asymmetric configuration will contribute to an irregular crack path.

Scenario 3

In the third scenario the shielding/enhancement phenomenon is investigated and the configuration consists of a crack which is situated near three clusters of fibers (fig. 6.3).

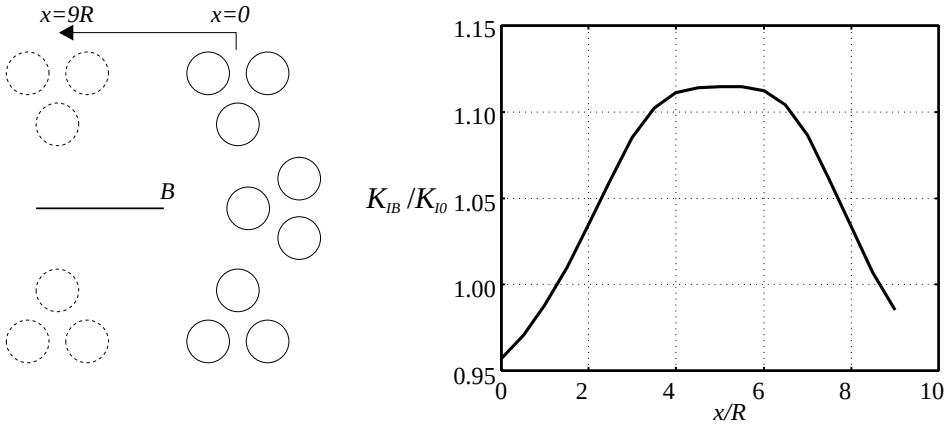

Figure 6.3: Stress intensity factors for a shielding/enhancement fiber–crack configuration.

The two outer clusters are moved in the horizontal direction in order to obtain an enhancement effect. The ratio between the radius of fibers and the crack length is $c/R = 3$. The horizontal and vertical distances between the crack centre and the nearest fiber in the middle cluster are $7.3R$ and 0, respectively. The corresponding distances for the outer clusters for $x = 0$ are $6.5R$ and $4R$, respectively. The inter–fiber centre distances in the middle cluster are $2.2R$ and $1.3R$ in the horizontal and vertical direction. The opposite distances apply for the outer clusters. The mode I stress intensity factor is calculated for each step of x. The shielding occurs for $x < 1.2R$ whereas the fracture toughness is enhanced for $1.2R < x < 8.6R$. As expected, the position of the clusters may lead to both increase and decrease of the stress intensity factor due the stress field introduced by the fibers. Thus roughly speaking, fibers, which are situated above or below a crack, lead to an increase of the stress intensity factor whereas fibers situated beside the crack lead a decrease of the stress intensity factor.

Scenario 4

In the fourth scenario another shielding/enhancement phenomenon is investigated and the configuration consists of a crack, which is situated near two fibers (fig. 6.4).

The fibers are moved along the arc of a circle, which has its centre at the crack tip. The ratio between the radius of fibers and the crack length is $c/R = 4$. The distance between the crack tip and the centre of the fibers is $3.3R$. The mode I stress intensity factor is calculated for various fiber positions along this circular path represented by the angle α. The fibers lead to an enhancement of the fracture toughness for $62° < \alpha < 118°$ and shielding for all other angles.

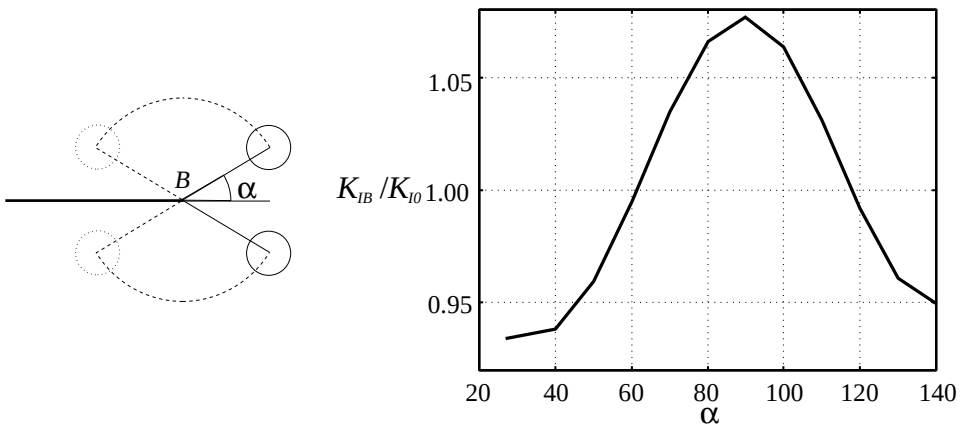

Figure 6.4: Stress intensity factors for a shielding/enhancement fiber–crack configuration.

Scenario 5

In the fifth scenario two similar configurations are considered and the first configuration consists of a crack located in front of a cluster containing 26 fibers (fig. 6.5).

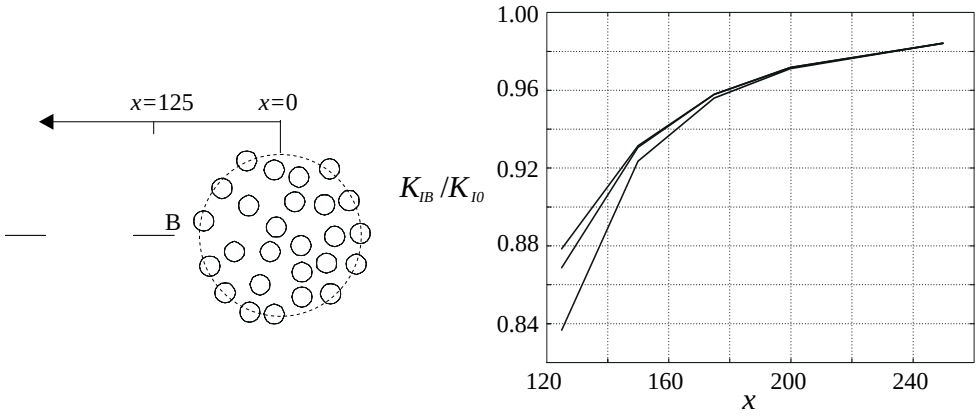

Figure 6.5: Stress intensity factors for the configuration where a cluster is located in front of a crack.

The ratio between the length of the crack and the radius of fibers $c/R = 2$ and the cluster is of circular shape with radius equal to 82.5 points. The crack is moved away from the cluster in the horizontal direction and in the initial position the distance between the centre of the cluster and the centre of the crack is 125 points. For this particular type of configuration three different distributions of fibers are generated within the cluster in order to determine the influence of various arrangements of fibers. During the movement of the crack the stress intensity factor is determined and in the initial position the stress intensity factor is influenced by the exact arrangement of fibers. For larger distances

between the cluster and the crack the effect of the exact position of fibers seems to be smeared out as there is no difference between the results for the three fibers distributions. Thus, for this particular configuration the stress intensity factor is independent of the exact distribution of fibers for $x > 200$ points. The second configuration consists of a cluster of 26 fibers located below a crack (fig. 6.6).

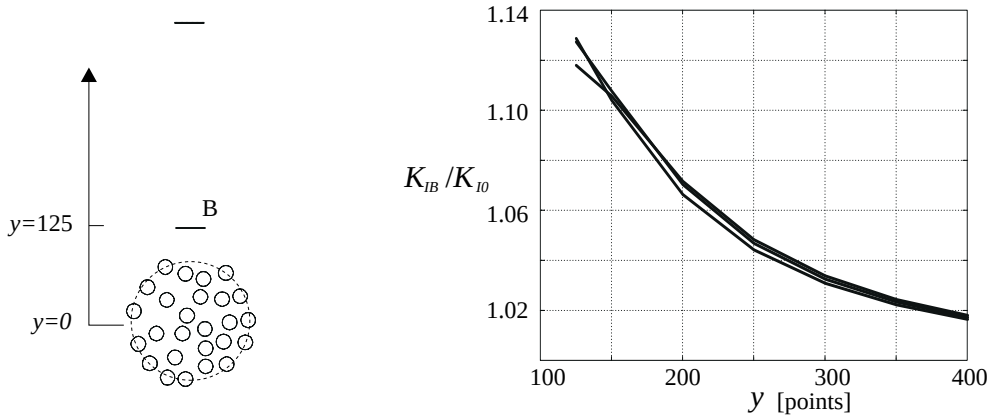

Figure 6.6: Stress intensity factors for the configuration where a cluster is located below a crack.

The similar effect is seen for this configuration, but now the stress intensity factor is not influenced by the exact position of fibers for $y > 400$ points.

The five scenarios do not provide a full description of the fiber–crack interaction but serve more as a illustration of the problem. The results indicate how some fiber–crack configurations lead to an increase of the fracture toughness and other configurations to a decrease of the fracture toughness. Also, some information about the zone of influence may be derived from the analyses.

6.2 Fiber Distributions' Effect on a Neighbouring Macrocrack

As presented in the previous section the relative position between fibers and cracks is crucial for the determination of the stress intensity factors. How the stress intensity factor changes depending on the relative position may be visualized by considering the stress field around a single fiber (fig. 6.7).

In the figure the fiber is represented by the shaded area and the radius of the fiber is 10 points. Contour lines are used to visualize the stress field, which is only calculated in the matrix material. The stress field at the position of a crack is responsible for the determination of stress intensity factor. Roughly speaking, if a crack or more precise the crack tip is situated along the stress line for which $\sigma_y/\sigma_\infty = 1$, the normalized stress intensity factor equals one. Thus, in this case the existence of a fiber does not seem to affect the fracture toughness of the material. If a crack is situated in the area where $\sigma_y/\sigma_\infty < 1$, the stress intensity factor is lower than one and thereby the material is

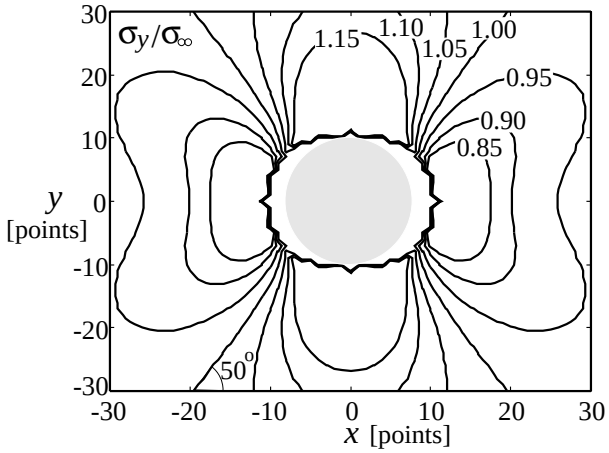

Figure 6.7: Stress field around a fiber represented by constant stress lines.

toughened due to the fiber. On the contrary, if $\sigma_y/\sigma_\infty > 1$ the material is soften because the stress intensity factor is higher than one. Of course the length of the crack enters the determination of stress intensity factors as an integration is performed over the whole length (chap. 2) but as a guideline the stress field consideration is very useful.

The information of the stress field is only valid for one fiber in an infinite medium but may be used to derive a quantifier which is able to correlate the stress intensity factor for a crack situated in the vicinity of various fiber distributions with the spatial dispersion of fibers. This quantifier must take into account both distance and orientation between the fibers and the crack tip as these two parameters seem to be predominant. The following expression may be used as a quantifier:

$$Q(r) = \sqrt{I(r)} \sum_{k=1}^{I(r)} \frac{1}{r_k^2} \, sgn(\theta_0 - |\theta_k|) \sqrt{|\theta_0 - |\theta_k||} \tag{6.1}$$

The function $Q(r)$ is called the *direct correlation function* where $I(r)$ is the number of fibers within a circle defined by radius r and centre at the crack tip (fig. 6.8).

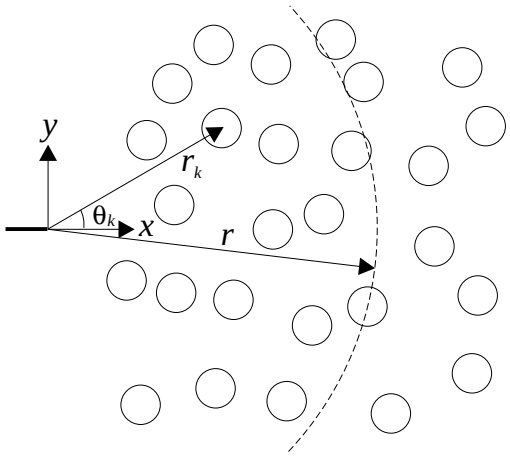

Figure 6.8: Geometry used to calculate the quantifier.

r_k is the radial distance from the crack tip to the k'th fiber. θ_k is the angle between the crack line and the k'th fiber. θ_0 is the angle between the crack line and a fiber for which the stress intensity factor is unaffected. According to figure 6.7 θ_0 is approximately equal to 50° measured between the x–axis and the lower left stress line where $\sigma_y/\sigma_\infty = 1$. The σ_y stress field is symmetrical both in horizontal and vertical direction.

The quantifier corresponds to the second–order intensity function and it may be used to separate different fiber distribution's effect on the stress intensity factors. Thus contrary to the second–order intensity function, which only takes into account the relative position of fibers, the $Q(r)$ function is related to a particular parameter, in this case the stress intensity factor. The function includes the parameter θ_0 indicating the stress line where σ_y/σ_∞ equals one. The stress line is based on the knowledge from the single fiber solution and if other fibers are present the stress line changes due to the interacting stresses. To include the interacting stresses, parameters which account for the inter–fiber interaction may be introduced in the $Q(r)$ function.

The significance of the direct correlation function is illustrated by a crack situated in the vicinity of different fiber distributions. Three categories of distributions are considered; hard–core, single cluster and triple cluster. The distributions, which include 50 fibers of radius 10 points, are generated within a sample area of 300×300 points where the total area is 400×400 points. This corresponds to a volume fraction of fibers equal to 17.5%. The crack is positioned at coordinates (0,200) points with total crack length $2c = 60$ points and no fibers are generated in the boundary area. The various distributions are generated inside the sample area and the stress intensity factors are calculated using the same material properties as in chapter 5. Three distributions from each category are shown in the following and for each distribution the direct correlation function is determined.

Hard–core

Three hard–core distributions are generated using the concept from chapter 4 where the fibers are dispersed randomly with the condition that fibers do not overlap (fig. 6.9).

The direct correlation function is able to differentiate between the three fiber distributions and the related stress intensity factors. Thus, the direct correlation function increases for an increased fracture toughness and vice versa. On a large scale the three distributions seem to be similar but observing the local areas near the crack tip a dissimilarity is detected. It is in these areas that the distribution of fibers has the largest influence corresponding to the short–range interaction. This is also accounted for in the direct correlation function by the factor $1/r_k^2$ and the sgn function. In the distribution shown in figure 6.9a fibers are located closer to the crack tip than in the other distributions. This particular location results in a lowering of the stress intensity factor.

Single Cluster

In the generation of single cluster distribution the centre point of the cluster is fixed and fibers are dispersed using the hard–core model both inside and outside the cluster. The centre points of the clusters in the three single cluster distributions are randomly chosen (fig. 6.10).

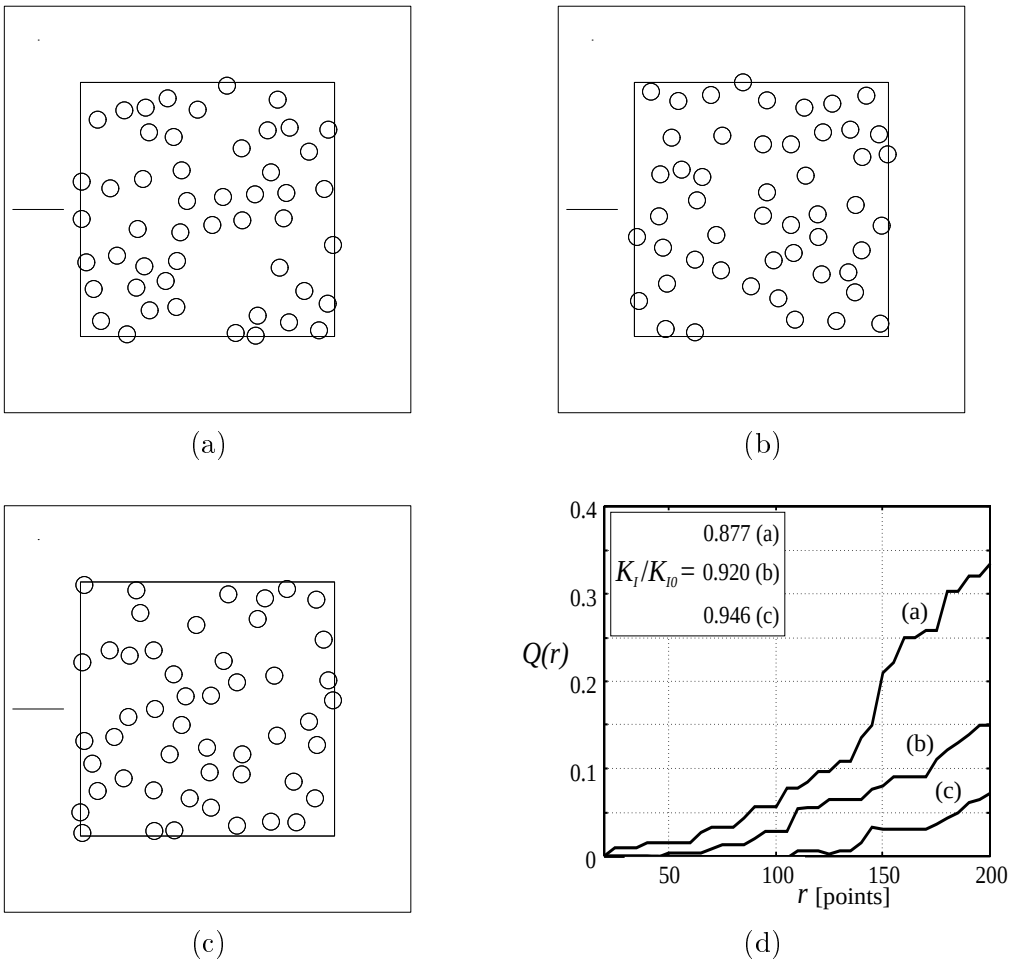

Figure 6.9: (a)-(c) Various distribution of the hard–core models, (d) direct correlation function.

The cluster is of elliptic shape where minor and major axes are equal to 175 and 200 points respectively and the number of fibers contained within the cluster is 30. In this case the direct correlation function is also able to differentiate between the three fiber distributions. The distribution in figure 6.10a has fibers very close to the crack tip and in positions, which increase the fracture toughness. As opposed to this the distribution in figure 6.10c has the closest fibers located at positions which results in an increase of the stress intensity factor.

Triple Cluster

The centre points for the clusters in the triple cluster distribution are also randomly chosen but with the condition that the cluster areas are not allowed to overlap. The clusters each contain a third of the fibers and again three various distributions are generated (fig. 6.10).

The clusters are of elliptic shape where minor and major axes are equal to 130 and 145

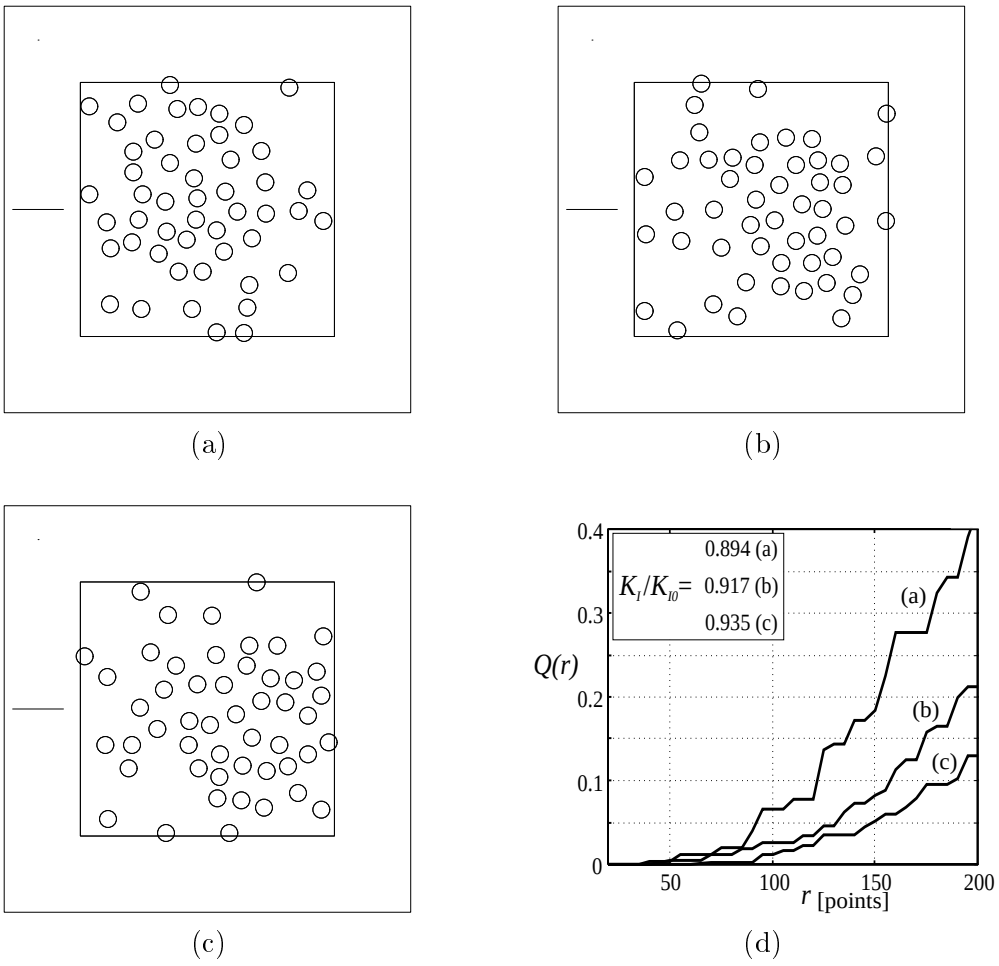

Figure 6.10: (a)-(c) Various distribution of the single cluster models, (d) direct correlation function.

points, respectively. As in the previous examples a distinction can be made between the different fiber distributions. For all presented examples it is the short–range interaction, which is decisive for the determination of stress intensity factors. The long–range interaction has only limited influence on the stress intensity factors.

6.3 Correlation Between Fiber Arrangements and Fiber Stresses

The geometrical arrangement of the presented microstructures are correlated with the von Mises stress inside fibers. The fiber distributions are described in form of the nearest neighbour distances and orientations (Tab. 6.1).

As expected the nearest neighbour distance indicates the degree of clustering and the correlation between the fiber arrangement and the stress field inside the fibers must take into account both distance and orientation. Similar to the results shown in figure 5.6, the

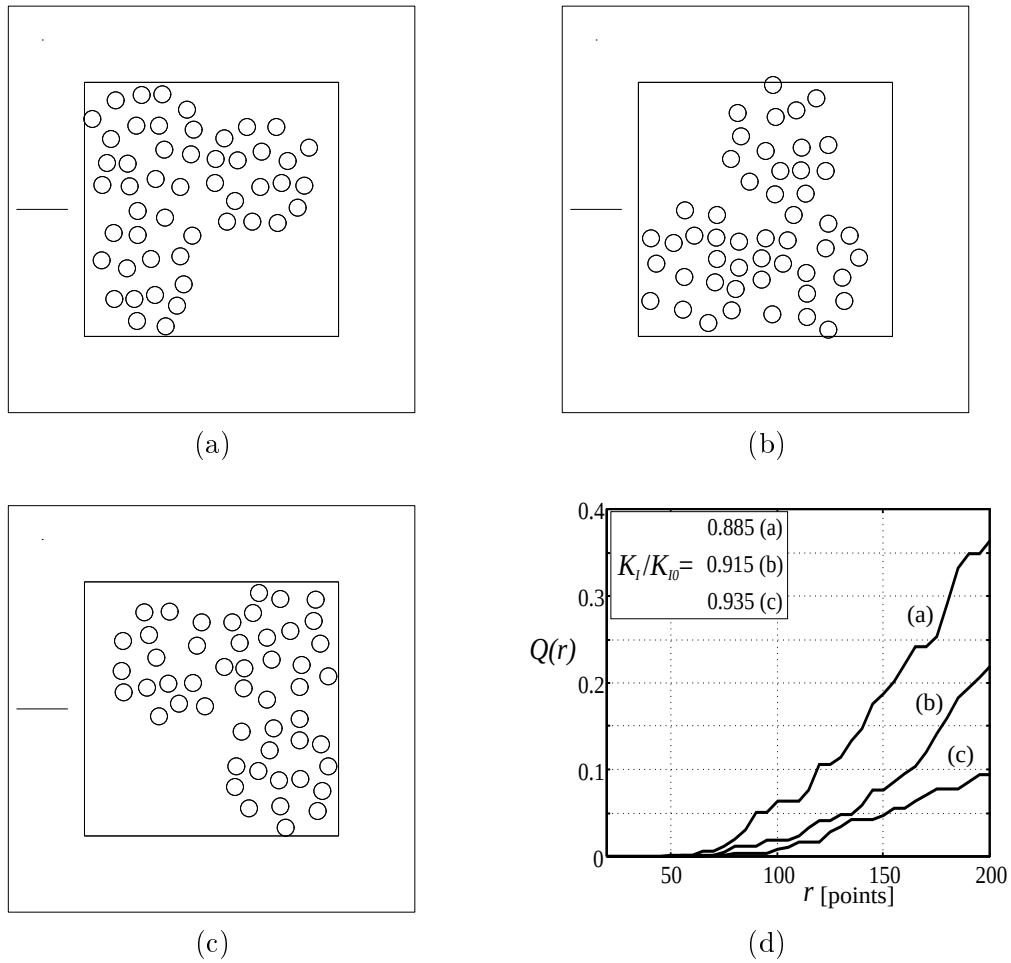

Figure 6.11: (a)-(c) Various distribution of the triple cluster models, (d) direct correlation function.

Table 6.1: Mean value and variance of nearest neighbour distances and orientations and the mean value of von Mises stress inside the fibers, distances are measured in points, orientations in degrees and stresses are normalized with σ_∞.

	N.n. distance		N.n. orientation		Von Mises stress	
Distribution type	Mean	Variance	Mean	Variance	Mean	Variance
hard–core(a)	33.4	47.1	45.2	823	1.046	0.0049
hard–core(b)	33.1	32.7	36.6	767	1.047	0.0043
hard–core(c)	31.5	59.1	46.4	898	1.060	0.0091
single cluster(a)	30.7	57.2	50.6	928	1.076	0.0137
single cluster(b)	32.2	74.4	45.7	957	1.056	0.0070
single cluster(c)	33.1	103.1	44.2	931	1.041	0.0066
triple cluster(a)	27.8	6.5	39.7	1098	1.070	0.0144
triple cluster(b)	28.4	15.8	53.1	1078	1.100	0.0127
triple cluster(c)	26.8	7.1	54.3	1148	1.120	0.0170

relation between the von Mises stress and the ratio between the mean nearest neighbour distance and orientation is calculated (fig. 6.12).

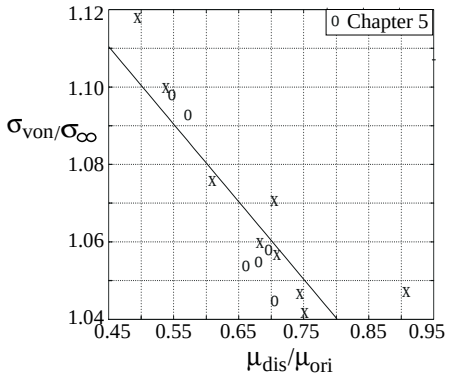

Figure 6.12: Correlation between the mean value of the von Mises stress and the ratio between the mean value of the nearest neighbour distance and the nearest neighbour orientation for the distributions presented in this chapter and in chapter 5.

The tendency is also clear in this case and the results correspond very well to the results from the previous chapter.

Chapter

7

Microstructural Influence on Fracture Toughness

As mentioned in the previous chapter some arrangements of fibers may change the stress intensity factor of a neighbouring macrocrack. In the following a similar investigation is performed in order to analyse the effect of microcracks initiating at the interface between fibers and the matrix.

The configuration, which is considered here, consists of a macrocrack located in the vicinity of a fiber distribution. The pattern of fibers itself may change the fracture toughness of the macrocrack, but how the fracture toughness is affected if microcracks initiate at the interface is also of interest. The initiation of microcracks at the interface is usually caused by a weaker strength of the interface as compared to the matrix material. The variation of the stress field around the fibers has decisive influence on microcracks' initiation sites and their subsequent development (sec. 5.3). Thus, the degradation of the material happens gradually and in order to perform the analysis, the load range applied must go from the load level, for which no microcracks are initiated, to the load level, for which microcracks appear at all interfaces. Various fiber distributions need to enter the analysis as the exact arrangement affects both the fracture toughness and the nucleation of microcracks. Two types of microcracking are considered; one type which considers the initiation of interface (tangential) cracks and another type which considers matrix (radial) cracks. Both types of damage mechanisms are applied to various configurations of fibers and macrocracks and an estimate of the fracture toughness may be given for the particular configurations by determining the stress intensity factor of the macrocrack as the material deterioates during the load increase.

The problem of estimating the fracture toughness for an array of microcracks in the neighbourhood of a macrocrack was investigated by Kachanov *et al.* [10]. They concluded that the exact positions of microcracks are crucial for the determination of stress intensity factors and various configurations may either increase or decrease the fracture toughness. Pijaudier-Cabot and Bažant [17] considered the fracture toughness for various configurations of a crack situated among multiple inclusions. Hu *et al.* [8] estimated the shielding/enhancement effect on various configurations of cracks situated among multiple voids.

In section 7.1 a procedure, which determines the initiation of cracks is presented. It

involves additional interaction terms in the stress field analysis, which arises both from the macrocrack and the initiated microcracks. In section 7.2 and 7.3 the procedure is applied for interface and matrix cracks, respectively. Various distributions are analysed in order to indicate the tendency of how the arrangements of fibers affect the fracture toughness.

7.1 Crack Nucleation Procedure

The configuration consists of a macrocrack located in the vicinity of a dispersion of fibers, which have initially perfectly bonded interfaces. As the applied load is increased, the stress field at the interface reaches a critical value, which leads to the nucleation of cracks. When and where the cracks appear at the interface depends on the local stress field around the fibers, which again is influenced by the dispersion of fibers and cracks. It is assumed that cracks initiates at positions where maximum stress occurs and, as in section 5.3, the tangential stress component leads to matrix cracks and the radial stress component leads to interface cracks. Only one crack is assumed to initiate at each fiber and as the initiation of cracks does not occur at the same load level, the load is increased until cracks appear at all interfaces. During the load increase microcracks initiate at the interface and it is assumed that the strength of the interface is weaker than the strength of the matrix so that microcracks initiate rather than the macrocrack extends. For every load step the stress intensity factor for the macrocrack is calculated and it is determined whether the fracture toughness is increased or decreased. According to the method from section 1.2 the stress field determination is based on the interaction from the fibers but both the macrocrack and the microcracks, which initiate during the load increase, interact with the local stress field. Therefore it is necessary to include additional terms in the stress field analysis.

Before the local stress field in the matrix is determined the stress field in the fibers are calculated according to the iterative procedure (Tab. 1.3). Then for each load step the pressure distribution on both the macrocrack and the microcracks is determined using the theory from section 2.3. The local stress field $\boldsymbol{\sigma}_D$ at the arbitrary matrix position D is then determined as:

$$\boldsymbol{\sigma}_D = \boldsymbol{\sigma}_\infty + \sum_{i=1}^{N_1} \boldsymbol{\sigma}_{iD} + \boldsymbol{\Lambda}_{cD}\langle \tilde{\mathbf{p}}_c \rangle + \sum_{i=1}^{N_2} \boldsymbol{\Lambda}_{iD}\langle \tilde{\mathbf{p}}_i \rangle \tag{7.1}$$

where $\boldsymbol{\sigma}_{iD}$ is the stress field at the point D due to unbalanced tractions at the i'th fiber. The average pressure distributions $\langle \tilde{\mathbf{p}}_c \rangle$ and $\langle \tilde{\mathbf{p}}_i \rangle$ act at the macrocrack and the i'th microcrack, respectively. The transmission factors $\boldsymbol{\Lambda}_{cD}$ and $\boldsymbol{\Lambda}_{iD}$ represent the stress field at the point D due to unit pressure distributions at the macrocrack and the i'th microcrack. N_1 is the total number of fibers and N_2 is the number of microcracks initiated at a given load level. In the initial configuration where no microcracks exist, i.e. $N_2 = 0$, the local stress field is calculated around the fibers. Maximum value of the stress component of interest is determined as well as the angle at which the maximum value occurs. Whether the microcracks initiate or not depends on the critical value of the stress field. The critical value may be related to the strength of the interface and if the stress component exceeds the critical value a microcrack initiates. As it is not reasonable to assume that the strength of the interface in the tangential and radial direction is equal, two critical values are needed. The crack length of the initiated microcrack is determined

as a function of the local maximum stress field:

$$\begin{aligned} \delta c_r &= A_r \max(\sigma_r) \\ \delta c_\theta &= A_\theta \max(\sigma_\theta) \end{aligned} \tag{7.2}$$

where A_r and A_θ are constants. Microcracks only appear in some of the interfaces and therefore the load is increased. The stress field in the fibers is recalculated and the pressure distributions on both the macrocrack and the new microcracks are determined. In the calculation of the local stress field the interaction from the new microcracks is included. The iterative procedure is summarized in table 7.1.

Table 7.1: The iterative procedure for initiation of interface cracks.

---

initial state Perfect bounding in interfaces

Determine stress field inside fibers

Determine pressure distribution on the macrocrack

The stress intensity factor is calculated of the macrocrack

Determine local stress field around fibers (incl. interaction from the macrocrack)

Sampling of $\max(\sigma)$ and θ_{max} around all fibers

iterations

- If $\max(\sigma) > \sigma_{critical} \Rightarrow$ crack initiation
- A crack is introduced at θ_{max} with length $a = a(\max(\sigma))$
- The load is increased
- Determine stress field inside fibers
- Determine pressure distribution on the macrocrack and the new microcracks
- The stress intensity factor of the macrocrack is calculated
- Determine local stress field around fibers (incl. interaction from the macrocrack and the new microcracks)
- Sampling of $\max(\sigma)$ and θ_{max} around fiber where microcracks are not initiated

stop iteration when microcracks appear in all fibers

end

The iterative procedure applies both for the initiation of interface and matrix cracks and in the following an example of interface crack initiation is given. A configuration with nine fibers dispersed in a regular arrangement in front of a macrocrack is considered (fig. 7.1a).

The dispersion of fibers and the macrocrack corresponds to the configuration shown in figure 6.3 for $x = 0$. The stress field inside the fibers is calculated and in figure 7.1b it is represented by the von Mises stress where the regularity also is emphasized. The iterative procedure is applied where the crack length constant $A_r = 1.0\,\mathrm{mm}^3/\mathrm{N}$ and the

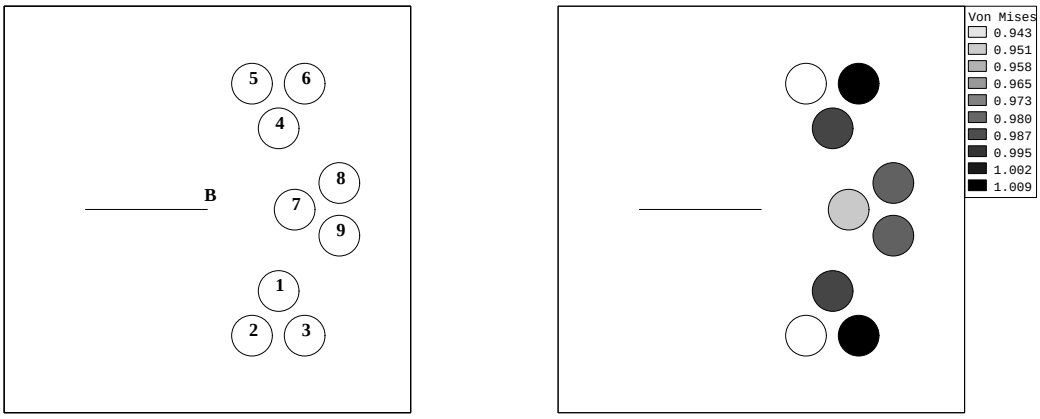

(a) (b)

Figure 7.1: Configuration with 9 regularly dispersed fibers in the vicinity of a macrocrack; (a) model, (b) von Mises stress inside fibers, normalized with σ_∞.

critical value of the interface stress is $\sigma_{r,critical} = 2.0\,\mathrm{N/mm^2}$. Five load steps are needed to initiate interface cracks at all fibers (Tab. 7.2).

Table 7.2: Iterative process during the load increase.

	Load step				
Parameter	1	2	3	4	5
σ_∞ [N/mm^2]	0.90	1.05	1.20	1.30	1.35
K_I/K_{I0}	0.9395	0.9407	0.9457	0.9461	0.9450
K_{II}/K_{I0}	0.0	0.0	0.0003	0.0003	0.0003
Number of cracks	0	2	5	7	9
$\sigma_{r,max}(\theta_{r,max})$ [N/mm^2]	([°]):				
Fiber 1	1.66(270)	1.94(270)	2.06(270)	–	–
Fiber 2	1.36(295)	1.59(295)	1.81(90)	1.96(90)	2.04(90)
Fiber 3	1.47(90)	1.71(90)	1.91(90)	2.07(90)	–
Fiber 4	1.66(90)	1.94(90)	2.06(90)	–	–
Fiber 5	1.36(65)	1.59(65)	1.81(270)	1.96(270)	2.05(270)
Fiber 6	1.47(270)	1.71(270)	1.91(270)	2.07(270)	–
Fiber 7	1.61(95)	1.88(95)	2.04(95)	–	–
Fiber 8	1.78(90)	2.08(90)	–	–	–
Fiber 9	1.78(270)	2.08(270)	–	–	–

The presence of the fibers lowers the stress intensity factor of the macrocrack, but as the interface cracks are initiated the stress intensity factor is increased and thus the interface cracks decrease the fracture toughness. The stress intensity factor for mode II crack opening becomes non-zero at load step 3 and as shown in figure 7.2a the configuration becomes unsymmetric when an interface crack initiates at fiber 7.

Figure 7.2b shows the crack initiation at load step 5 where interface cracks appear at all

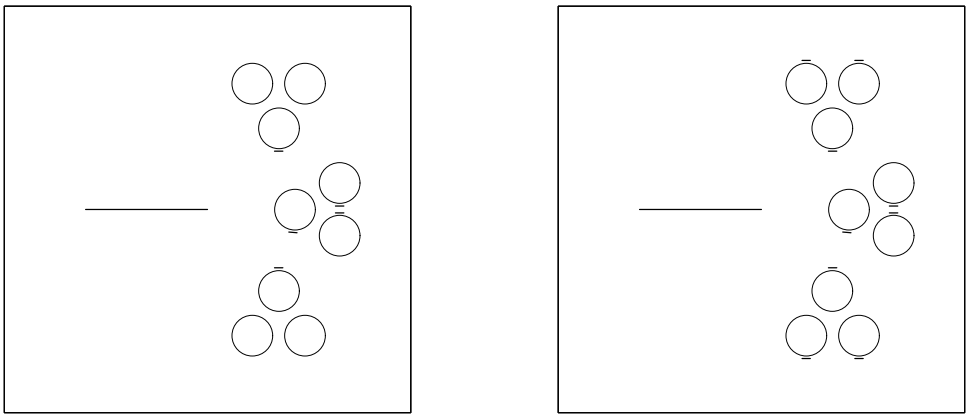

Figure 7.2: Nucleation of interface cracks; (a) $\sigma_\infty = 1.20\,N/mm^2$, (b) $\sigma_\infty = 1.35\,N/mm^2$.

fibers and the iterative procedure is stopped. Both for fiber 2 and 5 the angle, at which maximum value occurs, changes from load step 2 to 3. This illustrates the effect of new cracks entering the local stress analysis.

7.2 Nucleation of Interface Cracks

In the following various configurations and distributions are analysed in order to investigate the influence of interface cracks. Four typical configurations are simulated and each of them consists of 50 fibers dispersed in the vicinity of a macrocrack. The first configuration consists of a macrocrack situated in front of a cluster containing 50 fibers (fig. 7.3).

The cluster is circular with radius equal to 125 points and the distribution of fibers inside the cluster is generated using the hard–core model. The ratio between the crack length and the radius of fibers is $c/R = 2$. The iterative procedure is applied using the data shown in table 7.3.

Table 7.3: Data used for the analysis.

E_a	ν_a	E_m	ν_m	A_0	A_r	$\sigma_{r,critical}$	$\sigma_{\infty,initial}$
[N/mm^2]		[N/mm^2]			[mm^3/N]	[N/mm^2]	[N/mm^2]
73000	0.3	3174	0.35	1.15	1.0	2.0	0.9

The dispersion of fibers itself lowers the stress intensity factor of the macrocrack and thus increases the fracture toughness. During the load increase interface cracks gradually appear at the interfaces. For the configuration in figure 7.3d an enlarged view of a partial degraded material is shown in figure 7.4a. The corresponding fully degraded material is shown in figure 7.4b.

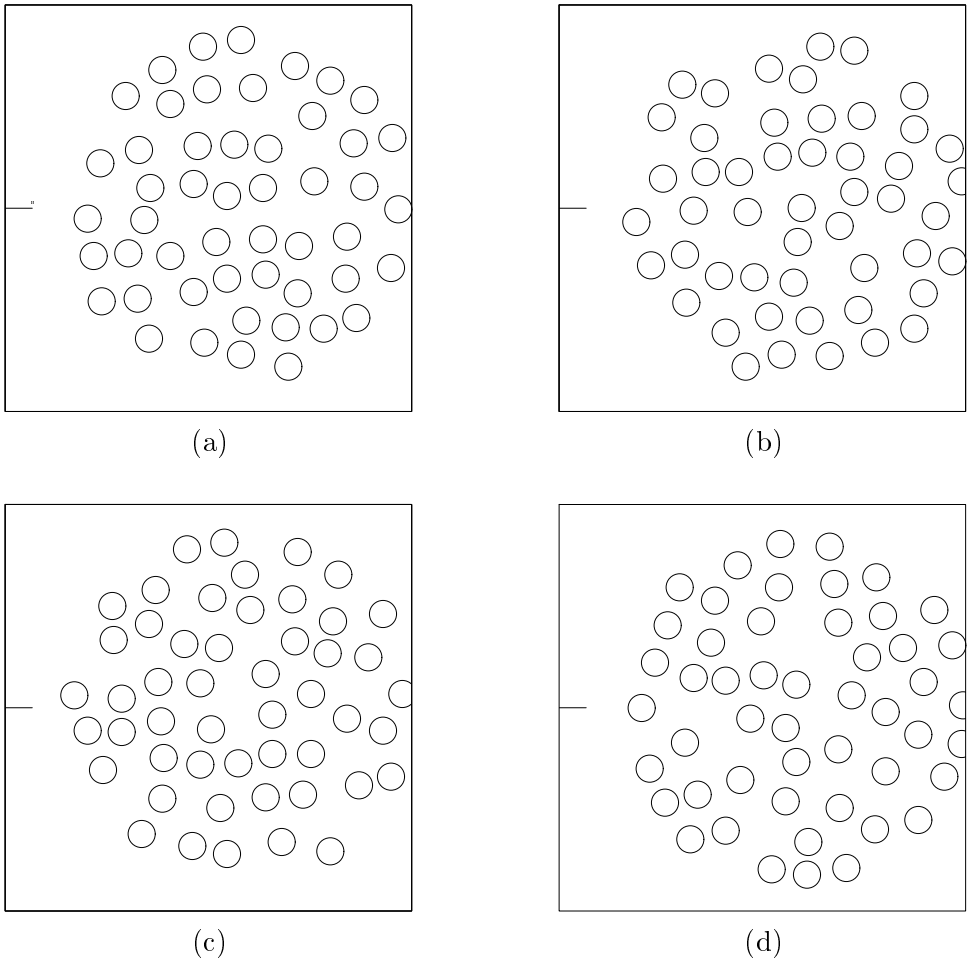

Figure 7.3: Four distributions of fibers generated within a cluster in front of a macrocrack.

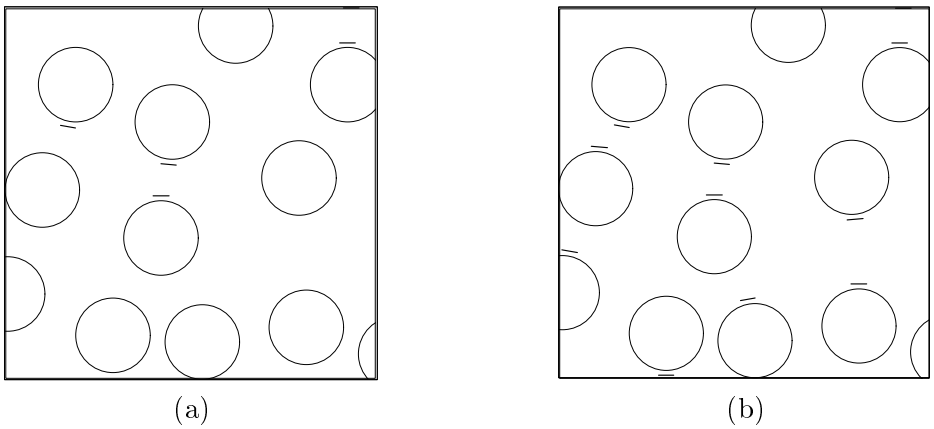

Figure 7.4: Enlarged view of the the configuration shown in figure; (a) partial degraded ($\sigma_\infty = 1.2\,N/mm^2$), (b) fully degraded ($\sigma_\infty = 1.7\,N/mm^2$).

The interface cracks appear in the vicinity of two distinct angles, $\theta = 90°, 270°$, corresponding to the analysis presented in section 5.3. The deviation from these angles is caused by the varying interaction which exists in non–regular arrangements of the fibers. The number of interface cracks and the stress intensity factor at crack tip B are calculated during the load increase (fig. 7.5).

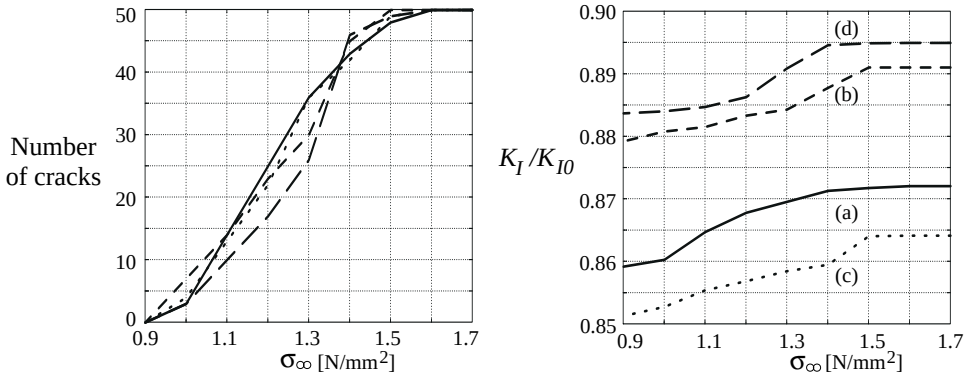

Figure 7.5: Number of initiated cracks and normalized stress intensity factors as a function of the applied load.

All patterns exhibit the same tendency where the stress intensity factor is increased during the load increase. Thus, the fracture toughness is decreased due to the existence of the interface cracks. The various distributions have different levels of the stress intensity factor due to the interaction from the fibers near to the crack tip. Another configuration, which is of interest consists of two clusters each containing 25 fibers, which are situated above and below a macrocrack (fig. 7.6).

Also in this case four distributions are generated and the clusters are of elliptic shape with semi–minor and semi–major axes equal to 60 and 110 points, respectively. The ratio between the crack length and radius of the fibers is equal to $c/R = 2$. In this configuration the stress intensity factor of the macrocrack is increased due to the presence of the fibers. The iterative procedure is applied and the number of interface cracks and the stress intensity factor at crack tip B are calculated (fig. 7.7).

The opposite effect is now seen to be predominant where the nucleation of cracks lowers the stress intensity factor of the macrocrack. Thus, although the fibers decreased the fracture toughness the interface cracks are now seen to reverse the effect. Finally, two similar configurations are analysed. They consist both of three clusters situated in front of the macrocrack (fig. 7.8).

The clusters each consist of a third of the 50 fibers and are of circular shape with radius equal to 65 points. The only difference between the configurations is that the two outer clusters are shifted with respect to the middle cluster. The iterative procedure is applied and the number of interface cracks and the stress intensity factor at the crack tip B are calculated (fig. 7.9).

Both configurations increase the fracture toughness by the presence of the fibers but as interface cracks are initiated, the fracture toughness is decreased. The relatively high

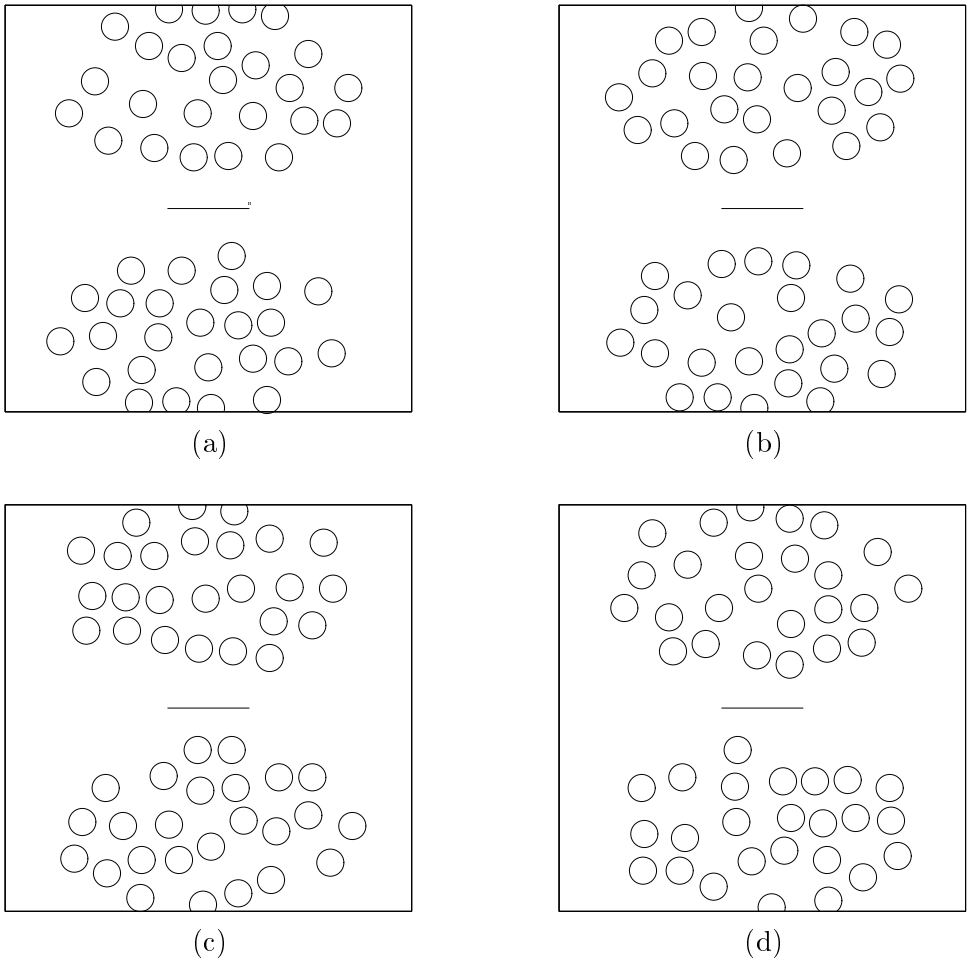

Figure 7.6: Four distributions of fibers dispersed in two clusters situated above and below a macrocrack.

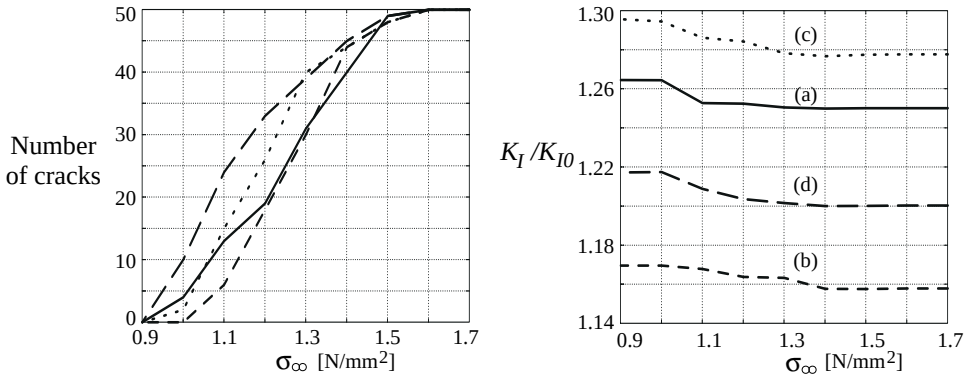

Figure 7.7: Number of initiated cracks and normalized stress intensity factor as a function of the applied load.

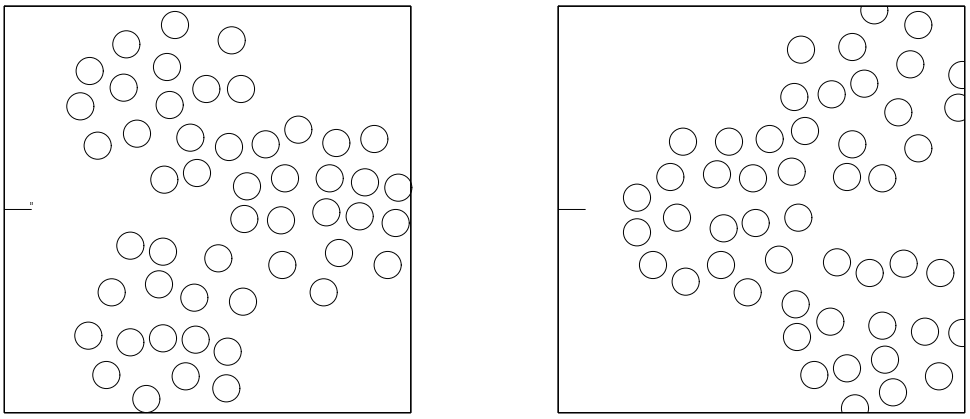

Figure 7.8: Similar configurations with three clusters situated in front of a macrocrack.

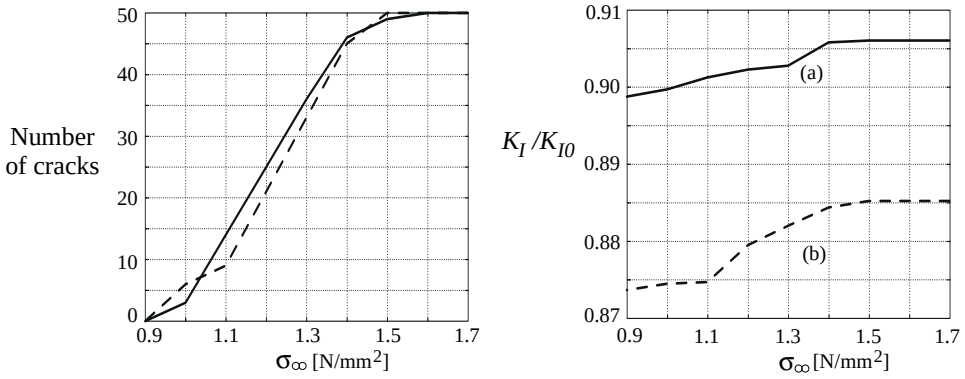

Figure 7.9: Number of initiated cracks and normalized stress intensity factor as a function of the applied load.

increase of the stress intensity factor for the configuration in figure 7.8b at load level $\sigma_\infty = 1.3\,\mathrm{N/mm^2}$ is a result of the fibers very near to the crack tip. Thus, when interface cracks initiate at these fibers the interaction effect is very influencial.

7.3 Nucleation of Matrix Cracks

The following analysis accounts for the initiation of radial cracks. Only two configurations are considered corresponding to the arrangements in figure 7.3a and 7.6a. In the iterative procedure the crack length constant $A_\theta = 2.5\,\mathrm{mm^3/N}$ and the critical radial stress $\sigma_{\theta,critical} = 0.6\,\mathrm{N/mm^2}$. An enlarged view of the first configuration is shown in figure 7.10a where matrix cracks have been initiated.

As the cracks may interfere with the neighbouring fibers the crack may need to be reduced until it does not coincide with other fibers (fig. 7.10b). Again the iterative procedure is applied and the number of matrix cracks and the stress intensity factor at crack tip B

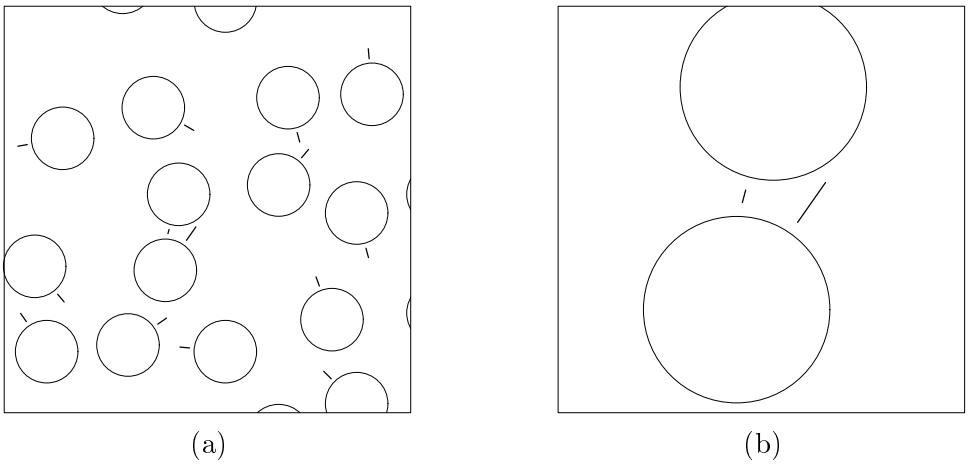

Figure 7.10: (a) Enlarged view of the fiber distribution showing radial cracks, (b) effect of reduced crack length.

are calculated during the load increase (fig. 7.11).

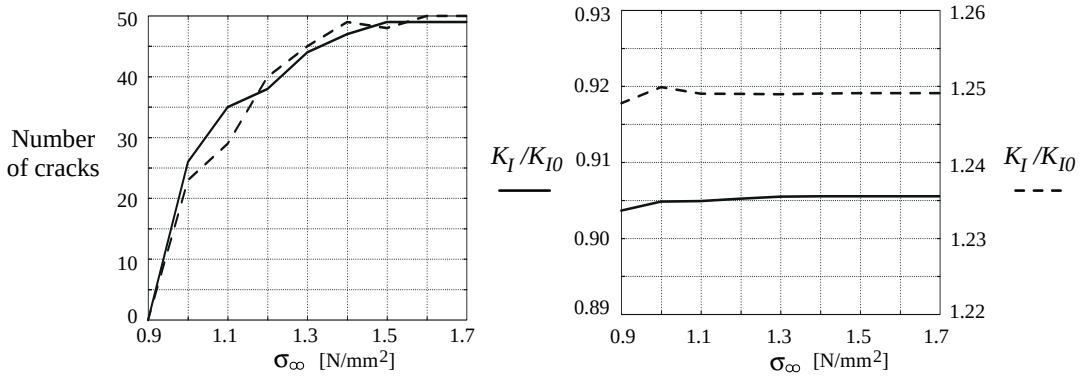

Figure 7.11: Number of initiated cracks and normalized stress intensity factor as a function of the applied load (the solid line corresponds to the configuration in figure 7.3a and the dashed line corresponds to figure 7.6a).

The initiation of matrix cracks has almost no effect on the stress intensity factor of the macrocrack. Thus, either the exact position of the matrix cracks does not affect the stress intensity factor or the interaction effects are cancelled.

Chapter

8

Trajectories of Percolating Cracks

The damage evolution in a composite material is of very complex nature. Some damage mechanisms may be analysed properly by simplifying and decomposing the problem into well–defined subproblems. The aim of the present analysis is to investigate how various types of fiber distributions affect the crack path of a percolating crack.

The problem considered here consists of a crack, which is located at the edge of a microstructure and the crack is then allowed to extend through the microstructure. The distribution of fibers influences the local stress field in the matrix and consequently it also influences the development of cracks. The crack path becomes irregular as it develops through the microstructure and in accordance with chapter 3 the crack path may consist of both pure matrix cracking and interface cracking. The irregularity of the crack path for the various distributions can be described by characteristic parameters. Comparing the characteristic parameters for crack paths the influence of the fiber distribution type may be given.

Real microstructures containing percolating cracks are analysed and the crack paths are measured and compared with corresponding numerical models. As seen in chapter 3 the crack path in the numerical models can be altered by changing a critical value of the interface strength. Thus, an estimate of the strength of the interface may be given by comparing the characteristic parameters for crack paths in real microstructures with crack paths in numerical models where the critical values for the strength of the interface have been altered.

Pyrz and Bochenek [22] investigated the crack propagation in a two–phase material by discretization of the microstructure and applying a truss model. Gradually the damage evolution appears as the load is increased and final damage state consists of microcracks and a percolating crack. They correlated the load carrying capacity with various types of fiber distributions. A further extension of the analysis is presented in Pyrz and Bochenek [23].

In section 8.1 the crack growth in four types of simulated microstructures is analysed in order to estimate how the distribution of fibers affects crack path parameters. In section 8.2 the crack growth in real microstructures is analysed numerically in order to estimate the strength of the interface.

8.1 Percolating Cracks in Simulated Microstructures

In order to analyse how the dispersion of fibers affects the crack path, four types of distribution are applied. For each of them a crack is initiated at various positions along the edge of the microstructure. The four types of microstructures correspond to those presented in chapter 5; regular(II), hard–core(II), single cluster(II) and triple cluster(II). The distributions are generated using model II so the microstructures consist of a sample area, which contains the actual fiber distribution, and a boundary area, which contains a hard–core fiber distribution similar for the four types of microstructures. Three possible locations of initial cracks are selected for the regular distribution and five possible locations are selected for other distributions (fig. 8.1).

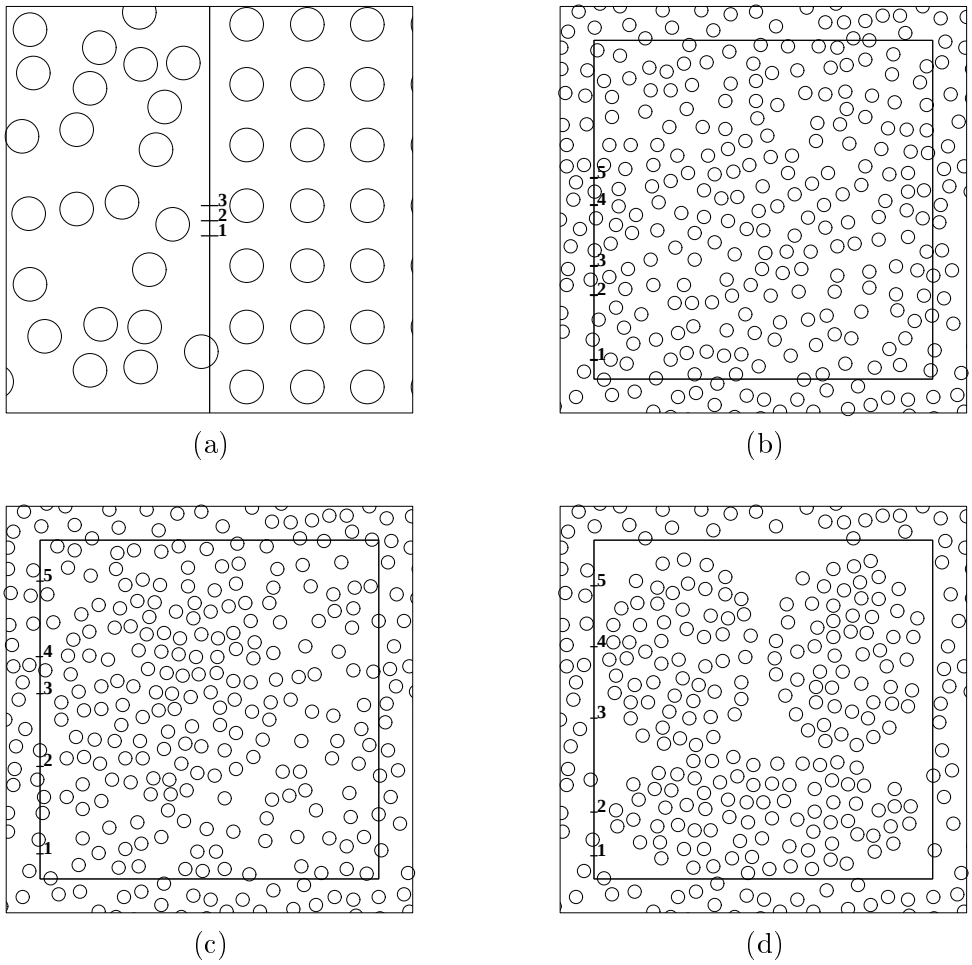

Figure 8.1: The positions of the initial cracks; (a) regular(II), (b) hard–core(II), (c) single cluster(II), (d) triple cluster(II).

The cracks are analysed separately as they extend through the sample area. The crack propagation is determined according to the theory presented in chapter 2 and 3. By applying this theory, interaction effects from all fibers are included. For the distributions used here, each crack step includes interaction effects from 800 fibers. This demands

considerable computational time and in order to reduce the time, locality criteria are introduced. The zone of influence for particular configurations is investigated in appendix C and an estimate of the locality is given by applying two criteria. The first criterion gives the range of locality r_i for the determination of the local stress field, and the second one gives the range of locality r_c for the determination of crack–fiber–crack interaction. Another important parameter is the critical value $\tilde{U}_{cr}$ (sec. 3.2) representing the strength of the interface. The parameter allows to change the crack path and must therefore be constant for all analyses. The data used in the analysis are shown in table 8.1.

Table 8.1: Data used for the analysis.

E_a	ν_a	E_m	ν_m	A_0	A_1	A_2	$\tilde{U}_{cr}$	r_i	r_c
[N/mm^2]		[N/mm^2]			[mm]	[mm^3/N]	[N/mm^2]	[points]	[points]
73000	0.3	3174	0.35	1.15	2.0	2.0	1.0	200	150

The number of crack steps needed to percolate the sample area is approximately 110 and the crack paths now appear as fracture profiles (fig. 8.2).

With the exception of the regular distribution the crack paths are not easily distinguished and therefore various descriptors are applied (Tab. 8.2).

Table 8.2: Fracture parameters for the various crack paths, lengths are measured in points and angles in degrees.

Distribution	Crack 1	Crack 2	Crack 3	Crack 4	Crack 5	Mean
Roughness:						
regular(II)	1.000	1.131	1.118	–	–	1.083
hard–core(II)	1.086	1.093	1.087	1.091	1.091	1.090
single cluster(II)	1.037	1.061	1.083	1.092	1.074	1.069
triple cluster(II)	1.127	1.114	1.070	1.082	1.092	1.097
Mean crack length:						
regular(II)	2.11	1.84	1.85	–	–	1.93
hard–core(II)	2.18	2.06	2.13	2.04	2.15	2.11
single cluster(II)	2.33	2.20	2.12	2.03	2.15	2.17
triple cluster(II)	2.00	1.95	2.18	1.92	2.22	2.05
Crack angle:						
regular(II)	0.7	24.4	22.7	–	–	15.9
hard–core(II)	18.5	18.8	18.6	18.5	19.7	18.8
single cluster(II)	9.8	15.6	16.6	17.6	16.8	15.3
triple cluster(II)	22.0	21.2	15.9	18.0	19.1	19.2

The roughness is defined as the ratio between the actual crack curve divided by its projection. Thus if there was no interaction, the roughness parameter would be equal to 1 and the more irregular the crack path the higher the roughness parameter becomes.

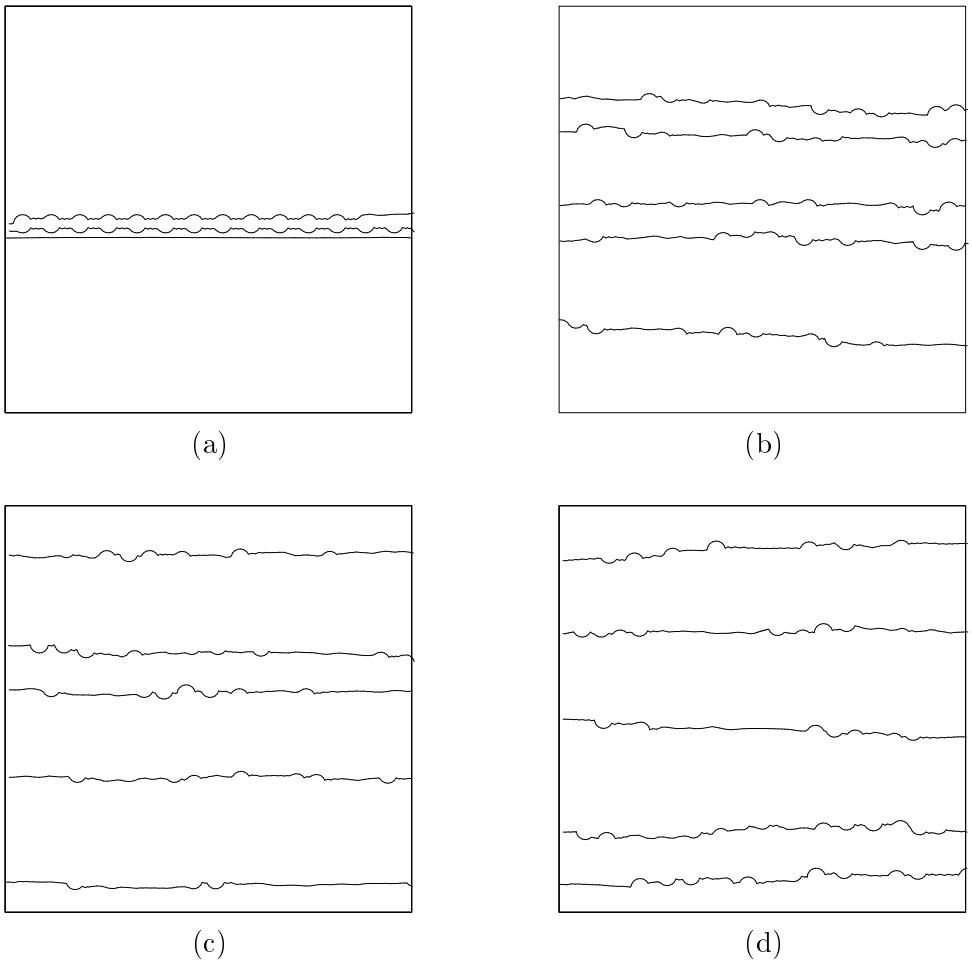

Figure 8.2: Crack paths in the distributions; (a) regular(II), (b) hard–core(II), (c) single cluster(II), (d) triple cluster(II).

This also corresponds to the roughness calculated for the four distributions where the triple cluster has the highest mean value. Crack 1 in the regular distribution is a straight line because of the symmetry and correspondingly the roughness parameter is equal to 1. It is of course crucial for the crack path where the crack is initiated and in particular the clustered distributions are very sensitive. Except from the regular distribution the mean value of the crack lengths for the triple cluster is lowest and correspondingly the mean value of the crack angles is the highest. The reason for this is that the stress field varies much more in a clustered distribution.

The analysis clearly shows that the distribution of fibers affects the crack path and as it might be expected the clustered distribution tends to have a more irregular path.

8.2 Percolating Cracks in Real Microstructures

In order to investigate the damage evolution in real material a specimen made of carbon/epoxy has been exposed to an unidirectional load and the microstructure is investigated. The specimen made as a symmetric laminate with eight layers, four layers in the loading direction and four layers transverse to the loading direction. Areas of the microstructure in the transverse layers containing a percolating crack have been sampled with respect to the fiber centres and the crack path. The fiber centres and the crack path have been measured using an image analysis system. A corresponding numerical model is generated by applying the measured fiber centres and a crack is initiated at the edge of the microstructure. The crack is allowed to extend through the microstructure and compared with the crack path in the real microstructure (fig. 8.4).

The crack growth path in modelled microstructures is determined as in the previous section. However, it does not coincide with the crack path in the real material. It should not be expected that they coincide as the crack path in the real material is influenced by several other parameters. Instead it is more reasonable to compare the roughness of the fracture profiles. The roughness for the real microstructures is found by measuring the crack path using crack lengths comparable to the simulated models. The roughness for the corresponding distributions in the numerical analysis depends on the critical value $\tilde{U}_{cr}$. The mean value together with upper and lower bounds of the roughness are determined for the three distributions (fig. 8.3).

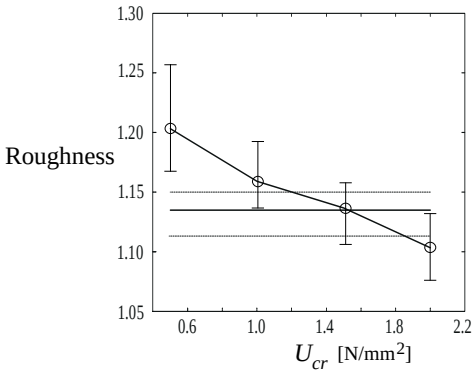

Figure 8.3: Mean value of roughness for the real and modelled crack paths using various $\tilde{U}_{cr}$.

The roughness of the modelled distributions varies depending on $\tilde{U}_{cr}$ and it is assumed that this critical value may be estimated by comparing the results from the real and modelled microstructures. The results coincide for $\tilde{U}_{cr} = 1.5\,\mathrm{N/mm^2}$ leading to an indication of the critical value. Thus, the procedure may be utilized to determine the strength of interfaces if the critical value can be related to the strength.

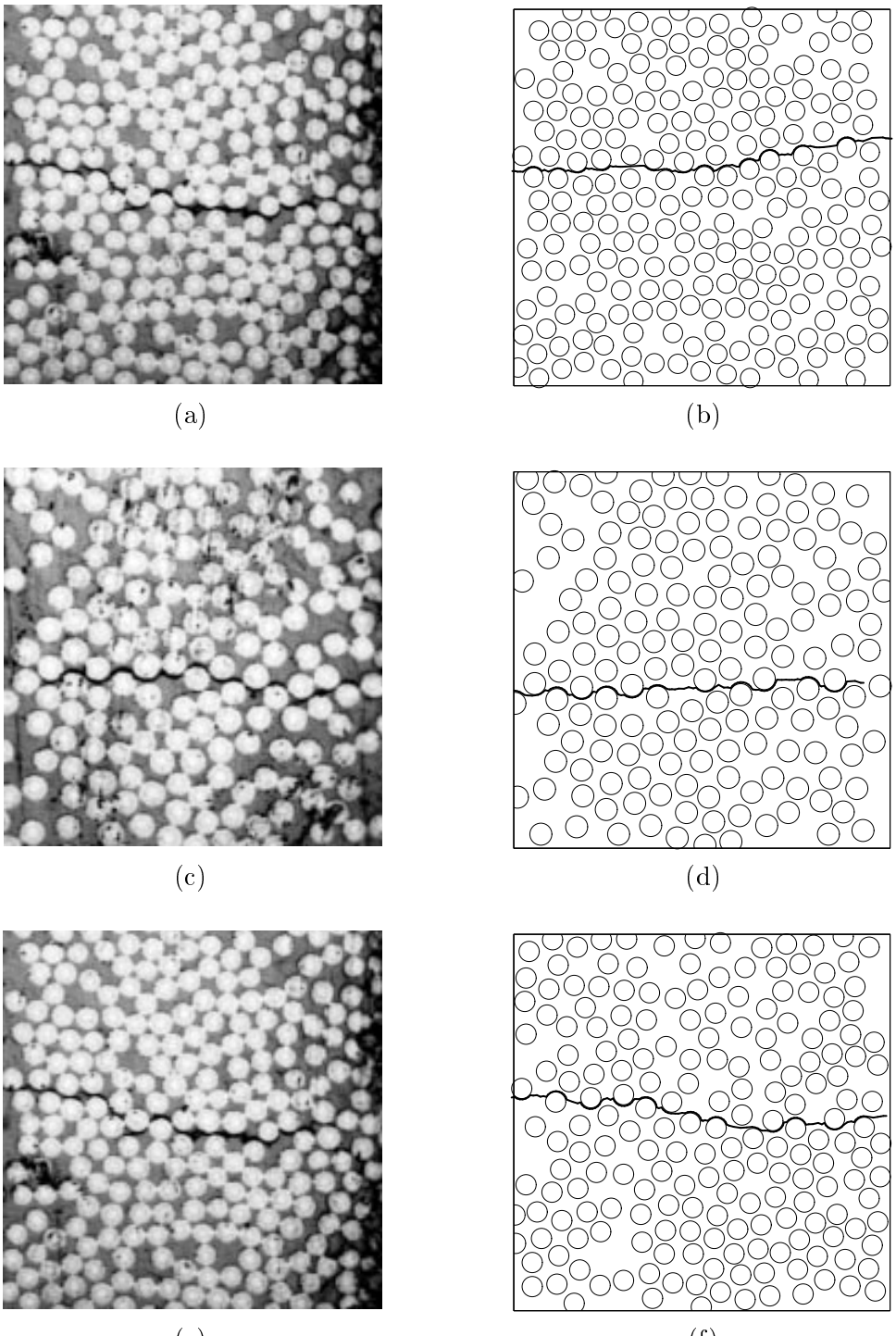

Figure 8.4: Real microstructures with real and modelled crack paths with $\tilde{U}_{cr} = 1.5\ N/mm^2$.

Conclusions

The aim of the present work is to investigate the correlation between the microstructure variability and the mechanical properties of a material. In the present work the microstructure variability has been envisioned as different types of fiber distributions. The mechanical properties are stress field in the fibers, local stress field in the matrix, stress intensity factors and crack growth. To obtain information of the mechanical properties it was necessary to develop a stress analysis method as well as a method for the determination of stress intensity factors. Also, in order to separate the various distribution of fibers in a non–visual manner it was necessary to apply a statistical description. In the following some of the most important conclusions of this work are summarized.

Analysis Method

The stress analysis method for determining the stress field in a solid containing multiple randomly dispersed inclusions has been derived in chapter 1. The method is solved using an iterative procedure where the interaction between the inclusions is superpositioned. The stress field determination is formulated analytically but solved through numerical integration. The main assumption and the disadvantage of the method are that the stress field within the fibers is uniform. Of course this introduces some inaccuracy in the results but comparing the usefulness of the present method with e.g. the finite element method makes it preferable to utilize in the present context. The geometrical modelling in the presented stress analysis method only consists of applying the centre coordinates of the fibers along with the radius. Thus, when increasing the number of fibers the pre–processing does not become more troublesome contrary to the finite element method. The analysis part consisting of the iterative procedure is relatively fast with respect to the computational time but the time is of course increased when the number of fibers is increased. The output from the iterative procedure is given by uniform stress fields within the fibers and the local stress field in the matrix may then be determined.

A method to determine the stress intensity factors for cracks situated among randomly dispersed inclusions is established in chapter 2. Both mode I and II crack opening are considered as the stress field introduces both normal and shear loading on the crack faces. The crack length and orientation may be arbitrary and the distribution of cracks may be random although they are not allowed to intersect. Furthermore, the relative inter–position between the cracks and also between fibers and cracks cannot be too small as this introduces an error in the calculation of the stress intensity factors. The method takes into account all interaction effects between fibers and cracks and these are included in transmission factors. Thus, by determining the stress interactions the stress intensity factors can be solved directly.

Proper crack growth criteria in a composite material containing randomly dispersed inclusions have been presented in chapter 3. Two damage modes are investigated in the method; pure matrix cracking and interface cracking. The crack growth criterion applied for the pure matrix cracks includes the stress intensity factors for both mode I and II crack opening, so that the crack may extend in a non–self–similar manner. The crack growth criterion applied for interface cracks does not include the determination of the stress intensity factors as the cracks are too close to the inclusions and consequently the stress intensity factors contain a considerable error. Instead, the criterion is based on the strain–energy–density. Thus, if the strain–energy–density at the crack tip of an interface crack is larger than a critical value related to the strength of the interface the crack starts to grow. The crack path is seen to be very much affected by the magnitude of the critical value. To account for both pure matrix cracking and interface cracking for multiple crack growth an iterative procedure has been proposed. To determine whether a matrix, or an interface crack starts to grow a self–imposed criterion must be applied.

Methods to establish a unit cell and to quantify the morphology of a microstructure are presented in chapter 4. The size of the unit cell is determined by distances at which the the stress interaction between fibers can be neglected. The unit cell consists of a sample area in which the actual fiber distribution is generated and a boundary area in which fibers are generated in order to apply boundary conditions to the actual fiber distribution. The degree of clustering of a microstructure may be determined by considering the information of nearest neighbour distances. Data for the nearest neighbour distances are curve–fitted with a continuous function and statistical moments are determined using both the discrete data and the continuous function. For approximately 200 fibers the discrete data is in agreement with the continuous function. The microstructure can also be quantified by applying the *second–order intensity function* and its derivative; the *pair distribution function*. Both functions are able to distinguish between various types of fiber distributions but they are only applicable for a limited range of the microstructure. Thus, the functions indicate the range of geometrical disorder and for a sample window larger than 0.25, having the total area of the sample equal to a unity, both functions coincide for various types of distributions.

Results of the Investigations

The stress field in a composite material with randomly dispersed fibers is correlated with the actual distribution of fibers in chapter 5. Distinct types of fiber distributions are generated and exposed to various boundary conditions. Both the mean value and variance of the nearest neighbour distance and orientation are determined for different distributions. The nearest neighbour distance indicates the degree of clustering whereas the nearest neighbour orientation is crucial for the interacting stress field. By comparing the mean value of the von Mises stress inside the fibers with the ratio between the mean nearest neighbour distance and orientation a correlation is detected. An indication of how the distribution of fibers affects the crack initiation is performed by determining the local stress field around the fibers. Peak values of stresses are calculated and the clustered distributions are the most sensitive towards the nucleation of cracks.

How the fracture toughness is affected by the configuration of fibers and a crack is presented in chapter 6. Some configurations increase the stress intensity factor and other decrease it. Thus, by rearranging the fibers the fracture toughness may be changed. The short–range interaction is estimated by determining how far away fibers must be

so that the interacting stress can be neglected. Long–range interaction is estimated by considering when the exact position of fibers becomes non–influential on the stress intensity factor. A function, which relates the stress intensity factor with the dispersion of fibers, is established. The function is called *direct correlation function* and is able to distinguish various distributions' influence on the fracture toughness, not only for various types of distributions but also within the particular type of distribution.

Degradation of the material through nucleation of microcracks is investigated in chapter 7. Configurations consisting of a macrocrack located in the vicinity of a fiber distribution are considered. Load is applied to the configuration and gradually increased until microcracks appear at all interfaces. During the load increase the stress intensity factor of the macrocrack is calculated. Both the interactions from the macrocrack and the initiated microcracks are included in the stress field calculation. Two crack types are considered; interface and matrix cracks. For interface cracks the configurations investigated show that the fracture toughness is changed. Thus, in a configuration where the presence of the fibers results in a decrease of the fracture toughness the nucleation of the interface cracks is seen to reverse the effect and increase the fracture toughness. For matrix cracks initiating at the interface, the fracture toughness seems to be unaffected by the nucleation of microcracks.

The crack growth in various types of fiber distributions is presented in chapter 8. Cracks are initiated at the edge of a microstructure at different positions and the cracks are then allowed to extend through the microstructure. The crack path is described by the roughness parameter and for clustered distributions the roughness is higher than for the non–clustered distributions. The crack path in real materials is measured and compared with the corresponding numerical model. The paths are not exactly similar as the damage evolution in a real material is affected by many other parameters than the numerical method is able to account for. Therefore, the roughness parameter of modelled and real microstructures is selected for comparison. By changing the strength of the interface in the numerical model the crack path changes and consequently the roughness is altered. Comparing the roughness for various strengths of the interface with the roughness from the real material, an estimate of the strength of the real material is given.

General Remarks

The present work contributes to the knowledge and understanding of how the morphology of multi–phase materials affects the mechanical behaviour. The work does not represent a complete description of the problem, but it provide information of the tendency. A complete description also seems unattainable as the mechanical behaviour in real materials is influenced by many other parameters.

In particular, the correlation between the stress intensity factors of cracks situated among each other and between fibers is a very complex problem. The pressure distribution on the crack faces is highly localized and therefore it is difficult to relate the descriptors of the microstructure distribution to crack parameters. For stress field analysis in a microstructure consisting of fibers and no cracks the problem is less localized. Therefore, the correlation between the type of distribution and stress field is more easily obtained.

Further Work

A further extension of the work presented in this report is reasonable as other mechanical properties are affected by the distribution of fibers. Thus, it would be interesting to consider the non–linear behaviour of the material which is much more sensitive to the details of the microstructure than the pure linear behaviour.

Many other configurations of fibers and cracks may also be considered as the ones presented here do not cover all possibilities.

References

[1] Axelsen, M.S. and Pyrz, R. (1995). "Correlation between Fracture Toughness and the Microstructure Morphology in Transversly Loaded Unidirectional Composites". To appear in the Proceedings of the IUTAM Symposium on Microstructure–Property Interactions in Composite Materials, R.Pyrz (ed.), Kluwer, Amsterdam 1995.

[2] Brockenbrugh, J.R., Suresh, S. and Wienecke, H.A. (1991). "Deformation of Metal–Matrix Composites with Continous Fibers: Geometrical Effects of Fiber Distribution and Shape". *Acta Metall. Mater.*, Vol. 39, No. 5, pp. 735–752.

[3] Daniel, I.M., Anastassopoulos, G. and Lee, J-W. (1989). "Failure Mechanisms in Ceramic Matrix Composites". *Proceedings of the SEM Spring Conference on Experimental Mechanics*, Cambrige, MA, pp. 832-838.

[4] Erdogan, F., Gupta, G.D. and Ratwani, M. (1974). "Interaction between a Circular Inclusion and an Arbitrarily Oriented Crack". *Journal of Applied Mechanics*, Vol. 41, pp. 1007-1013.

[5] Everett, R.K. and Chu, J.H. (1993). "Modeling of Non–Uniform Composite Microstructures". *Journal of Composite Materials*, Vol. 27, No. 11, pp. 1128-1144.

[6] Hori, M. and Nemat-Nasser, S. (1987). "Interacting Micro–Cracks Near the Tip in the Process Zone of a Macro–Crack". *Journal of Mechanics Physics and Solids*, Vol. 35, No. 5, pp. 601–629.

[7] Horii, H. and Nemat-Nasser, S. (1985). "Elastic Fields of Interacting Inhomogeneities". *International Journal of Solid and Structures*, Vol. 21, No. 7, pp. 731-745.

[8] Hu, K.X., Chandra, A. and Huang, Y. (1993). "Multiple Void–Crack Interaction". *International Journal of Solids and Structures*, Vol. 30, No. 11, pp. 1473-1489.

[9] Kachanov, M. (1987). "Elastic Solids with many Cracks-Simple Method of Analysis". *International Journal of Solids and Structures*, Vol. 23, pp. 23-43

[10] Kachanov, M., Montagut, E.L.E. and Laures, J.P. (1990). "Mechanics of Crack–Microcrack Interaction". *Mechanics of Materials*, Vol. 10, pp. 59–71.

[11] Lam, K.Y. and Phua, S.P. (1991). "Multiple Crack Interaction and its Effect on Stress Intensity Factors". *Engineering Fracture Mechanics*, Vol. 40, No. 3, pp. 585-592.

[12] Lam, K.Y. and Wen, C. (1993). "Interaction between Microcracks and a Main Crack in a Semi–Infinite Medium". *Engineering Fracture Mechanics*, Vol. 44, No. 5, pp. 753-761.

[13] Lam, K.Y. and Wen, C. (1993). "Enhancement/Shielding Effects of Inclusion on Arbitrarily Located Cracks". *Engineering Fracture Mechanics*, Vol. 46, No. 3, pp. 443-454.

[14] Meguid, S.A., Gaultier, P.E. and Gong, S.X. (1991). "A Comparison between Analytical and Finite Element Analysis of Main Crack–Microcrack Interaction". *Engineering Fracture Mechanics*, Vol. 38, No. 6, pp. 451-465.

[15] Mura, T. (1987). *Micromechanics of Defects in Solids.* 2nd Ed., Martinus Nijhoff Publishers, the Hauge, the Netherlands.

[16] Muskhelishvili, N.I. (1962). *Some Basic Problems of the Mathematical Theory of Elasticity.* Noordhoff International Publishing, Leyden.

[17] Pijaudier-Cabot, G. and Bažant, Z. P. (1991). "Cracks Interacting with Particles or Fibers in Composite Materials". *Journal of Engineering Mechanics*, Vol. 117, No. 7, pp. 1611-1630.

[18] Pyrz, R. (1993). "Stereological Quantification of The Microstructure Morphology for Composite Materials", Proc. IUTAM Symp. *Optimal Design with Advanced Materials*, P.Pedersen, ed., Elsevier, pp. 81-95.

[19] Pyrz, R. (1994). "Quantitative Description of Composites Microstructure. Part I: Morphology of Unidirectional Composite Systems". *Composite Science and Technology*, Vol. 50, pp. 197-208.

[20] Pyrz, R. (1993). "Correlation between Microstructure Variability and Local Stress Field in Two-phase Materials". *Materials Science and Engineering*, A177, pp. 253-259.

[21] Pyrz, R. (1993). "Interpretation of Disorder and Fractal Dimention in Transversly Loaded Unidirectional Composites". *Polym. and Polym. Comp.*, Vol. 1, pp. 283-295.

[22] Pyrz, R. and Bochenek, B. (1994). "Statistical Model of Fracture in Materials with Disordered Microstructure". *Science and Engineering of Composite Materials*, Vol. 3, No. 2, pp. 95-109.

[23] Pyrz, R. and Bochenek, B. (1994). "Discrete Model of Fracture in Disordered Two-phase Materials". To appear in the Proceedings of the IUTAM Symposium on Microstructure–Property Interactions in Composite Materials, R.Pyrz (ed.), Kluwer, Amsterdam 1995.

[24] Ripley, B.D. (1977). "Modelling Spatial Patterns". *Journal of Royal Statistical Society*, Series B, Vol. 39, No. 2, pp. 172-212.

[25] Sih, G.C. (1974). "Strain–Energy–Density Factor Applied to Mixed Mode Crack Problems". *International Journal of Fracture*, Vol. 10, No. 3, pp. 305-321.

[26] Tada, H. Paris, P.C. and Irwin, G.R. (1973). *The Stress Analysis of Cracks Handbook.* Del Research Corp., Hellertown, Pennsylvania.

[27] Yu, I.-W. and Sendeckyj, G.P. (1974). "Multiple Circular Inclusion Problems in Plane Elastostatics". *Journal of Applied Mechanics*, Vol. 41, pp. 215-221.

[28] Zhu, H. and Achenbach, J.D. (1991). "Radial Matrix Cracking and Interface Failure in Transversely Loaded Fiber Composites". *Mechanics of Materials*, Vol. 11, pp. 347-356.

APPENDIX

Appendix

A

Analytical Solution for One Inclusion

The single inclusion problem may be solved both with analytical and numerical methods. Two of the analytical methods are the Eshelby method (Mura [15]) and a method based on complex potential theory (Muskhelishvili [16]). In the Eshelby method it is assumed that the material properties of both the inclusion and the matrix are equal but the inclusion contains eigenstrains. This creates tractions at the boundary of the inclusion resulting in a disturbance of the stress field in the matrix. The eigenstrains are related to the Eshelby tensor and this can be solved for various shapes of the inclusion. The method based on complex potential theory is also derived by assuming an internal pressure inside the inclusion and it is derived in this appendix. The Eshelby method may be applied for three dimensional problems whereas the other method only applies for two dimensional problems.

The problem consists of determining the stress field in an infinitely extented plane solid containing a circular inclusion and subjected to unidirectional uniform tractions at the remote boundaries (fig. A.1). Radius of the inclusion is R and the coordinate system used has its origin in the center of the inclusion. Young's moduli are E_a and E_m for the inclusion and the matrix, respectively, and the corresponding Poisson's ratios are ν_a and ν_m.

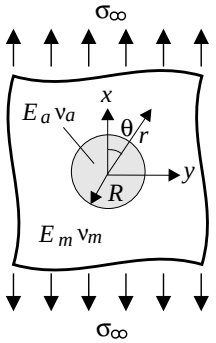

Figure A.1: Infinitely extented plane solid containing one inclusion.

The elastic equilibrium in the matrix is written as two analytical functions of the complex variable $z = re^{i\theta}$:

$$\begin{aligned} \phi_m(z) &= \frac{\sigma_\infty}{4}\left(z + \frac{\beta_m R^2}{z}\right) \\ \psi_m(z) &= -\frac{\sigma_\infty}{2}\left(z + \frac{\gamma_m R^2}{z} + \frac{\delta_m R^4}{z^3}\right) \end{aligned} \tag{A.1}$$

and the elastic equilibrium inside the inclusion is:

$$\begin{aligned} \phi_a(z) &= \frac{\sigma_\infty}{4}\left(\beta_a z + \frac{\gamma_a z^3}{R^2}\right) \\ \psi_a(z) &= -\frac{\sigma_\infty}{2}\delta_a z \end{aligned} \tag{A.2}$$

where β_m, γ_m, δ_m, β_a, γ_a, and δ_a are real constants to be determined. In complex potential theory the stress field may be written as a function of two analytical functions:

$$\begin{aligned} \sigma_x + \sigma_y &= 2(\phi'(z) - \overline{\phi'(z)}) \\ \sigma_x - i\sigma_{xy} &= \phi'(z) + \overline{\phi'(z)} - (\overline{z}\phi''(z) + \psi'(z)) \end{aligned} \tag{A.3}$$

The stress field in the matrix and in the inclusion may be solved by inserting equations A.1 and A.2 into equation A.3, respectively. The real constants are determined by applying the boundary conditions between the inclusion and the matrix. In cartesian coordinates the stress field in the matrix is:

$$\begin{aligned} \sigma_x &= \frac{\sigma_\infty}{2}\left[2 - \left(\frac{\beta_m R^2}{r^2} + \frac{\gamma_m R^2}{r^2}\right)\cos 2\theta - \left(\frac{\beta_m R^2}{r^2} + \frac{3\delta_m R^4}{r^4}\right)\cos 4\theta\right] \\ \sigma_y &= \frac{\sigma_\infty}{2}\left[\left(-\frac{\beta_m R^2}{r^2} + \frac{\gamma_m R^2}{r^2}\right)\cos 2\theta + \left(\frac{\beta_m R^2}{r^2} + \frac{3\delta_m R^4}{r^4}\right)\cos 4\theta\right] \\ \sigma_{xy} &= \frac{-\sigma_\infty}{2}\left[\frac{\gamma_m R^2}{r^2} + \left(\frac{2\beta_m R^2}{r^2} + \frac{6\delta_m R^4}{r^4}\right)\cos 2\theta\right]\sin 2\theta \end{aligned} \tag{A.4}$$

where the real constants become:

$$\beta_m = \frac{-2(\mu_a - \mu_m)}{\mu_m + \mu_a\kappa_m} \qquad \gamma_m = \frac{\mu_m(\kappa_a - 1) - \mu_a(\kappa_m - 1)}{2\mu_a + \mu_m(\kappa_a - 1)} \qquad \delta_m = \frac{\mu_a - \mu_m}{\mu_m + \mu_a\kappa_m} \tag{A.5}$$

The stress field in the inclusion is:

$$\sigma_x = \sigma_\infty\frac{\beta_a + \delta_a}{2} \qquad \sigma_y = \sigma_\infty\frac{\beta_a - \delta_a}{2} \qquad \sigma_{xy} = 0 \tag{A.6}$$

where

$$\beta_a = \frac{\mu_a(\kappa_m + 1)}{2\mu_a + \mu_m(\kappa_a - 1)} \qquad \gamma_a = 0 \qquad \delta_a = \frac{\mu_a(\kappa_m + 1)}{\mu_m + \mu_a\kappa_m} \tag{A.7}$$

The elastic constants, which enter in the equations, are defined as:

$$\mu_m = \frac{E_m}{2(1+\nu_m)} \qquad \mu_a = \frac{E_a}{2(1+\nu_a)} \tag{A.8}$$

$$\kappa_m = \frac{3-\nu_m}{1+\nu_m} \qquad \kappa_a = \frac{3-\nu_a}{1+\nu_a} \tag{A.9}$$

The stress field in the inclusion and the matrix may now be calculated given the material properties, geometry and the applied load.

Appendix

B

Standard Stress Field for Line Loads

In the superposition scheme for determining the stress intensity factors a pressure distribution is applied at the imaginary crack faces. This corresponds to line loads applied in an infinite solid. Such a problem may be solved in various ways and one of these methods, which was applied by Kachanov [9], is to introduce *standard stress fields*.

The problem consists of an infinite plane solid where a uniform load has been applied along a straight line. In the local coordinate system of this line the uniform load is divided into load components in the x and y direction. The load component in the x direction corresponds to tangential loading of the crack leading to mode II crack opening. The load component in the y direction corresponds to normal loading of the crack leading to mode I crack opening. The standard stress field makes it possible to determine the stress field anywhere in the solid due to both mode I and II loading of the crack knowing the magnitudes of the applied load components.

The stress field generated by a uniform load of unit intensity for mode I loading (standard stress field $\boldsymbol{\sigma}^n$):

$$\begin{aligned} \sigma_x^n &= I_2 - 8y^2 I_4 + 8y^4 I_6 \\ \sigma_y^n &= I_2 + 6y^2 I_4 - 8y^4 I_6 \\ \sigma_{xy}^n &= 2(-yI_3 + xyI_4 + 4y^3 I_5 - 4xy^3 I_6) \end{aligned}$$

The stress field generated by a uniform load of unit intensity for mode II loading (standard stress fields $\boldsymbol{\sigma}^t$):

$$\begin{aligned} \sigma_x^t &= 2(3yI_3 - 3xyI_4 - 4y^3 I_5 + 4xy^3 I_6) \\ \sigma_y^t &= 2(-yI_3 + xyI_4 + 4y^3 I_5 - 4xy^3 I_6) \\ \sigma_{xy}^t &= I_2 - 8y^2 I_4 + 8y^4 I_6 \end{aligned}$$

The notations in the above equations are:

$$\begin{aligned} I_2 &= 4l^2 \frac{1}{\sqrt{\delta}(\sqrt{\alpha} + \sqrt{\delta} + \sqrt{\gamma})} \\ I_3 &= 2l^3 \frac{\sqrt{\gamma} - \sqrt{\alpha}}{\delta^{3/2}\sqrt{\alpha\gamma}} \end{aligned}$$

$$
\begin{aligned}
I_4 &= 2l^2 \frac{\sqrt{\alpha}+\sqrt{\gamma}}{\delta^{3/2}\sqrt{\alpha\gamma}} \\
I_5 &= \frac{l^3}{2} \frac{3\sqrt{\alpha\gamma}(\sqrt{\alpha}+\sqrt{\gamma})^2\left(\sqrt{\gamma}-\sqrt{\alpha}\right)+\delta(\gamma^{3/2}-\alpha^{3/2})}{\delta^{5/2}(\alpha\gamma)^{3/2}} \\
I_6 &= \frac{l^2}{2} \frac{(\alpha^{3/2}+\gamma^{3/2})\delta+3\sqrt{\alpha\gamma}(\sqrt{\alpha}+\sqrt{\gamma})^3}{\delta^{5/2}(\alpha\gamma)^{3/2}}
\end{aligned}
$$

where

$$
\begin{aligned}
\alpha &= (x-l)^2+y^2 \\
\beta &= 2(x^2+y^2-l^2) \\
\gamma &= (x+l)^2+y^2 \\
\delta &= \beta+2\sqrt{\alpha\gamma}
\end{aligned}
$$

x and y are the distances from the center of the straight line to the point, at which the stress field is calculated. l corresponds to a half crack length that is $l=c$.

Appendix

C

Estimation of Local Range Parameters

The methods presented in the previous chapters are all implemented in numerical procedures and may therefore be solved variously depending on the input data such as accuracy of the numerical integrals, number of interaction terms, how many inclusions and cracks interact with a particular inclusion etc. All these inputs must be taken into consideration before making any analysis of different distributions. The necessity of these consideration is caused by the desire for having time-saving numerical procedures and at the same time enough statistical data. It is obvious that if the accuracy of the integrals is very precise and all interaction effects are taken into account the calculation time for the patterns is very long.

Local Interaction Parameters

One way to reduce the calculation time is to introduce a local effect parameter. This parameter gives the range of local interaction in such way that if the parameter is very large, all fibers and cracks interact with each other. Setting the parameter to a smaller value only neighbouring fibers and cracks interact. The parameter sets the radial distance from one fiber or crack and all other fibers and cracks within this distance are included in the interaction scheme. The problem is only to decide the magnitude of the local parameter.

In section 4.1 the zone of influence for various fiber arrangements is calculated. Here the stress inside the fibers is calculated and the variation of the strees field may be neglected for inter–fiber distances larger than 200 points. This leads to the conclusion that when determining the stress field in a solid containing multiple fibers (section 1.2) the local interaction parameter must be at least 200 points.

Another way of estimating the magnitude of the parameter is to calculate the stress intensity factor for a crack situated among different fiber arrangements (fig. C.1). The crack is approximately situated in the middle of the patterns and the length of the crack is $2c$ where the ratio between radius of fibers and the crack length is $R/c = 2$. The stress intensity factor is calculated for various magnitudes of the local effect parameter (fig. C.2). It is seen that the stress intensity factors for the regular distribution stabilize

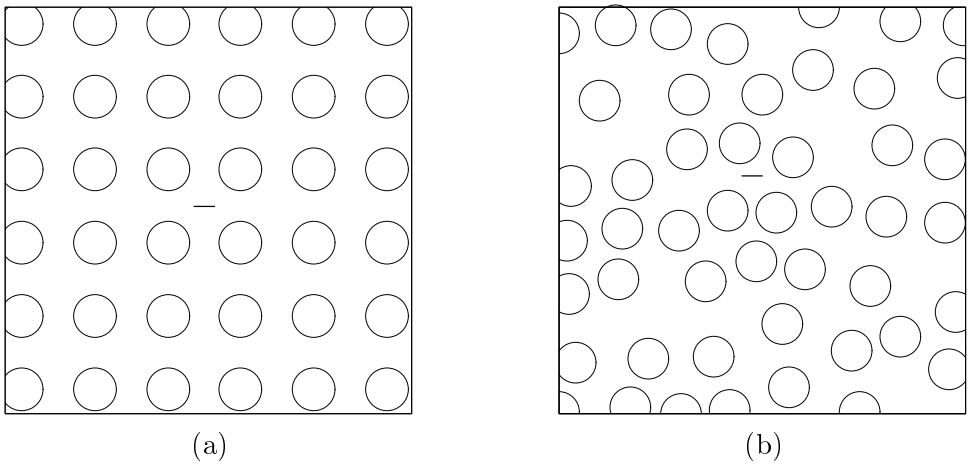

Figure C.1: One crack situated among two different fiber arrangements; (a) regular, (b) hardcore

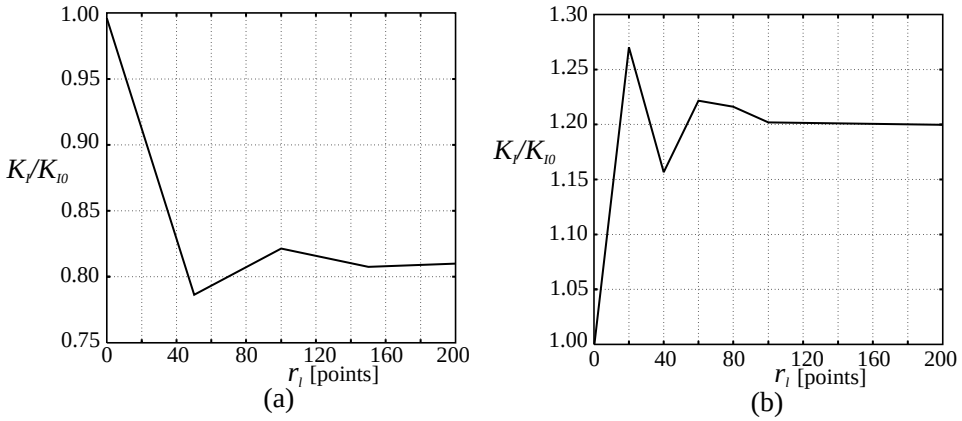

Figure C.2: Normalized stress intensity factors for; (a) regular arrangement, (b) hardcore arrangement.

for $r > 150$ points whereas they stabilize for the hardcore distribution for $r > 80$ points. Therefore, the local interaction parameter must be at least 150 points when calculating the stress intensity factors.

Printed at Aalborg University, January 1995.

ISBN 87-89206-03-7